Thallium Tellurides as Thermoelectrics

by

Quansheng Guo

A thesis

presented to the University of Waterloo

in fulfillment of the

thesis requirement for the degree of

Doctor of Philosophy

in

Chemistry

Waterloo, Ontario, Canada 2015

Author's Declaration

I hereby declare that I am the sole author of this thesis. This is a true copy of the thesis, including any required final revisions, as accepted by my examiners. I understand that my thesis may be made electronically available to the public.

Abstract

Noting the steadily worsening problem of depleted fossil fuel sources, alternate energy sources become increasingly important, such as thermoelectrics that may use waste heat to generate electricity. To be economically viable, the thermoelectric figure-of-merit, zT, – related to the energy conversion efficiency – needs to be in excess of unity ($zT > 1$). Modifications of Tl_5Te_3 show great promise as thermoelectrics due to their intrinsically low thermal conductivity.

Herein thallium lanthanide tellurides Tl_9LnTe_6 (Ln = La, Ce, Pr, Nd, Sm, Gd, Tb) have been prepared and their high temperature electrical and thermal transport properties investigated. Single phase samples were obtained. The electrical conductivity and thermal conductivity increased across the lanthanide series from La to Tb. On the other hand, the Seebeck coefficient values decreased with Ln varying from La to Tb. Tl_9SmTe_6 or Tl_9GdTe_6 constituted an exception, as the Seebeck coefficient of Tl_9SmTe_6 was smaller than that of Tl_9GdTe_6. Tl_9LaTe_6 had the largest figure-of-merit $zT = 0.51$ at 550 K. Thereafter, $Tl_{10-x}La_xTe_6$ samples were prepared with x = 0.90, 0.95, 1.00, 1.05, 1.10, aiming toward higher zT through composition optimization and expanding of the measurement temperature range. With the increasing La content, the unit cell volume increased, while the electrical conductivity, thermal conductivity and lattice thermal conductivity decreased. An opposite trend between Seebeck coefficient and electrical conductivity was observed. The highest $zT = 0.57$ was realized for Tl_9LaTe_6 at 600 K.

The isostructural series $Tl_9Sb_{1-x}Te_6$, $Tl_{9-x}Sb_{1+x}Te_6$, $Tl_9Bi_{1-x}Te_6$ and $Tl_{9-x}Bi_{1+x}Te_6$, with x ranging from 0 to 0.05, were prepared from the elements in the stoichiometric ratios, and the thermoelectric properties determined. In theory, these tellurides are narrow gap semiconductors when $x = 0$, with all elements in common oxidation states, according to $(Tl^+)_9(Sb^{3+}/Bi^{3+})(Te^{2-})_6$. The as-prepared samples of this 9-1-6 stoichiometry however exhibited relatively high electrical conductivity, which decreased with

increasing temperature, indicative of the presence of extrinsic charge carriers. The Seebeck coefficient was generally above +100 μV K^{-1}. Decreasing the Sb or Bi content then increased the hole concentration, and thus increased the electrical conductivity while decreasing the Seebeck coefficient. The best feature of these thermoelectrics was their low thermal conductivity, being consistently well below 0.7 W $m^{-1}K^{-1}$. Combined with reasonable electrical conductivity and high Seebeck coefficient, high zT values in excess of 1 can be achieved via simple hot-pressing as well, after experimental optimization of the carrier concentration via introducing deficiencies on the Bi site. Moreover, the variants with Sb instead of Bi exhibited similar thermoelectric performance, a result of the combination of a better electrical performance and higher thermal conductivity.

To investigate the effects of Sn- and Pb-doping, several samples with the nominal composition $Tl_9Bi_{1-x}Sn_xTe_6$, $Tl_9Bi_{1-y}Pb_yTe_6$ ($0 \leq x, y \leq 0.15$), $Tl_9Sb_{1-m}Sn_mTe_6$ and $Tl_9Sb_{1-n}Pb_nTe_6$ ($0 \leq m, n \leq 0.10$) were investigated. Thermoelectric property measurements showed that increasing doping caused increases in electrical and thermal conductivity, while decreasing the Seebeck coefficient. Mixed results were obtained for the lattice thermal conductivity, which decreased in some cases, but increased in others. At around 500 K, competitive zT values were obtained for $Tl_9Bi_{0.95}Sn_{0.05}Te_6$, $Tl_9Bi_{0.95}Pb_{0.05}Te_6$, $Tl_9Sb_{0.97}Sn_{0.03}Te_6$, and $Tl_9Sb_{0.95}Pb_{0.05}Te_6$, namely 0.95, 0.94, 0.83 and 0.71, respectively. Higher dopant concentrations led to lower zT values.

The 8-2-6 variants Tl_4SnTe_3 and Tl_4PbTe_3 were reported to attain a thermoelectric figure-of-merit zT_{max} = 0.74 and 0.71 at 673 K, respectively. Here, the thermoelectric properties of both materials are presented in dependence of x in $Tl_{10-x}Sn_xTe_6$ and $Tl_{10-x}Pb_xTe_6$, with x varying between 1.9 and 2.05, culminating in zT_{max} values in excess of 1.2. These materials are charge balanced when x = 2, according to $(Tl^+)_8(Sn^{2+})_2(Te^{2-})_6$ and $(Tl^+)_8(Pb^{2+})_2(Te^{2-})_6$ (or: $(Tl^+)_4Pb^{2+}(Te^{2-})_3$). Increasing x caused an increase in valence electrons, and thus a decrease in the dominating p-type charge carriers. Thusly, larger x values

occurred with a smaller electrical conductivity and a larger Seebeck coefficient. In each case, the lattice thermal conductivity remained under 0.5 W $m^{-1}K^{-1}$, resulting in several samples attaining the desired $zT_{max} > 1$. The highest values thus far are exhibited by $Tl_{8.05}Sn_{1.95}Te_6$ with $zT = 1.26$ and $Tl_{8.10}Pb_{1.90}Te_6$ with $zT = 1.46$ around 685 K. These materials are very competitive compared to other leading bulk materials as well, including the *n*-type triple-filled skutterudite $Ba_{0.08}La_{0.05}Yb_{0.04}Co_4Sb_{12}$, the *p*-type Zintl phase $Yb_{13.6}La_{0.4}MnSb_{11}$ and *p*-type $Tl_{0.02}Pb_{0.98}Te$ until 673 K.

Acknowledgements

I want to express my sincere gratitude to my supervisor Professor Holger Kleinke for his advice, guidance and patience during my Ph. D studies and research activities. I feel very lucky to work with him for four years.

It is also enjoyable and impressive to work with so many helpful colleagues: research assistant Katja, crystallographer Dr. Jalil, postdoctor Dr. Raj and Dr. Bryan, Dr. Savi, Abdul, Susan, Nagaraj, Nader, Nhi, Mohamed, Rafay, Mathew, Yixuan, Parisa, Xiaoyu and Wenbin.

The last but not the least, I also want to thank my advisory committee members Professor Richard T. Oakley, Professor Pavle Radvanovic, Professor Kathryn Preuss and examiners Professor Andrew Grosvenor and Professor Michael Tam for their suggestions on my work.

Table of Contents

List of Figures

List of Tables

List of Symbols and Abbreviations

Symbols

η_{max}	maximum efficiency of a thermoelectric power generator
φ_{max}	maximum efficiency of a thermoelectric refrigerator
zT	the dimensionless figure-of-merit of the thermoelement
σ	electrical conductivity
α	Seebeck coefficient
κ	thermal conductivity
T	temperature
n	carrier concentration
μ	mobility; chemical potential
E_F	Fermi energy
k_B	Boltzmann constant
κ_E	electrical thermal conductivity
κ_L	lattice thermal conductivity
$g(E)$	density of states
m^*	density of states effective mass
N	number of degenerate valleys
m_d	density of states effective mass for individual valley
τ	relaxation time
e	elementary charge
$F_j(\eta)$	the j^{th} order Fermi integral
η	reduced chemical potential
λ	scattering parameter; thermal diffusivity
L	Lorenz number
C_V	heat capacity of the lattice per unit volume
υ	average phonon velocity
$\bar{m}/M_{avg}$	average atomic mass

θ_D	Debye temperature
γ	Grüneisen parameter,
V_C	the unit cell volume
N_{atom}	the number of atoms per cell
T_m	melting point
ρ_m	mass density
κ_{min}	the minimum lattice thermal conductivity
$\hbar$	reduced Planck constant
Δ	the average volume per atom

Abbreviations

PGEC	phonon-glass electron-crystal
XRD	X-ray diffraction
SEM	scanning electron microscopy
GSAS	General Structure Analysis System
EDX	energy dispersive X-ray analysis
DFT	density functional theory
LDA	local density approximation
GGA	generalized gradient approximation
APW	augmented plane wave
LMTO	linear muffin tin orbital method
FP	full-potential
LCAO	linear combination of atomic orbitals
TB	tight-binding method
ASA	atomic-spheres-approximation
DOS	density of states

1. Introduction

1.1. Application of Thermoelectrics

Thermoelectrics could be defined as the science and technology related to thermoelectric generation and refrigeration. Thermoelectric devices have many advantages, such as high reliability, no moving parts, efficiency independent of size, no maintenance, acoustically silent, and environmentally friendly.[1]

Thermoelectric effects mainly refer to the Seebeck effect, Peltier effect and Thomson effect. The Seebeck effect is used to directly convert thermal energy into electricity. Since the 1960s, thermoelectric power generator has supplied power to the spacecrafts, working in the temperature range of ~500 K to 1273 K. Another interesting applications of the Seebeck effect is in the automotive industry where approximately 70% the energy generated from the gasoline combustion is lost in the form of heat.[2]

Conversely, the Peltier effect is used as thermoelectric refrigerators involving the generation or absorption of the heat when an electrical current is flowing through the closed thermoelectric circuit. The Peltier effect is commercially utilised in wine storage cabinets, night-vision systems, beverage and picnic coolers, automobile seats and in electronic systems like laser diodes cooling.[3]

1.2. Thermoelectric Efficiency and Figure-of-Merit

The maximum efficiency of a thermoelectric power generator (η_{max}) or a thermoelectric refrigerator (φ_{max}) is expressed as

$$\eta_{max} = \frac{T_H - T_C}{T_H} \frac{\sqrt{1+ZT}-1}{\sqrt{1+ZT}+T_C/T_H} \tag{1-1}$$

$$\varphi_{\max} = \frac{T_C}{T_H - T_C} \frac{\sqrt{1+ZT} - T_H/T_C}{\sqrt{1+ZT}+1} \tag{1-2}$$

where T is the mean temperature of the hot-side (T_H) and the cold-side (T_C). The maximum coefficient of performance is directly related to the dimensionless figure-of-merit (zT) of the thermoelement

$$zT = \frac{\alpha^2 \sigma}{\kappa} T \tag{1-3}$$

Here σ [$\Omega^{-1}m^{-1}$] is the electrical conductivity, α [V K^{-1}] is the Seebeck coefficient, κ [W $m^{-1}K^{-1}$] is the total thermal conductivity and T [K] the absolute temperature. To achieve high zT, a high Seebeck coefficient and large electrical conductivity are required, enabling the generation of a high voltage and a high current. Meanwhile, the thermal conductivity should be comparatively low as a large temperature gradient must be maintained. Therefore thermoelectric materials ideally behave as 'phonon-glass electron-crystal'(PGEC) materials because crystalline semiconductors provide the best compromise between Seebeck coefficient and electrical conductivity, and glasses show some of the smallest lattice thermal conductivity values.[4] The maximum zT values are available in degenerate semiconductors with carrier concentrations between 10^{19} and 10^{21} cm^{-3}. A typical thermoelectric module consists of many (typically 18 – 128) pairs of p-type and n-type semiconducting thermoelements, which are connected electrically in series and thermally in parallel. In practical applications, thermoelectric materials with zT > 1 are thought to be especially efficient.[5]

1.2.1. Electrical Conductivity

The electrical conductivity of a solid is given by the well-known formula

$$\sigma = ne\mu \tag{1-4}$$

where n is the carrier concentration and μ the electron drift velocity per unit electric field, or the mobility.[6] The expressions for transport properties of single type carriers in a single energy band could be derived by solving the Boltzmann transport equation.[7] The formal expression for the Boltzmann transport equation is

$$\left(\frac{df}{dt}\right)_{sc} = \frac{df}{dt} + \frac{d\vec{k}}{dt}\nabla_{\vec{k}} f + \frac{d\vec{r}}{dt}\nabla_{\vec{r}} f \tag{1-5}$$

where t is the time, $\vec{k}$ and $\vec{r}$ are the wave and position vectors of electrons and f the non-equilibrium function. If the electrical field and temperature gradient lie along the x-axis, then $d\vec{k}/dt = -e\varepsilon/\hbar$, $\nabla_{\vec{r}} f = (\partial f/\partial T)(dT/dx)$ and $\nabla_{\vec{k}} f = (\partial f/\partial E)(dE/dk) = \hbar\upsilon(\partial f/\partial E)$. Under the *relaxation time* approximation

$$\left(\frac{df}{dt}\right)_{sc} = -\frac{f - f_0}{\tau} \tag{1-6}$$

The solution is stated in term of the unperturbed Fermi-Dirac distribution function f_0

$$f_0(E) = \frac{1}{1 + \exp[(E - \mu)/k_B T]} \tag{1-7}$$

Where E is the electron's energy, μ is the chemical potential and k_B the Boltzmann constant. It is assumed that $f - f_0 \ll f_0$ and then f could be replaced by f_0 on the right-hand side of Equation (1-5). It is also assumed that the surfaces of constant energy in phase space are spherical and the energy E is proportional to k^2, $E = (\hbar^2 k^2)/(2m^*)$. Now the first-order steady state solution to the Boltzmann transport equation could be expressed as

$$f(E) - f_0(E) = -\tau(E)\upsilon(E)\frac{df_0}{dE}\left(\mp e\varepsilon - \frac{E - \mu}{T}\frac{dT}{dx}\right) \tag{1-8}$$

Subsequently, the electric current density and heat current density are

$$J \equiv \mp ne\upsilon = \mp e\int_{-\infty}^{+\infty} g(E)\upsilon(E)[f(E) - f_0(E)]dE \tag{1-9}$$

$$Q \equiv n(E-\mu)\upsilon = \int_{-\infty}^{+\infty} g(E)(E-\mu)\upsilon(E)[f(E) - f_0(E)]dE \tag{1-10}$$

where n is the carrier concentration, $\upsilon(E) = \sqrt{(2E)/(3m^*)}$ is the averaged carrier velocity along one axis and $g(E) = 4\pi(2m^*)^{3/2}h^{-3}E^{1/2}$ is the density of states in a unit volume of free space in three dimensions. Here $m^* = N^{2/3}m_{\mathrm{d}}$ is the density of states effective mass for all valleys, N is the number of degenerate valleys and m_{d} the density of states effective mass for individual valley. The maximum value of N is limited by the crystalline symmetry. The largest N is 48 in cubic, followed by 24 in hexagonal, 16 in tetragonal, 8 in orthorhombic, and 4 or less in the other crystal systems.[8] From the charge density and heat current density and the standard definitions, we could get the expressions for the transport coefficients for conduction perpendicular to directions of confinement. Now let the temperature gradient be zero, $dT/dx = 0$ and the electric field is $\pm\varepsilon$. So the electrical conductivity is

$$\sigma \equiv \left.\frac{J}{\varepsilon}\right|_{dT/dx=0} = -e^2\int_{-\infty}^{+\infty} g(E)\tau(E)\upsilon^2(E)\frac{df_0(E)}{dE}dE \tag{1-11}$$

When the relaxation time τ could be expressed by a power law, $\tau = \tau_0 E^{\lambda}$ where λ is the characteristic constant for a particular scattering process and τ_0 is a constant determined by scattering process and material properties, the electrical conductivity and equilibrium carrier concentration could be expressed as

$$\sigma = \frac{8\pi(2)^{3/2}}{3h^3}e^2(m^*)^{1/2}\tau_0(k_{\mathrm{B}}T)^{\lambda+3/2}(\lambda+3/2)F_{\lambda+1/2}(\eta) \tag{1-12}$$

$$n = \int_{-\infty}^{+\infty} g(E)f_0(E)dE = \frac{N}{2\pi^2}\left(\frac{2k_{\mathrm{B}}Tm_{\mathrm{d}}}{\hbar^2}\right)^{3/2}F_{1/2}(\eta) = \frac{4\pi(2m^*k_{\mathrm{B}}T)^{3/2}}{h^3}F_{1/2}(\eta) \tag{1-13}$$

$F_j(\eta) = \int_0^{+\infty} \frac{x^j}{1+e^{x-\eta}} dx$ is the j^{th} order Fermi integral and $\eta = \mu / k_B T$ is the reduced chemical potential.

Then the mobility is

$$\mu = \frac{2e}{3m^*} \tau_0 (k_B T)^{\lambda} (\lambda + 3/2) \frac{F_{\lambda+1/2}(\eta)}{F_{1/2}(\eta)} \tag{1-14}$$

1.2.2. Seebeck Coefficient

In 1821, Thomas Johann Seebeck discovered that when two elements were connected electrically in series and thermally in parallel and if the junctions were maintained at different temperatures, an open circuit electromotive force would be detectable.

The produced voltage difference (ΔV) was directly proportional to the temperature difference between the hot side and the cold side ($\Delta T = T_H - T_C$)

$$\alpha = \left(\frac{dV}{dT}\right)_a - \left(\frac{dV}{dT}\right)_b = \frac{\Delta V}{\Delta T} = \frac{\Delta V}{T_H - T_C} (\Delta T \to 0) \tag{1-15}$$

which defines the differential Seebeck coefficient α between the elements a and b. All superconductors have zero Seebeck coefficients below their critical temperatures.

Alternatively, let the electric current be zero in Equation (1-10)

$$J \equiv \mp ne\upsilon = \mp e \int_{-\infty}^{+\infty} g(E)\upsilon(E) \left\{ -\tau(E)\upsilon(E) \frac{df_0}{dE} \left[\mp e\varepsilon - \frac{E-\mu}{T} \frac{dT}{dx} \right] \right\} dE = 0 \tag{1-16}$$

$$e\varepsilon \int_{-\infty}^{+\infty} g(E)\upsilon^2(E)\tau(E) \frac{df_0}{dE} dE \pm \frac{1}{T} \frac{dT}{dx} \int_{-\infty}^{+\infty} g(E)\upsilon^2(E)\tau(E) \frac{df_0}{dE} (E-\mu) dE = 0 \tag{1-17}$$

Then the Seebeck coefficient is

$$\alpha \equiv \left. \frac{\varepsilon}{\frac{dT}{dx}} \right|_{J=0} = \pm \frac{1}{eT} \left\{ \frac{\int_{-\infty}^{+\infty} g(E)\tau(E)\upsilon^2(E) E \left(df_0/dE\right) dE}{\int_{-\infty}^{+\infty} g(E)\tau(E)\upsilon^2(E) \left(df_0/dE\right) dE} - \mu \right\} \tag{1-18}$$

which is positive for holes and negative for quasi-free electrons. In combination with the expression for carrier velocity, the Seebeck coefficient could be expressed as

$$\alpha = \pm \frac{k_{\mathbf{B}}}{e} \left\{ \frac{(\lambda + 5/2) F_{\lambda+3/2}(\eta)}{(\lambda + 3/2) F_{\lambda+1/2}(\eta)} - \eta \right\} \tag{1-19}$$

By employing the Bethe-Sommerfeld expansion, we arrive at

$$K_1 \cong \frac{\pi^2}{3} (k_B T)^2 \left(\frac{\partial K_0}{\partial E} \right)_{E=\mu} \tag{1-20}$$

$$K_n = \int_{-\infty}^{+\infty} g(E) \upsilon^2(E) \tau(E) \frac{df_0}{dE} (E - \mu)^n dE \tag{1-21}$$

and the Mott formula[9]

$$\alpha = \pm \frac{1}{eT} \frac{K_1}{K_0} = \pm \frac{\pi^2}{3} \frac{k_B^2 T}{e} \left. \frac{\partial [ln\, \sigma(E)]}{\partial E} \right|_{E=\mu} \tag{1-22}$$

1.2.3. Thermal Conductivity

Thermal conductivity comes mainly from two sources: (1) heat energy transported by carriers (κ_E) and (2) heat conducted through phonons (κ_L), *i.e.* $\kappa = \kappa_E + \kappa_L$. The electronic term ($\kappa_E$) is derived as follows

$$\begin{aligned} Q \equiv n(E-\mu)v &= \int_{-\infty}^{+\infty} g(E)(E-\mu)\upsilon(E)[-\tau(E)\upsilon(E)\frac{df_0}{dE}\left[\mp e\varepsilon - \frac{E-\mu}{T}\frac{dT}{dx} \right]]dE \\ &= \pm e\varepsilon \int_{-\infty}^{+\infty} g(E)\upsilon^2(E)\tau(E)(E-\mu)\frac{df_0}{dE}dE + \frac{1}{T}\frac{dT}{dx}\int_0^{+\infty} g(E)\upsilon^2(E)\tau(E)(E-\mu)^2 dE \\ &= \mp \frac{\frac{1}{T}\frac{dT}{dx}\left\{ \int_{-\infty}^{+\infty} g(E)\upsilon^2(E)\tau(E)(E-\mu)\frac{df_0}{dE}dE \right\}^2}{\int_{-\infty}^{+\infty} g(E)\upsilon^2(E)\tau(E)\frac{df_0}{dE}dE} + \frac{1}{T}\frac{dT}{dx}\int_{-\infty}^{+\infty} g(E)\upsilon^2(E)\tau(E)(E-\mu)^2 dE \end{aligned} \tag{1-23}$$

$$\kappa_{\mathrm{E}} \equiv -\left.\frac{Q}{\dfrac{dT}{dx}}\right|_{J=0} = \frac{1}{T}\left\{-\int_{-\infty}^{+\infty} g(E)\tau(E)\upsilon^2(E)E^2\frac{df_0}{dE}dE + \frac{\left(\int_{-\infty}^{+\infty} g(E)\tau(E)\upsilon^2(E)E\dfrac{df_0}{dE}dE\right)^2}{\int_{-\infty}^{+\infty} g(E)\tau(E)\upsilon^2(E)\dfrac{df_0}{dE}dE}\right\} \tag{1-24}$$

According to the Wiedemann–Franz law[10]: $\kappa_{\mathrm{E}} = L\sigma T$, then Lorenz number L is expressed by

$$L = \frac{\kappa_{\mathrm{E}}}{\sigma T} = \left(\frac{k_{\mathbf{B}}}{e}\right)^2\left\{\frac{(\gamma+7/2)F_{\gamma+5/2}(\eta)}{(\gamma+3/2)F_{\gamma+1/2}(\eta)} - \left(\frac{(\gamma+5/2)F_{\gamma+3/2}(\eta)}{(\gamma+3/2)F_{\gamma+1/2}(\eta)}\right)^2\right\} \tag{1-25}$$

By analogy with the kinetic theory of gases, the lattice thermal conductivity is given by

$$\kappa_{\mathbf{L}} = \frac{1}{3}C_{\mathbf{V}}\upsilon l \tag{1-26}$$

where l is the mean free path of the phonons, C_{V} is the heat capacity of the lattice per unit volume and υ is the average phonon velocity.[11]

The lattice thermal conductivity is the only parameter entering the figure-of-merit that is not related to the electrical properties. Slack proposed a theory to evaluate the thermal conductivity from crystallographic data, assuming that the most contribution to the lattice thermal conductivity is from the acoustic phonons, which possess higher group velocity than optical phonons.[12]

$$\kappa_{\mathbf{L}} \propto \frac{\bar{m}\theta_{\mathrm{D}}{}^3\delta}{\gamma^2\left(N_{\mathrm{atom}}\right)^{2/3}T} \tag{1-27}$$

where $\bar{m}$ is the average atomic mass, θ_{D} is the Debye temperature, γ is the Grüneisen parameter, $\delta = \sqrt[3]{V_{\mathrm{C}}/N_{\mathrm{atom}}}$ is a measure of atomic distance with V_{C} being the unit cell volume and N_{atom} the number of atoms per cell. The Debye temperature could be estimated by Lindemann's formula[13]

$$\theta_{\mathrm{D}} \approx 120\frac{(T_{\mathrm{m}})^{1/2}(\rho_{\mathrm{m}})^{1/3}}{(\bar{m})^{5/6}} \propto \frac{(T_{\mathrm{m}})^{1/2}\delta}{(\bar{m})^{1/2}} \tag{1-28}$$

where T_{m} is the melting point and ρ_{m} the mass density. Equation (1-27) could be expressed as

$$\kappa_{\mathrm{L}} \propto \frac{(T_{\mathrm{m}})^{3/2}\delta^4}{(\bar{m})^{1/2}\gamma^2\left(N_{\mathrm{atom}}\right)^{2/3}} \tag{1-29}$$

Therefore low melting point, high average atomic masses, a large number of atoms per unit cell, and large atomic distances will enable a low lattice thermal conductivity.

To which extent the figure-of-merit could be optimized, could be estimated by comparing the actual lattice thermal conductivity with the minimum lattice thermal conductivity κ_{min}, which is achieved assuming that the mean free path of the phonons is half of the wavelength of the phonons. κ_{min} is calculated according to Cahill's formulation[14],

$$\kappa_{\mathrm{min}} = \left(\frac{\pi}{6}\right)^{1/3} k_{\mathrm{B}}\Delta^{-2}\sum_i \upsilon_{\mathrm{i}}\left(\frac{T}{\Theta_{\mathrm{i}}}\right)^2 \int_0^{\Theta_{\mathrm{i}}/T} \frac{x^3 e^x}{\left(e^x-1\right)^2}\,dx \tag{1-30}$$

where the summation is over the one longitudinal and two transverse modes, Δ represents the average volume per atom, $\Theta_{\mathrm{i}} = \upsilon_{\mathrm{i}}(\hbar/k_{\mathrm{B}})(6\pi^2\Delta^{-3})^{1/3}$, and υ_{i} is the sound velocity for the longitudinal and transverse modes.

1.3. State-of-the-art Thermoelectrics

1.3.1. Bismuth Telluride and IVA Tellurides

The commercialized thermoelectric refrigeration material, Bi_2Te_3, was first investigated as a thermoelectric candidate in 1954. It crystallizes in a layered structure (Figure 1.1) with space group $R\bar{3}m$.[15] The hexagonal unit cell dimensions at room temperature are a = 3.8 Å and c = 30.5 Å. The atomic layers stacked along the c-axis form the sequence ⋯ Te[1]–Bi–Te[2]–Bi–Te[1] ⋯. The tellurium and bismuth layers are connected together by strong ionic-covalent bonds, whereas the bonding between neighbouring Te layers is based on weak van der Waals-type forces.[16] Consequently, this weak binding

accounts for the ease of cleavage in planes perpendicular to the *c*-axis and the anisotropy of electrical and thermal transport properties as well. *n*-Type $Bi_2Te_{2.7}Se_{0.3}$ and *p*-type $Bi_{0.5}Sb_{1.5}Te_3$ are the optimum compositions for thermoelectric refrigeration devices.[17]

For power generation at higher temperatures (500 – 900 K), materials based on group IVA tellurides are typically utilized, such as GeTe, SnTe, and PbTe. They all crystallize in a cubic NaCl-type crystal structure which leads to high valley degeneracy for high electrical conductivity and phonon anharmonicity for low thermal conductivity.[18] A radioisotope thermoelectric generator (RTG) containing *p*-type and *n*-type PbTe were used by NASA for its first RTG spacecraft.[19] The *zT* values of doped PbTe will reach ~ 2.0 at 750 – 900 Kelvin, making PbTe a prime candidate for power generation.[20]

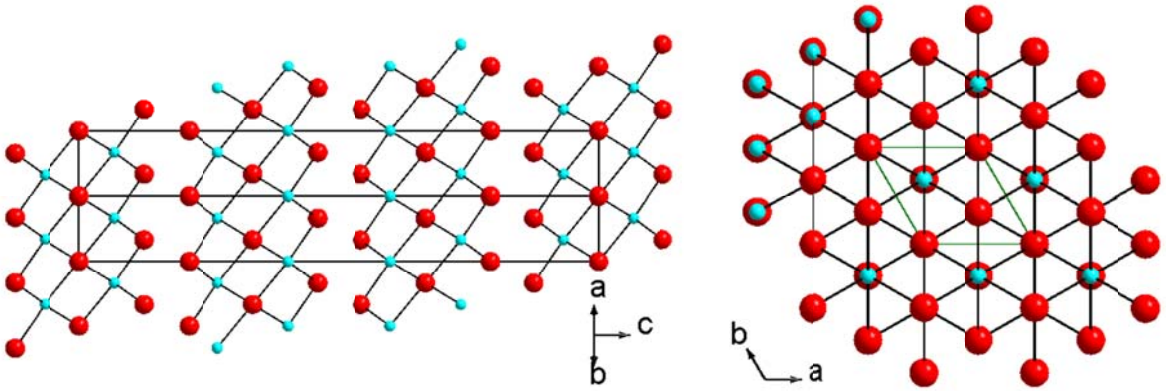

Figure 1.1 Crystal structure of Bi_2Te_3. Bi:cyan; Te: red.

1.3.2. Cage Compounds

The skutterudite MX_3 (M = transition metals Co, Rh, Ir, and X represents a pnicogen atom) was found in a small mining town Skutterud, in Norway. Skutterudites crystallize in space group $Im\bar{3}$ containing tilted corner-sharing MX_3 octahedra, making it a distorted variant of the ReO_3 structure (Figure 1.2). There are six planar X_4 rectangles lying parallel to either the (100), (010), (001)

crystallographic planes with X–X bonds existing as well as two large X_{12} icosahedra in one unit cell.[21] Filling the icosahedra with guest atoms, such as alkali metals, alkaline or rare earth metals will lead to the formation of the filled skutterudites of the general formula $Ln_xM_4X_{12}$, thereby modifying the electrical conductivity through adding additional electrons and reducing the lattice thermal conductivity, thusly enhancing the figure-of-merit. Alloying on the M or X site will also reduce the lattice thermal conductivity.[22, 23] Some doped skutterudites show exceptionally high zT values at elevated temperatures ($zT \sim 1.5$ at 600 – 800 K).[24-26]

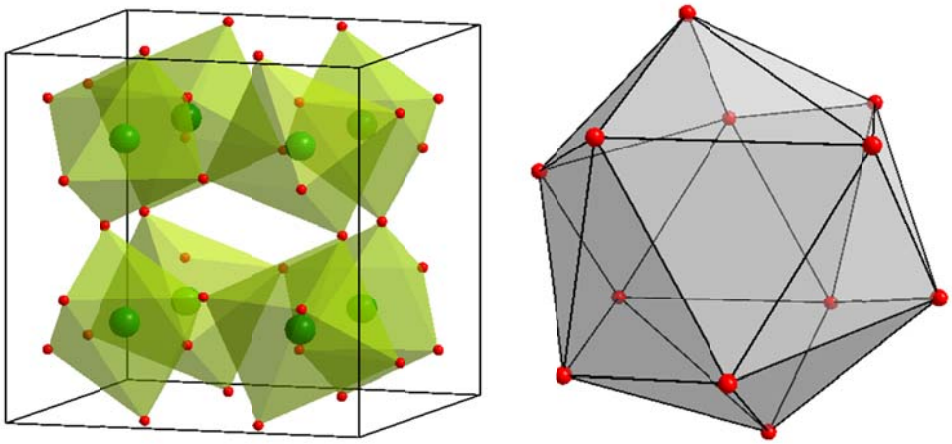

Figure 1.2 Crystal structure of cubic MX_3 (left) and the X_{12} icosahedron (right).

Clathrate is from Latin *clatratus* = encaged. Type-I clathrate with the general formula $X_2Y_6E_{46}$ (X = alkaline-earth elements, Y = Group XIII elements, Z = Group XIV elements) is a typical semi-conducting Zintl compound, where all E atoms possess four valence-electrons after absolute electron transfer from the X and Y atoms. The crystal structure of a typical type-I clathrate material $Ba_8Ga_{16}Si_{30}$ (space group $Pm\bar{3}n$) is shown in Figure 1.3. There are two smaller pentagonal dodecahedron (5^{12}) cages and six larger tetrakaidecahedron ($5^{12}6^2$) cages in the unit cell. In $Ba_8Ga_{16}Si_{30}$, Ba (2a site in the

dodecahedron and 6d site in the tetrakaidecahedron), Ga and Si will supply two, three, and four valence-electrons, respectively. Therefore, there are $8 \times 2 + 16 \times 3 + 30 \times 4 = 184$ valance electrons per formula unit.[21]

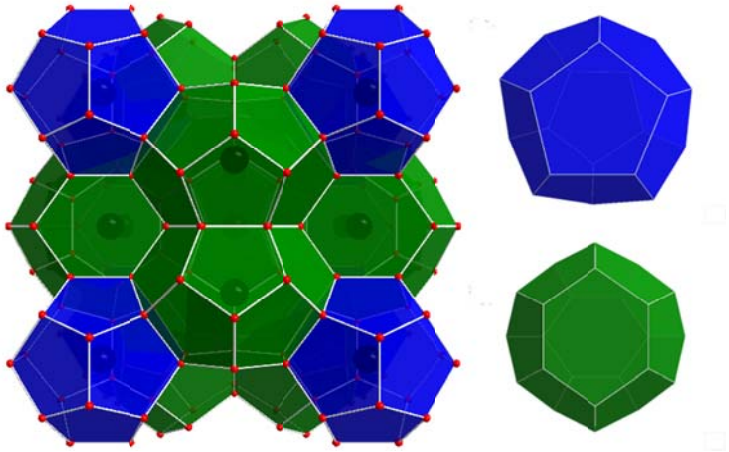

Figure 1.3 Crystal structure of cubic $Ba_8Ga_{16}Si_{30}$, Ba1-centered dodecahedron (top right) and Ba2-centered tetrakaidecahedron (bottom right).

Mo_3Sb_7 crystallizes in the cubic Ir_3Ge_7 type with space group $Im\bar{3}m$. Therein the Mo atoms are surrounded by eight Sb atoms in form of a square antiprism. Two such antiprisms share a common face formed by the Sb1 atoms (12*d* site) with Sb1–Sb1 contacts of the order of 3.4 Å, which occurs with a Mo–Mo bond of 3 Å through the $Sb1_4$ square. On the other side, the $Sb2_4$ square is connected to $Sb2_4$ square of the next pair of an $MoSb_8$ antiprism, forming Sb2–Sb2 contacts of about 3.1 Å along the edges of an empty Sb_8 cube.[21] Our results show that Ni atoms occupy the centers of the Sb_8 cubes in addition to partly substituting the Mo atoms (Figure 1.4), while the larger Fe atoms only replace Mo sites, i.e. do not occupy the cubic holes.[27, 28] For example, the Slater atomic radii are $r_{Mo} = 1.45$ Å, $r_{Fe} = 1.40$ Å, and $r_{Ni} = 1.35$ Å.[29] Partly filling these holes occurs with an enlarged unit cell of the Ni case, resulting in eight Ni–

Sb2 bonds of 2.693 Å, while the distance from that empty position to the Sb2 atoms in the Fe case is 2.678 Å. We speculate that Fe prefers the Mo site over the cubic site mostly because it is larger than Ni, and the eight *M*–Sb2 bonds are already somewhat short in case of *M* = Ni. This difference in site preferences may be the reason why more Fe than Ni can be incorporated into the Mo_3Sb_7 structure. [27, 28]

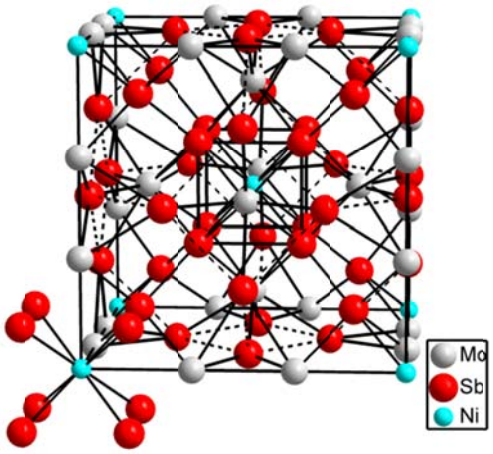

Figure 1.4 Crystal structure of $Ni_xMo_3Sb_7$, showing the Ni atoms at the origin in the cubic Sb_8 voids. Dashed lines emphasize the secondary Sb1–Sb1 contacts within the $Sb1_4$ squares.

1.4. Research on Thallium Tellurides

Great advancements were achieved in well-known bulk thermoelectric antimonides and chalcogenides.[26, 30-37] Meanwhile, several thallium-containing chalcogenides were synthesized and their potential for thermoelectric application evaluated. Almost all thallium tellurides exhibit an extremely low thermal conductivity of below 2.5 W $m^{-1}K^{-1}$ in a wide temperature range of ~300 K to ~700 K.[38-47] This was attributed to the fact that the compounds consist only of heavy elements, have extremely soft thallium bonding modes and have a large number of heavy elements per unit cell.

1.4.1. Ag_9TlTe_5, Tl_2SnTe_5 and Tl_2GeTe_5

Ag_9TlTe_5 has a zT of 1.23 at 700 K because of its extremely low glass-like thermal conductivity which is explained by the small average sound velocity (1203 ms^{-1}), Young's modulus (23.4 GPa) and Debye temperature (120 K) stemming from the weak interatomic bonding.[48] Tl_2SnTe_5 also exhibits an extremely low thermal conductivity and an impressively high zT (estimated to be 0.85 at 400 K), which is competitive to that of Bi_2Te_3. Neutron scattering experiments show that there are large atomic displacement parameters (ADPs) for the Tl ions and some of the Te atoms, which mean those atoms are weakly bonded in the structure, leading to the abnormally low lattice thermal conductivity.[49] Crystallographic details of Ag_9TlTe_5, Tl_2SnTe_5 and its analogue Tl_2GeTe_5 are summarized in Table 1.1.[49]

1.4.2. Modifications of Tl_5Te_3

The crystal structure and our own unpublished investigations on transport properties of Tl_5Te_3 are shown in Figure 1.5.[50] As seen from the figure, Tl_5Te_3 indeed possesses a low thermal conductivity (~ 3.0 W $m^{-1}K^{-1}$) and it is metallic with $\sigma = 2500\ \Omega^{-1}cm^{-1}$ and $\alpha = 18\ \mu V\ K^{-1}$ at 320 K.

Tl_9LaTe_6, Tl_9BiTe_6, Tl_9SbTe_6, Tl_4SnTe_3, and Tl_4PbTe_3 belong to a large group of ternary compounds, which can be derived from the isostructural Tl_5Te_3. Tl_9LaTe_6, Tl_9SbTe_6 and Tl_9BiTe_6 are ordered variants of Tl_5Te_3.[51] The Tl atoms occupy two sites, namely the Wyckoff positions 4*c* (Tl1) and 16*l* (Tl2) of space group *I*4/*mcm* (with four formula units of Tl_5Te_3 per unit cell). The La,[52, 53] Sb and Bi atoms then replace half of the Tl1 atoms on 4*c*. With Tl adopting the 1+ oxidation state and Te being 2−, these materials were calculated using density functional theory (DFT) [54, 55] methods to be semi-conducting (with band gaps < 0.5 eV), which is in accordance with the formulations $(Tl^+)_9La^{3+}(Te^{2-})_6$,[52] $(Tl^+)_9Sb^{3+}(Te^{2-})_6$ and $(Tl^+)_9Bi^{3+}(Te^{2-})_6$.[51] Our experiments showed that the formally undoped, electron

precise materials Tl_9BiTe_6 and Tl_9SbTe_6 are actually heavily doped, *p*-type semiconductors, with the electrical conductivity slowly decreasing with increasing temperature.

Table 1.1 Crystallographic details of Ag_9TlTe_5, Tl_2SnTe_5[56] and Tl_2GeTe_5[57]

Chemical formula	Ag_9TlTe_5	Tl_2SnTe_5	Tl_2GeTe_5
Formula weight [g/mol]	1813.20	1165.48	1119.41
Space group	$R\bar{3}c$	*I*4/*mcm*	*P*4/*mbm*
a [Å] = *b*	11.431	8.306	8.243
c [Å]	41.945	15.161	14.918
Z	12	4	4
ADPs(Å^2)*	–	Tl(1):0.017(0.026) Tl(2):0.047(0.049)	Tl(1):0.048(0.042) Tl(2):0.025(0.021)
X-ray density [g/cm^3]	–	7.40	7.34

*In each case, the second ADP value is from neutron diffraction data. ADP evaluates the mean-square displacement amplitude of an atom about its equilibrium position in a crystal.[58]

Böttcher et al. reported Tl_4SnTe_3 and Tl_4PbTe_3 to be ternary substitution variants of Tl_5Te_3 (In_5Bi_3 structure type, space group *I*4/*mcm*), where the *E* (= Sn, Pb) atoms occupy one Tl site, namely Tl1 on Wyckoff site 4*c*.[59, 60] As the second metal site, Tl2 on 16*l*, has a multiplicity of 16, compared to 4 for Tl1, the Tl : *E* ratio is 4 : 1 as in Tl_4ETe_3, when both metal sites are fully occupied by either Tl or *E* atoms. Then, all atoms can be in their most common oxidations states, resulting in the semiconducting charge-balanced formula $(Tl^+)_4E^{2+}(Te^{2-})_3$. The lattice parameters of Tl_5Te_3 and its modifications are presented in Table 1.2.

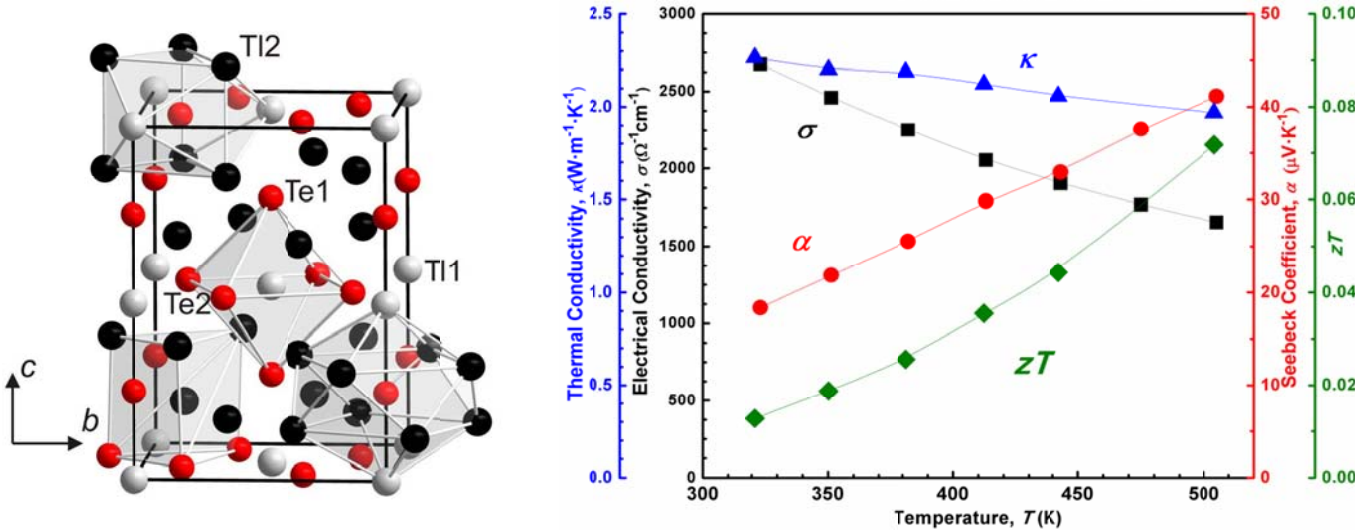

Figure 1.5 Crystal structure (left) and thermoelectric properties (right) of Tl_5Te_3.

Table 1.2 Lattice parameters of Tl_5Te_3 and its modifications (* reported by Böttcher et al.).

Parameter	Tl_5Te_3*	$Tl_{8.96}La_{1.04}Te_6$[48]	Tl_9SbTe_6	Tl_9BiTe_6*	Tl_4SnTe_3*	Tl_4PbTe_3*
a [Å]	8.930(2)	8.9220(4)	8.847(2)	8.855(2)	8.819(2)	8.841(2)
c [Å]	12.589(4)	13.156(1)	13.024(5)	13.048(4)	13.013(3)	13.056(3)
V [Å^3]	1003.9(5)	1047.2(1)	1019.4(6)	1023.1(5)	1012.1(4)	1020.4(4)

1.5. Scope of This Thesis

Prior to this work, several Tl_5Te_3-type ternary variants are reported to show great promise, like hot-pressed[61] as well as zone-refined Tl_9BiTe_6,[62] Tl_9SnTe_6 (zT = 0.17 at 572 K), Tl_9LaTe_6 (zT = 0.21 at 580 K),[52] Tl_9SbTe_6 (zT = 0.84 at 500 K), Tl_4SnTe_3 (zT = 0.74 at 673 K) and Tl_4PbTe_3 (zT = 0.71 at 673 K).[63] Tl_9BiTe_6 is one of the leading mid-temperature thermoelectrics, postulated to exceed zT = 1 above

450 K when prepared by zone-melting, and reaching zT = 0.86 at 560 K after hot-pressing due to its intrinsic low lattice thermal conductivity (< 0.4 $W \cdot m^{-1}K^{-1}$).

No data from off-stoichiometry materials such as $Tl_9Sb_{1-x}Te_6$ (with deficiencies on the Sb site), $Tl_{9-x}Sb_{1+x}Te_6$ (with a higher Sb/Tl ratio), $Tl_{10-x}Sn_xTe_6$ and $Tl_{10-x}Pb_xTe_6$ (with different *E*/Tl ratios) were known. In addition, disadvantageous high porosity (15% - 20%) was at least in part responsible for the relatively poor thermoelectric performance, causing additional charge carrier scattering at the grain boundaries.[64] Enhancement in thermoelectric performance is anticipated if the density is improved via an efficient consolidation and densification method. In this work, several series of the variants of Tl_5Te_3 have been prepared by hot-pressing and their crystal structure, electronic structure and high temperature electrical and thermal transport properties are investigated.

a) The effects of lanthanides on crystal structure and physical properties of Tl_9LnTe_6 (Ln = La, Ce, Pr, Nd, Sm, Gd, Tb) are analyzed. Thereafter, $Tl_{10-x}La_xTe_6$ (x = 0.90, 0.95, 1.00, 1.05, 1.10) are prepared aiming toward higher zT through composition optimization and measurement temperature range broadening. The effects of La contents on the unit cell volume and thermoelectric properties are also discussed. These results are published with me as first author in Journal of Alloys and Compounds.

b) The following samples $Tl_9Bi_{1-x}Te_6$ with $0 \le x \le 0.05$, $Tl_{9-x}Bi_{1+x}Te_6$ with $0 \le x \le 0.05$, $Tl_9Sb_{1-x}Te_6$ with $0 \le x \le 0.03$, and $Tl_{9-x}Sb_{1+x}Te_6$ with $0 \le x \le 0.03$ are investigated. A substantial improvement of the thermoelectric figure-of-merit, zT, is achieved in both the Bi and Sb systems over the previous data on hot-pressed Tl_9BiTe_6 and cold-pressed Tl_9SbTe_6, respectively. These results are published with me as first author in Chemistry of Materials.

c) To investigate the effects of Sn- and Pb-doping, several samples with the nominal composition $Tl_9Bi_{1-x}Sn_xTe_6$, $Tl_9Bi_{1-y}Pb_yTe_6$ ($0 \le x, y \le 0.15$), $Tl_9Sb_{1-m}Sn_mTe_6$ and $Tl_9Sb_{1-n}Pb_nTe_6$ ($0 \le m, n \le 0.10$) are prepared and their thermoelectric property measured. Considering that Sn and Pb have one valence

electron less than Sb and Bi, the Sn and Pb substitutions are expected to induce extrinsic *p*-type carriers in Tl_9SbTe_6 and Tl_9BiTe_6. Furthermore, the disorder of random atomic substitution may introduce mass and strain fluctuations in the material, which is expected to scatter the phonons, thereby decreasing the lattice thermal conductivity. These results are published with me as first author in Journal of Applied Physics.

d) $Tl_{10-x}Sn_xTe_6$ with $1.95 \leq x \leq 2.05$ and $Tl_{10-x}Pb_xTe_6$ with $1.90 \leq x \leq 2.05$ are investigated. The thermoelectric properties of both materials are presented in dependence of x in $Tl_{10-x}Sn_xTe_6$ and $Tl_{10-x}Pb_xTe_6$. Increasing x causes an increase in valence electrons, and thus a decrease in the dominating *p*-type charge carriers. Thusly, larger x values occur with a smaller electrical conductivity and a larger Seebeck coefficient. In each case, the lattice thermal conductivity remains under 0.5 W $m^{-1}K^{-1}$, resulting in several samples attaining the desired $zT_{max} > 1$. The highest values thus far are exhibited by $Tl_{8.05}Sn_{1.95}Te_6$ with $zT = 1.26$ and $Tl_{8.10}Pb_{1.90}Te_6$ with $zT = 1.46$ around 685 K. These results are published with me as first author in Advanced Energy Materials.

2. Experimental Methods

2.1. Preparation of the Samples

2.1.1. Synthesis

The starting materials were preserved in an argon-filled MBRAUN glove box. Both the oxygen and water contents are less than 0.1 ppm in the glove box, which helps to prevent the elements from oxidation. The elements were weighed according to the stoichiometric ratio, loaded into silica tubes, and then transferred to a vacuum line. The silica tubes were then sealed under a vacuum on the order of 10^{-3} mbar with an oxygen-hydrogen torch. The tubes were finally put into a programmable cube resistance furnace.

2.1.2. Consolidation

Primary techniques widely employed in the densification of thermoelectric materials include cold-pressing (CP), hot-pressing (HP) and spark plasma sintering (SPS). In HP the heat is provided by external heating elements, while in SPS the heat generation is internal. SPS applies large DC Pulsed Current to the powder materials in the die and generates sparks and thusly momentary ultra-high temperature between the powder particles, which will start the neck formation among the particles and develop the sintering process at lower temperature than traditional sintering methods. Here the samples are sintered by the Oxy-Gon FR-210-30T-ASA-160-EVC hot-press furnace system. The powder Is loaded into a graphite die and then pressed under a uniaxial pressure and Argon atmosphere. The details for the pressing process will be described briefly in each chapter.

2.2. Characterization and Measurement

2.2.1. X-ray Diffraction

X-rays are electromagnetic waves with wavelength of ~1 Ångström (1 Å = 10^{-10} m). X-ray diffraction experiments follow Bragg's law

$$2d \sin\theta = n\lambda \tag{2-1}$$

Here n is an integer, λ is the wavelength of incident wave, d is the spacing between the lattice planes, and θ is the angle between the incident beam and the scattering planes. An INEL powder diffractometer with position-sensitive detector and Cu Kα1 radiation is used for phase characterization herein.

In the late 1960s, Dr. Hugo Rietveld, a Dutch physicist, proposed a method to refine a crystal structure from its powder diffraction profile. The Rietveld method employs directly the individual intensities Y_i at each scattering angle (θ) from powder diffraction patterns and is a complex structure refinement and minimization procedure. The quantity minimised is in general form

$$S = \sum_{i=1}^{n} w_i \left[Y_i(obs) - Y_i(calc) \right]^2 = Minimum \tag{2-2}$$

n is the total number of points measured in the experimental powder diffraction pattern; Y_i(obs) is the observed intensity of the i^{th} data point; Y_i(calc) is the calculated intensity of the i^{th} data point; $w_i = 1/Y_i$(obs) is the weight of the i^{th} data point. In the process of obtaining a particular best refinement results, several parameters should be adjusted in the least squares refinement, including lattice parameters, atomic positions, site occupancies, thermal vibrational parameters, peak shape and width parameters, preferred orientation, and so on. The following figure-of-merits are customarily proposed to characterize the quality of the refinement.[65]

The profile residual (or reliability) factor, R_p:

$$R_{\mathrm{P}} = \frac{\sum_{i=1}^{n} \left| Y_{\mathrm{i}}(obs) - Y_{\mathrm{i}}(calc) \right|}{\sum_{i=1}^{n} Y_{\mathrm{i}}(obs)} \tag{2-3}$$

The weighted profile residual, R_{wp}:

$$R_{\mathrm{wp}} = \sqrt{\frac{\sum_{i=1}^{n} w_{\mathrm{i}} \left[Y_{\mathrm{i}}(obs) - Y_{\mathrm{i}}(calc) \right]^2}{\sum_{i=1}^{n} w_{\mathrm{i}} \left[Y_{\mathrm{i}}(obs) \right]^2}} \tag{2-4}$$

The Bragg residual, R_{B}:

$$R_{\mathrm{B}} = \frac{\sum_{j=1}^{m} \left| I_{\mathrm{j}}(obs) - I_{\mathrm{j}}(calc) \right|}{\sum_{j=1}^{m} I_{\mathrm{j}}(obs)} \tag{2-5}$$

The expected profile residual, R_{exp}:

$$R_{\mathrm{exp}} = \sqrt{\frac{n-p}{\sum_{i=1}^{n} w_{\mathrm{i}} \left[Y_{\mathrm{i}}(obs) \right]^2}} \tag{2-6}$$

The goodness of fit, χ^2(chi-squared):

$$\chi^2 = \left(\frac{R_{\mathrm{wp}}}{R_{\mathrm{exp}}} \right)^2 = \frac{\sum_{i=1}^{n} w_{\mathrm{i}} \left[Y_{\mathrm{i}}(obs) - Y_{\mathrm{i}}(calc) \right]^2}{n-p} \tag{2-7}$$

I_{j} (obs) is the 'observed' integrated intensity of the j^{th} Bragg peak, which has been calculated after the observed intensity of every data point in the powder diffraction profile has been portioned according to the calculated intensities of the contributing Bragg peaks; I_{j} (calc) is the calculated integrated intensity of the Bragg peak; m is the number of independent Bragg reflections; p is the number of free least squares parameters. All figures-of-merit except R_{B} include a contribution from the background. Here Rietveld

refinements were performed using the General Structure Analysis System (GSAS)[66] via the graphical interface EXPGUI.[67]

2.2.2. Single Crystal X-ray Diffraction

The single crystal measurements were carried out on a Bruker Kappa APEX II diffractometer with graphite-monochromatic Mo Kα (λ = 0.71073 Å) radiation. The crystal is centered by changing its position along the *X*, *Y* and *Z* direction. The SMART software integrated into the APEX2 package is utilized for data collection. After corrections for Lorentz and polarization effects, the data were corrected for absorption by fitting a function to the empirical transmission surface as sampled by multiple equivalent measurements using SADABS and the structure solution and refinements performed with the SHELXTL package.[68] The internal residual value (R_{int}) is used to determine the quality of data collected.

$$R_{\text{int}} = \frac{\sum \left| F_{\text{O}}^2 - F_{\text{mean}}^2 \right|}{\sum F_{\text{O}}^2} \tag{2-8}$$

R_{int} depends on the observed structure factor, F_O. The square roots of the corrected data yields the observed structure factor,

$$\left| F_{(\text{hkl})} \right| = \sqrt{\frac{KI_{(\text{hkl})}}{L_{\text{P}}}} \tag{2-9}$$

where K is a scaling factor and L_P is the Lorentz (geometric) correction and polarization correction parameter. Because our materials are composed by heavy atoms, the chosen method for solving crystal structures was the direct method.

The quality of the refinement is evaluated by R factor (R_1) and weighted R factor (wR_2) defined as

$$R_1 = \frac{\sum \left| \left(|F_{\text{O}}| - |F_{\text{C}}| \right) \right|}{\sum |F_{\text{O}}|} \tag{2-10}$$

$$wR_2 = \sqrt{\frac{\sum w(F_O^2 - F_C^2)^2}{\sum w(F_O^2)^2}} \quad (2\text{-}11)$$

with F_O and F_C the observed and calculated structure factors, respectively. w is the weighting parameter.

2.2.3. Scanning Electron Microscopy

Scanning electron microscopy (SEM) has been proven to be effective in studying the texture (sizes, shapes), topography, surface and fracture features of powders or bulk pieces.[69] SEM mainly works in the reflection mode and has the resolution in the range of ~100 nm to ~1000 nm. Energy Dispersive X-ray analysis (EDX) is an analytical technique commonly comes with SEM. Selected pellets were analyzed after the hot-pressing procedure by energy dispersive X-ray spectroscopy (Zeiss, with integrated EDAX Pegasus 1200 detector) using an acceleration voltage of 25 kV.

2.2.4. Electronic Structure Calculation

Electronic structure calculation is of great importance to understand and predict the properties of the materials. Electronic structure of a compound could be obtained from first principles, in which process not any adjustable parameters are involved. One just needs to input the electronic charge, electron mass, atomic numbers, and masses of the atoms of the material, since all the properties arise from the interaction between the nuclei and the electrons. Nuclei obey classical mechanics; by contrast, electrons are governed by quantum mechanics.[70]

DFT proposed by Kohn and Hohenberg in 1964 presented a huge breakthrough with respect to the handling of electron-electron interaction. The ground-state density of electrons plays a fundamental role in the DFT. DFT is computationally inexpensive because the density has only three degrees of freedom, in contrast to 3N for the many-body wave function. DFT is based on two theorems: (1) the

external potential is a functional of the ground-state density, which means density is the fundamental variable; (2) the total energy is lowest for the right ground-state density. In 1965 Kohn and Sham showed that the right electron density can be obtained by a one-electron equation (Kohn-Sham equation).[71] The Kohn-Sham equation is described below:

$$\left[-\frac{\hbar^2}{2m}\nabla^2+\underbrace{\upsilon(\vec{r})+\upsilon_H(\vec{r})+\upsilon_{XC}(\vec{r})}_{\upsilon_{eff}(\vec{r})}\right]\psi_i(\vec{r})=\varepsilon_i\psi_i(\vec{r}) \tag{2-12}$$

$$\upsilon_H(\vec{r})=\int\frac{e^2}{4\pi\varepsilon_0}\frac{n(r')}{\left|\vec{r}-\vec{r}'\right|}d^3r' \tag{2-13}$$

where *m* denotes the electron mass; $\vec{r}$ the position of an electron. The Kohn-Sham equation is similar to Hartree or Hartree-Fock method but this includes the effects of exchange and correlation. Some approximation should be used to solve the Kohn-Sham equation for the exchange-correlation potential $\upsilon_{XC}(\vec{r})$ is unknown. The simplest approximation is the local density approximation (LDA), which has been proved efficient in most cases. However, sometimes it overestimates binding energy and underestimates the bond lengths and thus the lattice constants. To rectify these problems, to some extent, Perdew developed generalized gradient approximation (GGA) in 1991.[72] When it comes to band gaps in semiconductors and insulators, both LDA and GGA will yield comparatively small values.

There are many other methods to solve the Kohn-Sham equation to obtain the band structure for a periodic solid. Augmented plane wave (APW) method proposed by Slater (1937) is one the oldest methods and remains one of the accurate methods to calculate energy bands. The method uses the muffin-tin form of the electron-ion potential. The potential around an ion is hypothetically considered to be spherically symmetric within a sphere of radius (the muffin-tin radius) and is constant in the interstitial area.

Another method using the potential in the muffin-tin form is the Korringa-Kohn-Rostoker (KKR) method using a Green's function formulation. Both AWP and KKR methods are capable of calculating accurately, but they are time-consuming to obtain self-consistent calculations since they involve a complicated, non-linear energy dependent secular matrix. In 1975, Andersen developed the linear augmented plane wave (LAPW) method and the linear muffin tin orbital (LMTO) method to solve the band structure in a more efficient way. Nowadays it is feasible to get rid of the muffin-tin approximation and use full-potential (FP). The methods using FP form are FP-LAWP and FP-LMTO. The tight-binding (TB) method or the linear combination of atomic orbitals (LCAO) method that uses tightly bound atomic orbitals as bases has also been developed to obtain the band structure. The LMTO method cast in the TB form is called the TB-LMTO method. Nonetheless, most of the LMTO calculations have been performed using the atomic-spheres-approximation (ASA) in which muffin-tin spheres are blown up until overlapping and volume-filling spheres are utilised.[73]

2.3. Measurements of Physical Properties

2.3.1. Electrical Resistivity and Seebeck Coefficient Measurement

The electrical resistivity and Seebeck coefficient were measured on ZEM-3 (ULVAC-RIKO, Inc). The two *R*-type thermocouples are spring-mounted and pressed onto the pellet with a uniform pressure ensuring good near-ohmic contacts, but sufficiently gentle to avoid damage. In the electrical resistivity measurement, a constant current is applied to the sample and the voltage drop between the same wires of the thermocouple is determined by subtracting the thermo-electromotive force between leads. After the sample is heated to and held at a programed temperature, the lower block is heated to provide a temperature gradient. Seebeck coefficient is obtained by measuring the upper and lower temperatures

and thermal electromotive force between the same wires of the thermocouples.

2.3.2. Thermal Conductivity Determination

Thermal conductivity is determined by the measurement of thermal diffusivity (λ), specific heat (C_P) and density (ρ_m):

$$\kappa = \lambda \rho_m C_P \tag{2-14}$$

One of the widely used methods to measure thermal diffusivity is the laser flash method. Thin disks or squares are selected for the measurement. One face of the sample is irradiated by a pulsed laser and an infrared detector observes the temperature fluctuation of the rear face. The time $t_{1/2}$, taken to reach one-half of the steady-state temperature rise, is employed to calculate the thermal diffusivity.

$$\lambda = \frac{1.37 d^2}{\pi^2 t_{1/2}} \tag{2-15}$$

where d is the thickness of the sample. The thermal diffusivity measurements were carried out on the Flash Line 3000 (ANTER Corp.) with a Xenon flash lamp.

The specific heat is calculated following the Dulong-Petit law, $C_P = 3R/M_{avg}$, where R is the gas constant and M_{avg} the average molar mass. The Dulong-Petit values often serve as a good approximation in particular at low temperatures, while experimental data are often difficult to be reliably obtained.[74] For validation, temperature dependent C_P values for Tl_9BiTe_6 were calculated using the Neumann-Kopp[75, 76] law with the experimental data on Tl_2Te and Bi_2Te_3. Those data yielded slightly higher C_P with increasing temperature, e.g. by 9% at 500 K.

The densities of the pellets were determined with a Sartorius® mechatronics density determination kit following the Archimedes' method. The densities were calculated from

$$\rho = \frac{W(\mathrm{a})\left[\rho(\mathrm{fl}) - \rho(\mathrm{a})\right]}{0.99983\left[W(\mathrm{a}) - W(\mathrm{fl})\right]} + \rho(\mathrm{a}) \tag{2-16}$$

where W(a) is the weight of the pellet in the air, W(fl) is the weight of the pellet in liquid (water or ethanol), ρ(fl) is the density of the liquid and ρ(a) = 0.0012 g/cm^3 the density of the air under standard conditions (293.15 K, 101.325 kPa). 0.99983 is used to eliminate the error caused by depth of immersion.

3. Thermoelectric Properties of Tl_9LnTe_6 (Ln = La, Ce, Pr, Nd, Sm, Gd, Tb) and $Tl_{10-x}La_xTe_6$

3.1. Introduction

Previously, a series of Tl_9LnTe_6 (Ln = rare earth elements), isostructural to Tl_9BiTe_6, were prepared by the cold-pressing and sintering method and their electrical and thermal properties determined.[53] Here the Tl_9LnTe_6 (Ln = La, Ce, Pr, Nd, Sm, Gd, Tb) series was revisited at first. Samples with relatively high densities were obtained by hot-pressing. Their crystal structure and thermoelectric properties were also measured and analyzed, with La turning out to be forming the best Tl-Ln telluride of this series. Subsequently, $Tl_{10-x}La_xTe_6$ (x = 0.90, 0.95, 1.00, 1.05, 1.10) with various Tl/La ratios were prepared with the hope of further optimizing thermoelectric properties through adjusting carrier concentration.

3.2. Experimental Process

Samples with the nominal composition Tl_9LnTe_6 (Ln = La, Ce, Pr, Nd, Sm, Gd, Tb) and $Tl_{10-x}La_xTe_6$ (x = 0.90, 0.95, 1.00, 1.05, 1.10) were prepared from the starting materials (Tl granules, 99.9%, Strem Chemicals; La, ingots, 99.9%; Ce ingots, 99.9%; Pr powder, −40 mesh, 99.9%; Nd, powder, −40 mesh, 99.9%; Sm powder, −40 mesh, 99.9%; Gd, powder, −40 mesh, 99.9%; Tb, powder, −40 mesh, 99.9%;Te broken ingots, 99.99+%, Strem Chemicals). To prevent the reaction between the silica and the rare earth elements, the fused silica tubes were coated with carbon film formed by the decomposition of ethanol. The samples then were gradually heated to 1200 K within 24 hours, kept at

this temperature for 30 hours, gradually cooled down to 673 K within 160 hours, followed by switching off the furnace. The hot-press sintering pressure, sintering temperature and sintering time are 45 MPa, 613 K and 1.5 hours, respectively. Rietveld refinements were performed on Tl_9LaTe_6, Tl_9CeTe_6, Tl_9PrTe_6, $Tl_{9.05}La_{0.95}Te_6$, and $Tl_{8.95}La_{1.05}Te_6$ based on the Tl_9BiTe_6 model.

3.3. Results and Discussion

The Powder XRD results, Rietveld refinements and thermoelectric properties of the thallium lanthanide tellurides compounds are discussed separately in this section. Firstly, we present the results for Tl_9LnTe_6 (Ln = La, Ce, Pr, Nd, Sm, Gd, Tb), and then we show the effects of the Tl/La ratio on the crystal structure and thermoelectric properties of $Tl_{10-x}La_xTe_6$.

3.3.1. Powder XRD Results and Rietveld Refinements of Tl_9LnTe_6

Figure 3.1 shows the room temperature powder XRD patterns of Tl_9LnTe_6 (Ln = La, Ce, Pr, Nd, Sm, Gd, Tb). The XRD patterns reveal that the samples from Tl_9LaTe_6 to Tl_9TbTe_6 give patterns similar to that of Tl_9BiTe_6 (PDF No. 84-2448). No impurity diffraction peaks were observed except for a tiny amount of $La_{3-y}Te_4$ found in Tl_9LaTe_6. An attempt to prepare "Tl_9YbTe_6" yielded a pattern corresponding to that of Tl_5Te_3 with presence of YbTe, which agrees well with the observations from Babanly et al. who reported that "Tl_9YbTe_6" could not have been prepared.[77]

Crystallographic details of Tl_9LaTe_6, Tl_9CeTe_6 and Tl_9PrTe_6 are presented in Table 3.1. The unit cell volumes of Tl_9PrTe_6 (1038.42(2) $Å^3$) and Tl_9CeTe_6 (1032.98(2) $Å^3$) are smaller than that of Tl_9LaTe_6 (1049.65(2) $Å^3$), as expected based on lanthanide contraction with the radii of La^{3+}, Ce^{3+} and Pr^{3+} ions being 103 pm, 102 pm, and 99 pm, respectively. However, it is interesting to note that Tl_9CeTe_6 has a

smaller unit cell than Tl_9PrTe_6. This shrinkage could be attributed to the existence of Ce^{3+} and Ce^{4+} ions, which was deduced from a comparatively lower magnetic moment in Tl_9CeTe_6.[78]

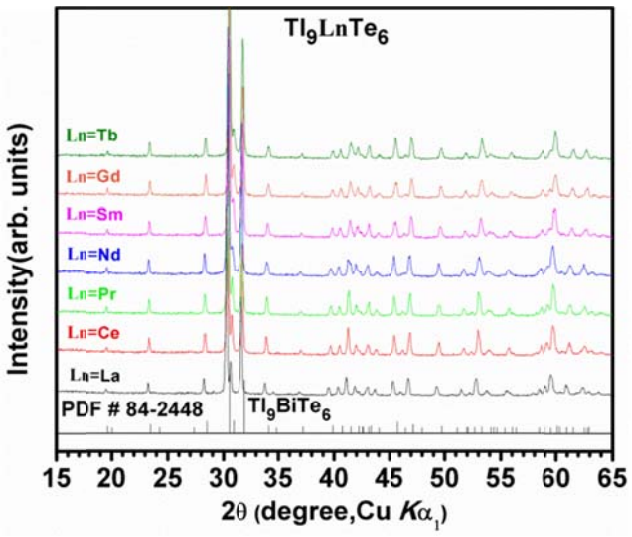

Figure 3.1. Room temperature powder XRD patterns of Tl_9LnTe_6 (Ln = La, Ce, Pr, Nd, Sm, Gd, Tb).

Table 3.1 Crystallographic information for Tl_9LaTe_6, Tl_9CeTe_6 and Tl_9PrTe_6

Chemical formula	Tl_9LaTe_6	Tl_9CeTe_6	Tl_9PrTe_6
M [g/mol]	2743.96	2745.17	2745.97
$a = b$ [Å]	8.93175(8)	8.8879(1)	8.9055(1)
c [Å]	13.1575(2)	13.0765(2)	13.0934(2)
V [Å^3]	1049.65(2)	1032.98(2)	1038.42(2)
Z	2	2	2
$R_P{}^a$ \ $R_B{}^b$	0.055 \ 0.077	0.061 \ 0.094	0.062 \ 0.114

[a] $R_P = \Sigma|y_o - y_c| / \Sigma|y_o|$ [b] $R_B = \Sigma|I_o - I_c| / \Sigma|I_o|$

3.3.2. Thermoelectric Properties of Tl_9LnTe_6

The thermoelectric properties of Tl_9LnTe_6 (Ln = La, Ce, Pr, Nd, Sm, Gd, Tb) are presented in Figure 3.2, and the values at 315 K and at 550 K shown in Table 3.2. Figure 3.2(a) reveals the temperature dependence of the electrical conductivity of all Tl_9LnTe_6 samples. In each case, σ decreases monotonously with increasing temperature, typical for heavily doped semiconductors. While these materials are formally charge-balanced, *p*-type defects are often observed in such heavy metal tellurides, as also found in Bi_2Te_3 and Tl_9BiTe_6, causing a large number of carriers (> 10^{19} cm^{-3}) to be present without thermal activation.

Across the thallium lanthanide telluride series, σ gradually increases from σ = 190 $\Omega^{-1}cm^{-1}$ for Tl_9LaTe_6 to 1039 $\Omega^{-1}cm^{-1}$ for Tl_9TbTe_6 at 315 K, i.e. from the left to the right in the Periodic Table. This evolution could be readily interpreted in terms of that the band gaps (E_g) of these Tl_9LnTe_6 compounds decrease across the series. The smaller energy gap makes it easier for intrinsic carriers to transit from the valence band to the conduction band, leading to an increased σ.[53] The σ values of Tl_9SmTe_6 (e.g., 942 $\Omega^{-1}cm^{-1}$ at 315 K) are an exception to the general trend across the series, as they are higher than the ones of the representative to its right, Tl_9GdTe_6 with σ = 884 $\Omega^{-1}cm^{-1}$ at 315 K. It is reasonable to attribute this discontinuity (a difference of 7%) to an experimental error, for example a slightly higher Tl : Sm ratio or lower Tl : Gd ratio than planned or from the determination of the electrical conductivity itself, usually estimated to have an error of ±5%. The latter seems less likely here, because the same discontinuity is also found in the Seebeck coefficient and thermal conductivity.

Typically the sample with a higher electrical conductivity is accompanied by a lower Seebeck coefficient. This principle is indeed true for the thallium lanthanide telluride series investigated here, as shown in Figure 3.2(b). All samples have positive α values, implying the dominant carriers in the

compounds are holes. In addition, the Seebeck coefficient α increases with the increasing temperature. At around 315 K, α gradually decreases from 125 μV K^{-1} for Tl_9LaTe_6, to 53 μV K^{-1} for Tl_9TbTe_6.

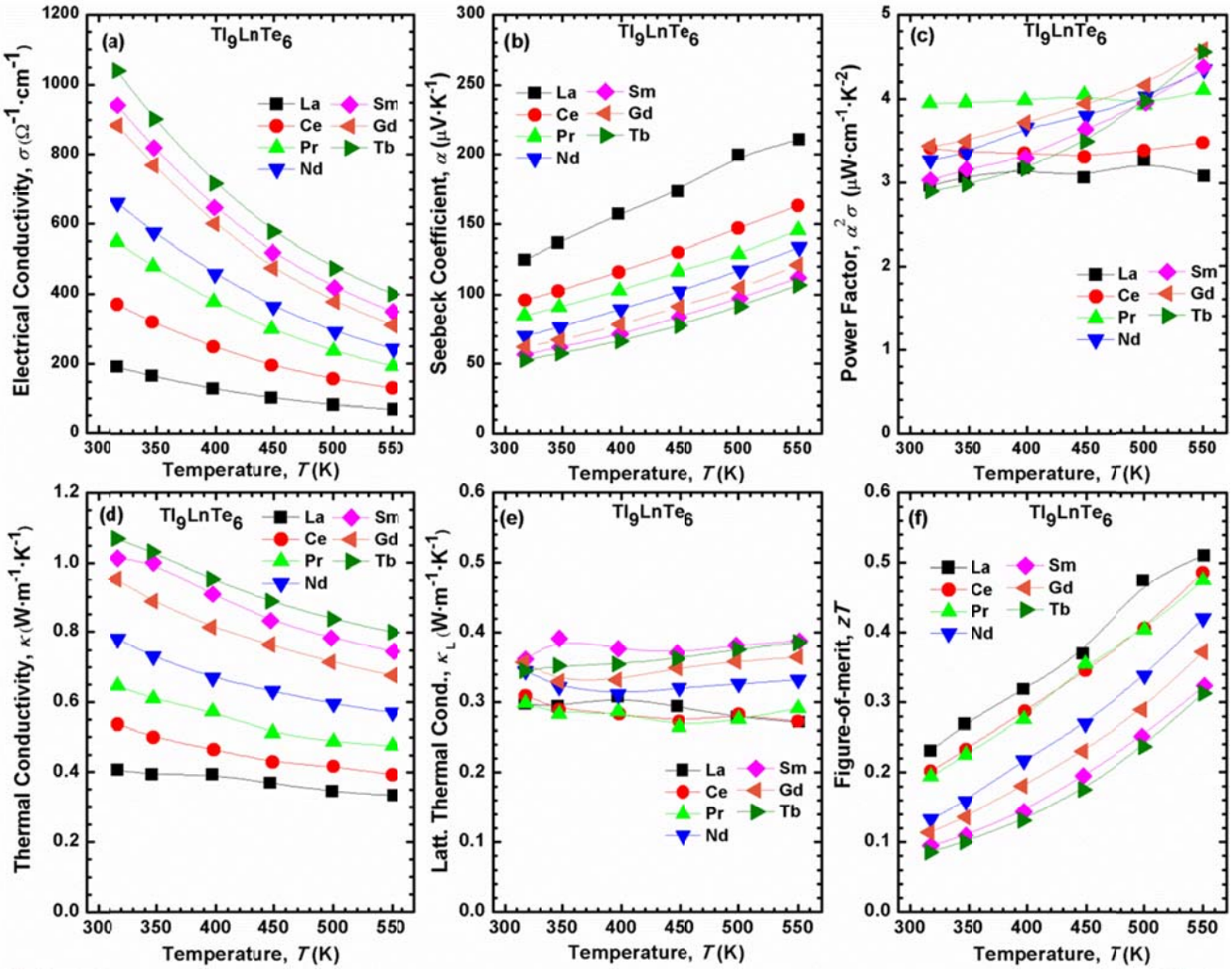

Figure 3.2 Temperature dependence of the thermoelectric properties for Tl_9LnTe_6 (Ln = La, Ce, Pr, Nd, Sm, Gd, Tb), (a) electrical conductivity, (b) Seebeck coefficient, (c) power factor, (d) thermal conductivity, (e) lattice thermal conductivity, (f) dimensionless figure-of-merit, *zT*. The solid line is a guide for the eye.

Table 3.2 Thermoelectric properties of various Tl_9LnTe_6 samples at 315 K and at 550 K.

Sample	σ ($\Omega^{-1}cm^{-1}$)	α ($\mu V\ K^{-1}$)	*P.F.* ($\mu W\ cm^{-1}K^{-2}$)	κ ($W\ m^{-1}K^{-1}$)	κ_L ($W\ m^{-1}K^{-1}$)	zT
Ln = La	190 \ 69	125 \ 211	3.0 \ 3.1	0.41 \ 0.33	0.30 \ 0.27	0.23 \ 0.51
Ln = Ce	371 \ 130	96 \ 163	3.4 \ 3.5	0.54 \ 0.39	0.31 \ 0.27	0.20 \ 0.49
Ln = Pr	550 \ 193	85 \ 146	3.9 \ 4.1	0.65 \ 0.48	0.30 \ 0.29	0.19 \ 0.47
Ln = Nd	661 \ 243	70 \ 134	3.3 \ 4.3	0.78 \ 0.57	0.34 \ 0.33	0.13 \ 0.42
Ln = Sm	942 \ 350	57 \ 112	3.0 \ 4.4	1.01 \ 0.75	0.36 \ 0.39	0.09 \ 0.32
Ln = Gd	884 \ 312	62 \ 121	3.4 \ 4.6	0.95 \ 0.68	0.36 \ 0.36	0.11 \ 0.37
Ln = Tb	1039 \ 401	53 \ 107	2.9 \ 4.6	1.07 \ 0.80	0.35 \ 0.39	0.09 \ 0.31

The power factor, $P.F. = \alpha^2\sigma$, for these thallium lanthanide tellurides is depicted in Figure 3.2(c). Here the temperature dependence of these compounds could be categorized into two groups. Tl_9LaTe_6, Tl_9CeTe_6 and Tl_9PrTe_6 exhibit only a very small temperature dependence in the whole temperature range, while the *P.F.* values of the other samples rise in a similar fashion to α. All the *P.F.* values fall in the range of 2.8 $\mu W\ cm^{-1}K^{-2}$ to 4.6 $\mu W\ cm^{-1}K^{-2}$ across the lanthanide series from La to Tb. At around 550 K, the *P.F.* increases from 3.1 $\mu W\ cm^{-1}K^{-2}$ for Tl_9LaTe_6 to 4.6$\mu W\ cm^{-1}K^{-2}$ for Tl_9GdTe_6 and Tl_9TbTe_6.

The thermal conductivity data are plotted in Figure 3.2(d). Similar to the electrical conductivity, the thermal conductivity decreases with increasing temperature and increases across the lanthanide series. From Tl_9LaTe_6 to Tl_9TbTe_6, all samples display a general low thermal conductivity ($\kappa < 1.1\ W\ m^{-1}K^{-1}$), which gradually decreases with increasing temperature. Generally speaking, samples with larger electrical conductivity exhibit higher thermal conductivity because κ_E is proportional to σ via the

Wiedemann-Franz law $\kappa_E = L\sigma T$.[10] For instance, κ increases from 0.40 W $m^{-1}K^{-1}$ of Tl_9LaTe_6 to 1.07 W $m^{-1}K^{-1}$ of Tl_9TbTe_6 at 325 K, correlating well to the changes in electrical conductivity.

To further understand the effect of lanthanide on the lattice thermal conductivity, κ_L, we calculated κ_L via $\kappa_L = \kappa - \kappa_E$. The Lorenz number L was calculated under the single parabolic band and acoustic phonon scattering (scattering parameter $\lambda = -0.5$) assumption.[79] The calculated lattice thermal conductivity is illustrated in Figure 3.2(e). From Tl_9LaTe_6 to Tl_9TbTe_6, all samples exhibit very low κ_L values, consistently below 0.4 W $m^{-1}K^{-1}$. Moreover, the κ_L curves are very flat, which is characteristic of compounds with the thermal conductivity approaching the phonon-glass limit. The same κ_L behavior was also found in the Sn- and Pb- doped Tl_9BiTe_6 and Tl_9SbTe_6.[80] As also can be observed from Figure 3.2(e), Tl_9LaTe_6, Tl_9CeTe_6 and Tl_9PrTe_6 exhibit the lowest κ_L; Tl_9SmTe_6, Tl_9GdTe_6 and Tl_9TbTe_6 show higher κ_L without a clear trend; Tl_9NdTe_6 has a κ_L in between. Theoretically, the increase in atomic mass across the period should decrease κ_L, while the decrease in Tl : Ln mass fluctuation from Tl_9LaTe_6 to Tl_9TbTe_6 should cause an increase in κ_L. To some extent, the experimental results are consistent with this mass fluctuation theory, although the parameter associated with the point defect scattering is small.

The dimensionless thermoelectric figure-of-merit zT was calculated via $zT = T\alpha^2\sigma/\kappa$ and summarized in Figure 3.2(f). It was observed that zT increases with increasing T. Across the series from Tl_9LaTe_6 to Tl_9TbTe_6, a decrease in zT is observed. Tl_9LaTe_6 has the largest zT values (0.23 – 0.51) among them, whilst Tl_9TbTe_6 has the minimum (0.09 – 0.31). In short, the formally electron-precise material Tl_9LaTe_6 performs best, reaching $zT = 0.51$ around 550 K, which is almost 2.5 times the value obtained from the cold-pressed and sintered Tl_9LaTe_6.[50] Its substantially higher thermoelectric figure-of-merit benefits significantly from the consolidation method, which yielded 98% of the theoretical density. By contrast, the cold-pressed La sample has a density of only 80%.[52]

3.3.3. Powder XRD Results and Rietveld Refinements of $Tl_{10-x}La_xTe_6$

Figure 3.3 shows the room temperature powder XRD patterns of $Tl_{10-x}La_xTe_6$ (x = 0.90, 0.95, 1.00, 1.05, 1.10). Impurity diffraction peaks from $La_{3-x}Te_4$ were observed when x = 1.00 and 1.10. Noting there is a larger amount of $La_{3-x}Te_4$ when x = 1.10, its thermoelectric properties will not be incorporated here.

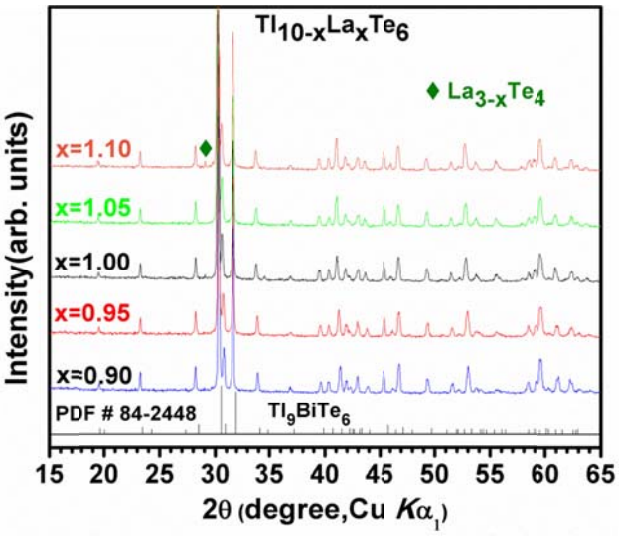

Figure 3.3 Room temperature powder XRD patterns of $Tl_{10-x}La_xTe_6$ (x = 0.90, 0.95, 1.00, 1.05, 1.10).

Crystallographic details of $Tl_{10-x}La_xTe_6$ (x = 0.95, 1.00, 1.05) are listed in Table 3.3. As x increases, the lattice parameter a decreases slightly while c increases more significantly; thus the unit cell volume also increases from 1047.78(2) $Å^3$ when x = 0.95 to 1050.25(1) $Å^3$ when x = 1.05. Similar observations have been made for $Tl_{9.52}Ho_{0.48(4)}Te_6$ and $Tl_{9.24}Ho_{0.76(8)}Te_6$ as well as for $Tl_{8.98}Nd_{1.02(6)}Te_6$ and $Tl_{8.68}Nd_{1.32(6)}Te_6$.[53] This trend could be explained on the basis that the smaller Tl ions are replaced by the larger Ln ions, and that the change is anisotropic because the (Tl/Ln)Te_6 "octahedron" becomes more

regular with increasing Ln content, because of the decreasing effect of the lone pair of Tl^+, as previously discussed in the $Tl_{10-x}La_xTe_6$ cases.[52]

Table 3.3 Crystallographic information for $Tl_{9.05}La_{0.95}Te_6$, Tl_9LaTe_6 and $Tl_{8.95}La_{1.05}Te_6$

Chemical formula	$Tl_{9.05}La_{0.95}Te_6$	Tl_9LaTe_6	$Tl_{8.95}La_{1.05}Te_6$
M [g/mol]	2747.23	2743.96	2740.68
$a = b$ [Å]	8.9379(1)	8.93175(8)	8.92966(8)
c [Å]	13.1160(3)	13.1575(2)	13.1712(2)
V [Å^3]	1047.78(2)	1049.65(2)	1050.25(1)
Z	2	2	2
$R_P{}^a$ \ $R_B{}^b$	0.066 \ 0.127	0.055 \ 0.077	0.051 \ 0.075

[a] $R_P = \Sigma|y_o - y_c| / \Sigma|y_o|$ [b] $R_B = \Sigma|I_o - I_c| / \Sigma|I_o|$

3.3.4. Thermoelectric Properties of $Tl_{10-x}La_xTe_6$

The temperature and composition dependence of the thermoelectric properties of $Tl_{10-x}La_xTe_6$ (x = 0.90, 0.95, 1.00, 1.05) are shown in Figure 3.4, and the values at 315 K and 600 K are listed in Table 3.4. Larger x, i.e. a higher La content, occurs with a higher number of electrons and thus fewer charge carriers (holes). The electrical conductivity σ thusly declines with increasing La content/decreasing hole concentration (Figure 3.4(a)). For example, at 315 K, the $Tl_{10-x}La_xTe_6$ sample with x = 0.90 exhibits a σ value of 470 $\Omega^{-1}cm^{-1}$, compared to only σ = 100 $\Omega^{-1}cm^{-1}$ for x = 1.05. The samples with x = 0.90 and x = 0.95 display a sharply decreasing σ with increasing T, in contrary the other two samples exhibit a small change in the magnitude. As an illustration, σ of Tl_9LaTe_6 slowly decreases from σ = 195 $\Omega^{-1}cm^{-1}$ at 315

K to 70 $\Omega^{-1}cm^{-1}$ at 600 K, while σ of $x = 0.90$ drops rapidly from 467 $\Omega^{-1}cm^{-1}$ to 176 $\Omega^{-1}cm^{-1}$.The room temperature σ value of Tl_9LaTe_6 is comparable with the one of hot-pressed Tl_9BiTe_6 (σ = 193 $\Omega^{-1}cm^{-1}$).[61]

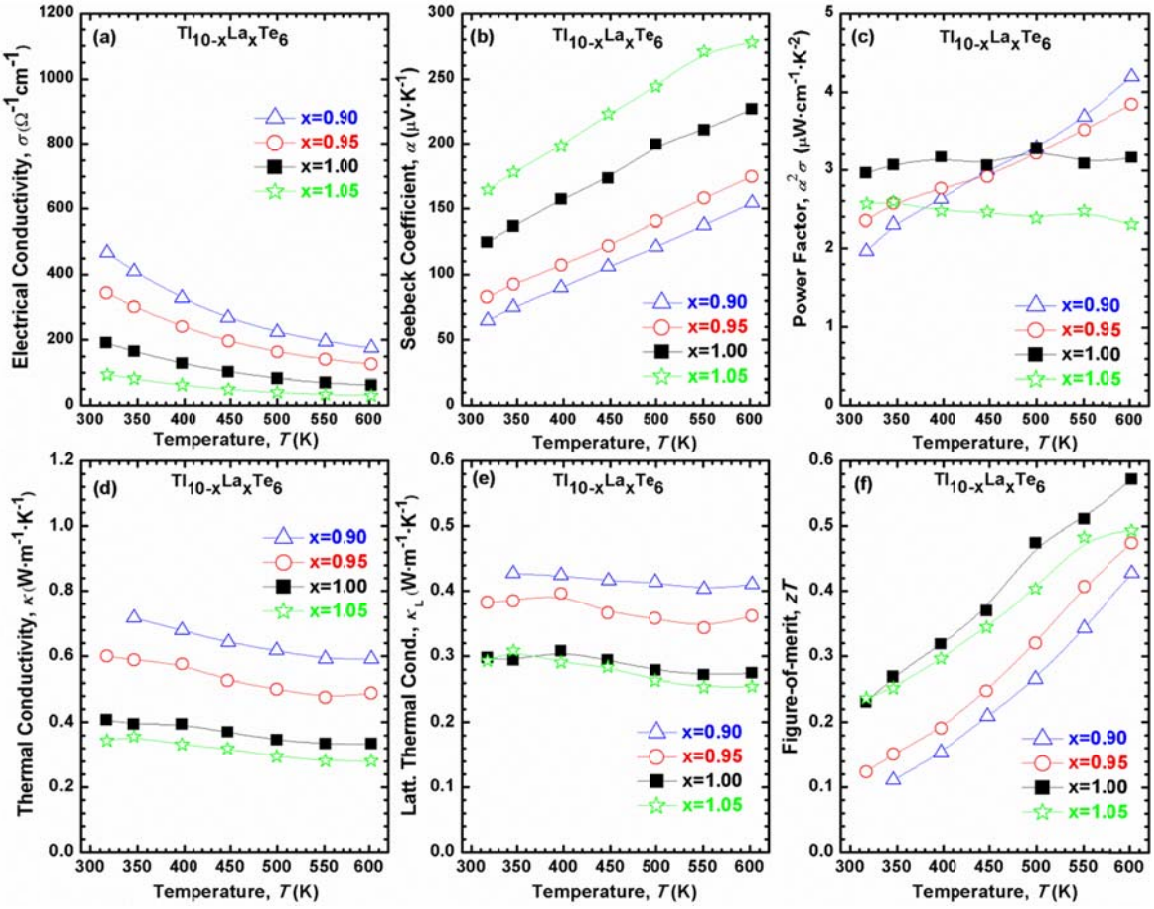

Figure 3.4 Temperature dependence of the thermoelectric properties for $Tl_{10-x}La_xTe_6$ (x = 0.90, 0.95, 1.00, 1.05). (a) electrical conductivity (b) Seebeck coefficient (c) power factor (d) thermal conductivity (e) lattice thermal conductivity (f) dimensionless figure-of-merit, zT. The solid lines are guides for the eye.

According to the results of the electrical conductivity measurements, α is anticipated to rise with increasing La concentration as well as with increasing temperature. In fact, both trends are observed clearly in Figure 3.4(b). Electronic structure calculations imply that as x increases in $Tl_{10-x}La_xTe_6$, a transition from metallic ($x = 0$) to *p*-doped semiconducting ($x < 1$) then to *n*-doped semiconducting ($x > 1$) behavior is anticipated.[52] This *p*-*n* transition has been demonstrated in $Tl_{9-x}Bi_{1+x}Te_6$.[81] In the cases studies here, α increases from $\alpha = +83$ μV K^{-1} when $x = 0.95$ to $\alpha = +165$ μV K^{-1} when $x = 1.05$ at 300 K. Even though the specimen with $x = 1.05$ is expected to be a *n*-type semiconductor, its positive sign of the Seebeck coefficient indicates hole conduction is dominant in the sample, probably due to defects in the structure, or possible due to small side products such as $La_{3-x}Te_4$ not observed in the X-ray diagram, which affect the Tl : La ratio of the main product.

Table 3.4 Thermoelectric properties of various $Tl_{10-x}La_xTe_6$ samples at 315 K and at 600 K.

Sample	σ ($\Omega^{-1}cm^{-1}$)	α (μV K^{-1})	*P.F.* (μW $cm^{-1}K^{-2}$)	κ (W $m^{-1}K^{-1}$)	κ_L (W $m^{-1}K^{-1}$)	*zT*
$x = 0.90$	467 \ 176	64 \ 154	2.0 \ 4.2	- \ 0.60	- \ 0.41	- \ 0.42
$x = 0.95$	343 \ 126	83 \ 175	2.4 \ 3.8	0.60 \ 0.49	0.38 \ 0.36	0.12 \ 0.47
$x = 1.00$	190 \ 62	125 \ 227	3.0 \ 3.2	0.41 \ 0.33	0.30 \ 0.27	0.23 \ 0.57
$x = 1.05$	94 \ 30	165 \ 278	2.6 \ 2.3	0.34 \ 0.28	0.29 \ 0.25	0.24 \ 0.49

Figure 3.4(c) presents the overall electrical performance (power factor) for the samples. Samples $x = 1.00$ and 1.05 with low electrical conductivity exhibit power factors with slight temperature dependence, similar to Tl_9CeTe_6 and Tl_9PrTe_6. On the other hand, $x = 0.90$ and $x = 0.95$ have *P.F.* values ascend in a similar fashion to α.

The total thermal conductivity κ consists of the electronic and the lattice contribution. It is reasonable to assume that samples with the larger electrical conductivity exhibit larger κ, as expected according to the Wiedemann-Franz law.[10] Figure 3.4(d) shows that κ values around 0.4 W $m^{-1}K^{-1}$ were obtained when x = 1.00 and x = 1.05, which are close to those determined for zone-refined Tl_9BiTe_6 (κ = 0.46 W $m^{-1}K^{-1}$)[62] and hot-pressed Tl_9BiTe_6 (κ = 0.39 W $m^{-1}K^{-1}$).[61]

It could be concluded from Figure 3.4(e) that the lattice thermal conductivity are weakly dependent on the temperature, as evidenced by the relatively flat curve for each case. Samples with higher amount of La show lower values of lattice thermal conductivity, suggesting that the higher mass of La, compared to Tl, results in lower κ_L.

In the end, zT values calculated from the measured α, σ, and κ are plotted in Figure 3.4(f). In the whole temperature range, zT first increases with x increasing from 0.90 to 1.00, then it drops moderately for x = 1.05 in spite of a lower thermal conductivity (0.36 – 0.28 W $m^{-1}K^{-1}$). Tl_9LaTe_6 with a low thermal conductivity (< 0.4 W $m^{-1}K^{-1}$) was bestowed with the highest zT = 0.57 at 600K in this work.

3.4. Conclusions

p-Type polycrystalline thallium lanthanide tellurides with the nominal composition Tl_9LnTe_6 (Ln = La, Ce, Pr, Nd, Sm, Gd, Tb) and $Tl_{10-x}La_xTe_6$ (x = 0.90, 0.95, 1.00, 1.05) have been successfully fabricated by a combination of the melting-slow cooling-down process and hot-pressing technique. Their crystal structure, high temperature electrical and thermal transport properties were investigated.

These compounds are isostructural to Tl_9BiTe_6, crystallizing in the space group *I*4/*mcm*. Rietveld refinement results show that Tl_9CeTe_6 has an exceptionally small unit cell volume of 1032.98(2) $Å^3$, and the unit cell expands with increasing La contents in $Tl_{10-x}La_xTe_6$.

The electrical conductivity and thermal conductivity increase across the lanthanide series. On the other hand, the Seebeck coefficient values decrease with Ln varying from La to Tb. Tl_9SmTe_6 appears to be the exception of these general trends. Possessing the lowest thermal conductivity (0.33 – 0.41 W m^{-1} K^{-1}), Tl_9LaTe_6 has the largest figure-of-merit, zT = 0.51 at 550 K (and 0.57 at 600 K).

As for the $Tl_{10-x}La_xTe_6$ (x = 0.90, 0.95, 1.00, 1.05) series, the electrical conductivity, thermal conductivity and lattice thermal conductivity decrease with the increasing lanthanum contents and the opposite trend is observed for the Seebeck coefficient. The highest zT = 0.57 is realized for Tl_9LaTe_6 at 600 K.

4. Thermoelectric Properties of Variants of Tl_9SbTe_6 and Tl_9BiTe_6

4.1. Introduction

It is not a coincidence that state-of-the-art thermoelectric materials include elements from the 6th period (such as Ba, La, Yb, Pb, Bi), as heavy elements are known to contribute to low thermal conductivity, an important asset of enhanced thermoelectrics. This appears to be particularly true for materials containing thallium, as toxic as they may be.[52, 61, 63, 82, 83] In particular, Tl_9BiTe_6 exhibits high zT values at intermediate temperatures, namely zT = 0.86 at 590 K after hot-pressing,[61] and even up to (extrapolated) zT = 1.2 at 500 K after zone-refining.[62] Its lighter homologue, Tl_9SbTe_6, was investigated as well prior to this work, and reported to achieve zT = 0.41 at 591 K after cold-pressing and sintering.[84] With this contribution, we demonstrate that Tl_9SbTe_6 can yield zT values around unity as well, and that the thermoelectric properties of both Tl_9SbTe_6 and Tl_9BiTe_6 can be further improved by varying the Tl/E ratio with E = Sb, Bi.

4.2. Experimental Procedures

The compounds were synthesized from the respective elements stored in an argon-filled glove box (Tl granules, 99.9%, Strem Chemicals; Sb powder, 99.5%, -100 mesh, Alfa Aesar; Bi granules, 99.997%, 1 – 2 mm, Alfa Aesar; Te broken ingots, 99.99+%, Strem Chemicals). The evacuated and sealed ampoules were gradually heated to 923 K within 12 hours in a resistance furnace, held at 923 K for 24 hours, and then slowly cooled down to 703 K within 120 hours, followed by switching off the furnace to cool down to room temperature.

The following samples were investigated: $Tl_9Bi_{1-x}Te_6$ with $0 \le x \le 0.05$, $Tl_{9-x}Bi_{1+x}Te_6$ with $0 \le x \le 0.05$, $Tl_9Sb_{1-x}Te_6$ with $0 \le x \le 0.03$, and $Tl_{9-x}Sb_{1+x}Te_6$ with $0 \le x \le 0.03$. Larger x values were not attempted, because the Bi samples with $x > 0.03$ showed a decrease in performance. No additional phases were detected in any of the samples discussed here, except for very minor once in the case of $Tl_{8.95}Bi_{1.05}Te_6$, indicative of the formation of $TlBiTe_2$. The X-ray patterns are shown in Figure 4.1.

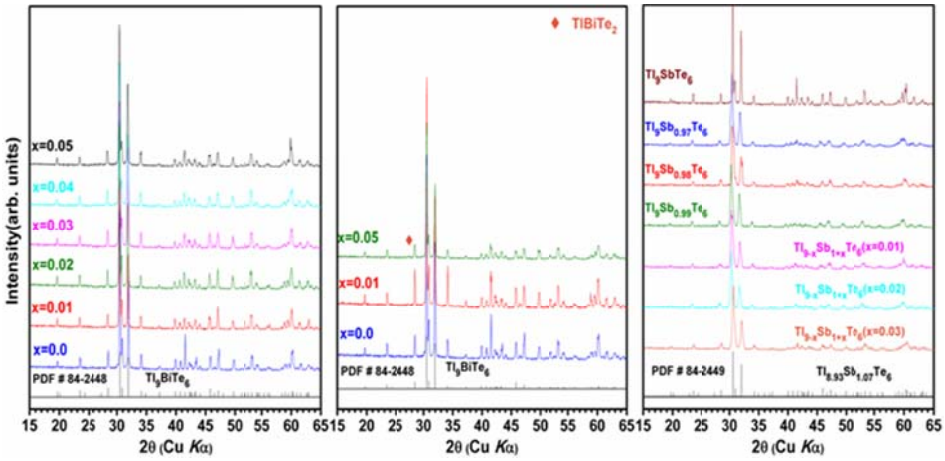

Figure 4.1 XRD patterns of $Tl_9Bi_{1-x}Te_6$, $Tl_{9-x}Bi_{1+x}Te_6$, $Tl_9Sb_{1-x}Te_6$ and $Tl_{9-x}Sb_{1+x}Te_6$.

All samples were sintered under a flow of argon at 45 MPa at 523 K for a period of 90 minutes. The electrical properties were measured perpendicular to the pressing direction, and the thermal diffusivity parallel. This may constitute a problem in case of anisotropic samples that exhibit strong texture effects such as Bi_2Te_3,[85] but we did not observe texture effects for these materials. We measured the electrical conductivity perpendicular to the first measurements, i.e. across the long bar and thus parallel to the pressing direction, and obtained the same value within error, namely $\sigma = 230\ \Omega^{-1}cm^{-1}$ *vs.* 210 $\Omega^{-1}cm^{-1}$ at 300 K for a pellet of Tl_9BiTe_6, noting that the dimensions of this perpendicular measurements cannot be determined as precisely because of the short distance between the contacts. No

impurity elements were detected, and the distribution of the elements appeared to be homogenous as far as detectable using SEM (Figure 4.2).

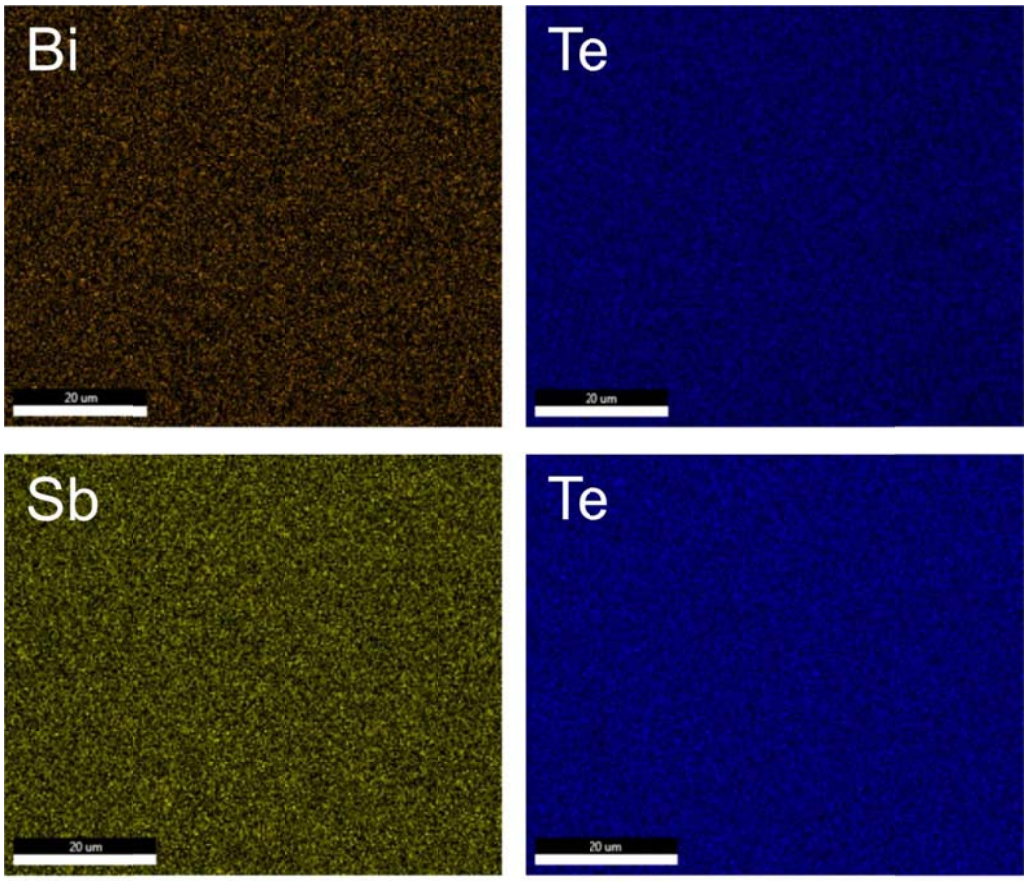

Figure 4.2 SEM maps of Tl_9BiTe_6 (top) and Tl_9SbTe_6 (bottom).

4.3. Results and Discussion

Figure 4.3 reveals the data determined on the $Tl_9Bi_{1-x}Te_6$ samples in our laboratory. Moreover, the numbers from Kurosaki (hot-pressed)[61] and Wölfing (zone-refined)[62] were added to these graphs in form of dashed and solid lines, respectively. Increasing x, i.e. increasing the Bi deficiency, is expected to increase the number of holes, the dominant charge carriers according to the earlier reports. This expected

trend is experimentally observed: with increasing x, the electrical conductivity (at 325 K) increased from $\sigma = 180\ \Omega^{-1}\text{cm}^{-1}$ when $x = 0$ stepwise to $370\ \Omega^{-1}\text{cm}^{-1}$ when $x = 0.05$. With an estimated relative error of 5%, these differences are significant.

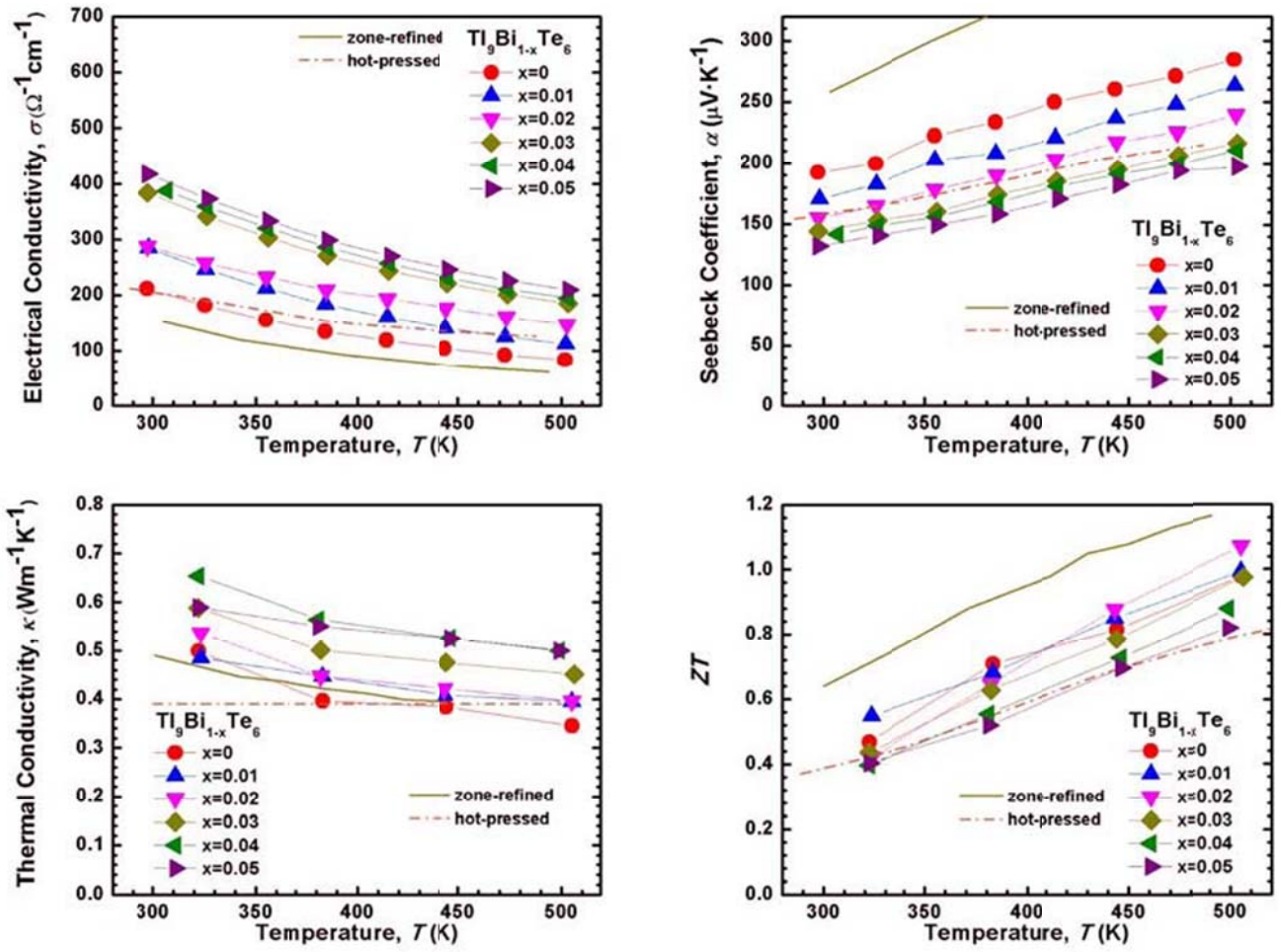

Figure 4.3 Thermoelectric properties of $Tl_9Bi_{1-x}Te_6$. Top left: electrical conductivity; top right: Seebeck coefficient; bottom left: thermal conductivity; bottom right: figure-of-merit.

While these measurements commenced at 300 K, we choose 325 K at the minimum temperature for all comparisons because no thermal conductivity data were obtained below 325 K, noting that the electrical conductivity is highest at the lowest temperature in every case. The thermoelectric properties of

the $Tl_9Bi_{1-x}Te_6$ samples with $0 \le x \le 0.05$ at 325 K and at 500 K are summarized in Table 4.1.

Table 4.1 Thermoelectric properties of various $Tl_9Bi_{1-x}Te_6$ samples at 325 K (first value) and at 500 K (second value).

Property	$x = 0$	$x = 0.01$	$x = 0.02$	$x = 0.03$	$x = 0.04$	$x = 0.05$
$\alpha/(\mu V\ K^{-1})$	200 \ 285	183 \ 263	164 \ 239	153 \ 216	149 \ 211	141 \ 198
$\sigma/(\Omega^{-1}cm^{-1})$	182 \ 83	246 \ 112	258 \ 147	342 \ 185	360 \ 195	373 \ 210
$P.F./(\mu W\ cm^{-1}K^{-2})$	7.2 \ 6.7	8.2 \ 7.8	7.0 \ 8.4	8.0 \ 8.7	7.9 \ 8.7	7.4 \ 8.2
$\kappa/(W\ m^{-1}K^{-1})$	0.50 \ 0.35	0.48 \ 0.40	0.54 \ 0.40	0.59 \ 0.45	0.65 \ 0.50	0.59 \ 0.50
zT	0.47 \ 0.98	0.55 \ 0.99	0.42 \ 1.07	0.44 \ 0.98	0.40 \ 0.88	0.40 \ 0.82

Like in the earlier reports, the conductivity values of the samples measured here decrease steadily with increasing temperature (top left of Figure 4.3), parallel to the zone-refined Tl_9BiTe_6, whereas the decrease of Kurosaki's hot-pressed sample is smaller. As a consequence, it compares well to our Tl_9BiTe_6 at low temperature and to our $Tl_9Bi_{0.99}Te_6$ above 420 K. The smaller temperature dependence may be caused by (less temperature dependent) more grain boundary scattering of Kurosaki's hot-pressed sample, although its density was given to be 98% of the maximum as well.[61] The combination thereof (more scattering, same density) implies smaller grain sizes. Its slightly higher conductivity at 325 K of 190 $\Omega^{-1}cm^{-1}$, compared to 180 $\Omega^{-1}cm^{-1}$, would then be caused by a larger carrier concentration. In contrast, the zone-refined sample has the lowest values here (140 $\Omega^{-1}cm^{-1}$ at 325 K),[62] while one could postulate that it should have the smallest dependence on grain boundaries because of its preparation directly from the melt. In that case, this sample would have the smallest number of charge carriers, and thus the largest

Seebeck coefficient, which does not depend as strongly on grain boundary scattering.

This is indeed the case, as revealed in the Seebeck curves shown in the top right part of Figure 4.3: the zone-refined Tl_9BiTe_6 sample has the largest Seebeck coefficient, namely α = +280 μV K^{-1} at 325 K, compared to Kurosaki's +160 μV K^{-1} and our +200 μV K^{-1}.[61, 62] It is therefore likely that our sample of the same nominal composition actually has an intermediate carrier concentration. Moreover, increasing the Bi deficiency and thusly the number of *p*-type carriers leads to a steady decline of the Seebeck coefficient, e.g. from +200 μV K^{-1} when x = 0 down to 140 μV K^{-1} when x = 0.05. Assuming experimental errors of 3% (smaller than in case of the conductivity, as the numbers do not depend on the dimension measurements), the Seebeck values are generally significantly different as well, aside from the samples with x = 0.03 and x = 0.04 (+153 μV K^{-1} vs. +149 μV K^{-1}). In each case, the Seebeck coefficient increases almost linearly with increasing temperature, and all curves run parallel - with the exception of the zone-refined sample.

Overall, the electrical performances of these samples are very comparable, and show little temperature dependence, as expressed in the numerator of the figure-of-merit, the power factor *P.F.* = $\alpha^2\sigma$. This is a consequence of the opposing trends in both the values and the temperature dependence of α and σ. At 325 K, the *P.F.* varies from 7.0 μW $cm^{-1}K^{-2}$ when x = 0.02 to 8.2 μW $cm^{-1}K^{-2}$ when x = 0.01, compared to minimal and maximal values of 6.7 μW $cm^{-1}K^{-2}$ when x = 0 and 8.7 μW $cm^{-1}K^{-2}$ when x = 0.03 and x = 0.04 at 500 K. For comparison, the literature *P.F.* values of the zone-refined and hot-pressed Tl_9BiTe_6 samples are *P.F.* = 10.7 μW $cm^{-1}K^{-2}$ and 5.1 μW $cm^{-1}K^{-2}$ at 325 K,[61, 62] respectively, with the *P.F.* curves displaying comparably flat slopes. Thusly, our samples here all perform better electrically than Kurosaki's hot-pressed Tl_9BiTe_6, independent of the exact Bi content, and worse than the zone-refined material.[61, 62]

The thermal conductivity data are depicted in the bottom left part of Figure 4.3. All samples show overall low thermal conductivity (< 0.7 W $m^{-1}K^{-1}$) in accord with earlier data, which slowly decreases with increasing temperature. The differences between the various samples are less distinct than in the electrical conductivity data because of the smaller importance of the charge carrier concentration. Generally, the samples with larger Bi deficiency (having larger electrical conductivity, σ) exhibit higher thermal conductivity, κ, as well, but there are exceptions, most notably at the lower temperatures. At 325 K, κ increases from 0.48 W $m^{-1}K^{-1}$ when $x = 0.01$ to 0.65 W $m^{-1}K^{-1}$ when $x = 0.04$, but one should note that the $x = 0$ sample as well as the $x = 0.05$ are very close to the minimal and maximal value, respectively, in part within the assumed error of 5%.

To gain insight into the effect of the different carrier concentrations on κ, we estimated their contribution to the thermal conductivity via the Wiedemann-Franz law, $\kappa_E = L\sigma T$,[10] with L = Lorenz number, using the value for non-degenerate semiconductors of 1.5×10^{-8} W Ω K^{-2}. This results in κ_E values between 0.09 W $m^{-1}K^{-1}$ ($x = 0$) and 0.18 W $m^{-1}K^{-1}$ ($x = 0.05$) at 325 K. The lattice contribution to the thermal conductivity, $\kappa_L = \kappa - \kappa_E$, thus varies between κ_L = 0.36 W $m^{-1}K^{-1}$ and 0.41 W $m^{-1}K^{-1}$, confirming the exceptionally low values published before for these materials, namely κ_L = 0.30 W $m^{-1}K^{-1}$ for Kurosaki's hot-pressed Tl_9BiTe_6 and κ_L = 0.39 W $m^{-1}K^{-1}$ for the zone-refined Tl_9BiTe_6 (all numbers extrapolated for 325 K using the same Lorenz number)[61, 62] noting that many thermoelectric materials including Bi_2Te_3 and PbTe typically exhibit values above 1 W $m^{-1}K^{-1}$. While the lower κ_L of Kurosaki's hot-pressed Tl_9BiTe_6 can be understood by larger grain boundary scattering as postulated above,[61] all these values come close to the so-called minimum thermal conductivity for a fully disordered solid composed of the elements Tl-Bi-Te, which was calculated to be around κ_{min} = 0.2 W $m^{-1}K^{-1}$.[62]

Finally, the figure-of-merit, zT, was calculated for all samples using the experimentally determined thermal conductivity data and polynomial fits for the power factor, which was obtained for a larger range of temperature than κ. Thus, no extrapolation was necessary. All zT values increase approximately linearly with increasing temperature, e.g. for Tl_9BiTe_6 from 0.47 at 325 K up to 0.98 at 500 K. This compares favorably with Kurosaki's hot-pressed Tl_9BiTe_6 (0.40 – 0.78),[61] but remains behind the zone-refined material (0.72 – 1.0 at 430 K, extrapolated to 1.2 at 500 K).[62] According to Kurosaki's data, zT is expected to continue to increase up to 591 K for these materials, with the melting point being around 813 K.[61] While different Bi deficiencies lead to quite different transport properties, the zT values are all comparable, and do not follow any clear trend. The two best samples in this series are $Tl_9Bi_{0.99}Te_6$, with zT varying from 0.55 to 0.99, and $Tl_9Bi_{0.98}Te_6$, with zT values of 0.42 – 1.1.

From the above-mentioned experimental errors, the error in zT follows to be around 8%. Within those 8%, several of the $Tl_9Bi_{1-x}Te_6$ samples have equivalent zT values, and the best one reaches about 90% of zT_{max} of the zone-refined sample,[62] i.e. its zT_{max} does not differ significantly assuming a comparable error for the zone-refined sample. On the other hand, most of these samples are significantly better than the Tl_9BiTe_6 hot-pressed by Kurosaki et al.,[61] with an improvement of up to 1.1/0.78 = 41% at 500 K.

To investigate the impact of a reduction of the charge carriers as well, we tried to increase the Bi content in Tl_9BiTe_6 by replacing more Tl atoms according to the formula $Tl_{9-x}Bi_{1+x}Te_6$. As shown in the top left of Figure 4.4 in comparison to the data of Tl_9BiTe_6 already presented in Figure 4.3, the electrical conductivity decreases with increasing x as expected, from 180 $\Omega^{-1}cm^{-1}$ when $x = 0$ down to 80 $\Omega^{-1}cm^{-1}$ when $x = 0.01$ and even down to only 1.8 $\Omega^{-1}cm^{-1}$ when $x = 0.05$ at 325 K. The initial carrier concentration of the $x = 0.05$ sample is so small that the electrical conductivity increases with increasing

temperature due to the activation of the intrinsic carriers. This sample actually exhibits a negative Seebeck coefficient between 300 K and 450 K, which then turns positive above 450 K (top right of Figure 4.4). Because of its low electrical conductivity, the electronic contribution to the thermal conductivity is negligible, with $\kappa_E \approx 0.001$ W m^{-1}K^{-1}. Therefore its thermal conductivity of $\kappa = 0.34$ W m^{-1}K^{-1} (bottom left of Figure 4.4) equals the lattice thermal conductivity, κ_L.

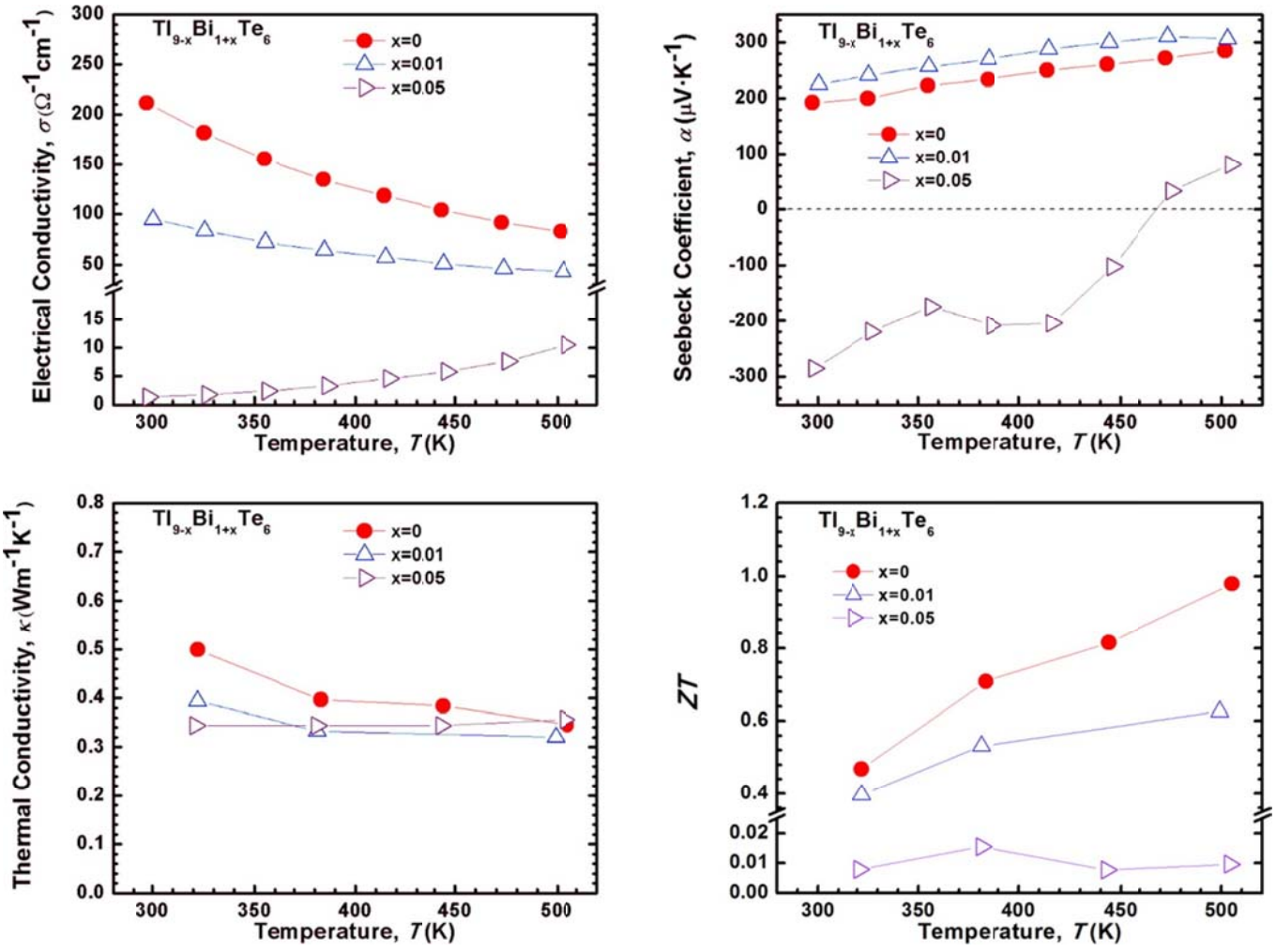

Figure 4.4 Thermoelectric properties of $Tl_{9-x}Bi_{1+x}Te_6$. Top left: electrical conductivity; top right: Seebeck coefficient; bottom left: thermal conductivity; bottom right: figure-of-merit.

Decreasing the carrier concentration of stoichiometric Tl_9BiTe_6 is disadvantageous with respect to the thermoelectric performance, because of a large drop in the power factor below 5 μW $cm^{-1}K^{-2}$ when $x = 0.01$ and 0.02 μW $cm^{-1}K^{-2}$ when $x = 0.05$, yielding significantly lower zT values (bottom right of Figure 4.4).

In analogy to Figure 4.3, the thermoelectric key properties of the Tl_9SbTe_6 variants are summarized in Figure 4.5. All seven Sb samples investigated are included in one figure, using filled symbols for the $Tl_9Sb_{1-x}Te_6$ series and open symbols for the $Tl_{9-x}Sb_{1+x}Te_6$ series. In contrast to the Bi-containing materials, no clear trends were detected. This may be a consequence of experimental error (including the weighing) combined with the smaller ranges of both x and the properties. For example at 325 K, the electrical conductivity values range from $\sigma = 420$ $\Omega^{-1}cm^{-1}$ to 530 $\Omega^{-1}cm^{-1}$ (Tables 4.2 and 4.3), compared to the range of 180 $\Omega^{-1}cm^{-1}$ to 370 $\Omega^{-1}cm^{-1}$ for $Tl_9Bi_{1-x}Te_6$ and to 1.8 $\Omega^{-1}cm^{-1}$ for $Tl_{8.95}Bi_{1.05}Te_6$. Likewise, the range of the Seebeck coefficient is much smaller for $Tl_9Sb_{1-x}Te_6$ ($\alpha = +105$ μV K^{-1} – $\alpha = +120$ μV K^{-1}at 325 K) than for $Tl_9Bi_{1-x}Te_6$ (+140 μV K^{-1} – +210 μV K^{-1} at 325 K). Overall, the changes with increasing temperature are comparable, namely decreasing σ and increasing α, and the electrical performance, i.e. the power factor, is similar, stemming from generally higher σ and lower α of the Sb-containing samples. For example, the maximum *P.F.* of the Sb series is almost identical to the one of the Bi series: 8.5 μW $cm^{-1}K^{-2}$ for $Tl_9Sb_{0.98}Te_6$ vs. 8.7 μW $cm^{-1}K^{-2}$ for both $Tl_9Bi_{0.97}Te_6$ and $Tl_9Bi_{0.96}Te_6$, all reached at $T = 500$ K. Moreover, *P.F.* steadily increases with increasing temperature for the Sb series, but not for the Bi series. Last, the power factor of the cold-pressed and sintered Tl_9SbTe_6 reported earlier [84] is significantly lower with approximately 6.0 μW $cm^{-1}K^{-2}$ at 500 K, culminating in 6.5 μW $cm^{-1}K^{-2}$ at 591 K.

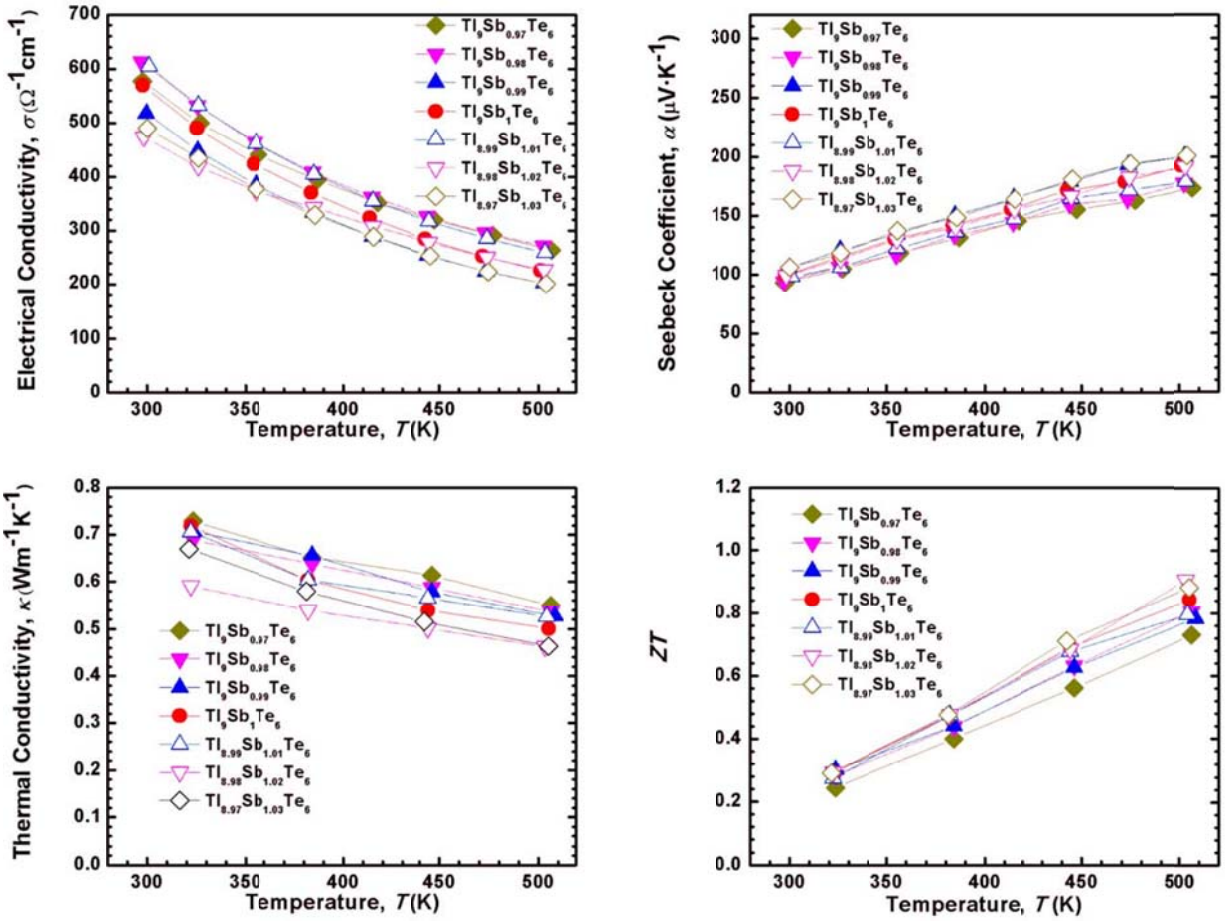

Figure 4.5 Thermoelectric properties of $Tl_9Sb_{1-x}Te_6$ and $Tl_{9-x}Sb_{1+x}Te_6$. Top left: electrical conductivity; top right: Seebeck coefficient; bottom left: thermal conductivity; bottom right: figure-of-merit.

The thermal conductivity, on the other hand, is across the board larger in case of the Sb samples, for example $\kappa = 0.72$ W m^{-1}K^{-1} for Tl_9SbTe_6 vs. 0.50 W m^{-1}K^{-1} for Tl_9BiTe_6 (both at 325 K). This is a consequence of a larger electronic contribution ($\kappa_E = 0.24$ W m^{-1}K^{-1} vs. 0.09 W m^{-1}K^{-1}) stemming from the larger electrical conductivity as well as larger lattice thermal conductivity ($\kappa_L = 0.48$ W m^{-1}K^{-1} vs. 0.41 W m^{-1}K^{-1}). The latter observation indicates that the heavier mass of Bi outweighs the larger mass fluctuation of Sb and Tl (40% mass difference) on the 4*c* site, compared to Bi and Tl (2% mass difference).

Table 4.2 Thermoelectric properties of various $Tl_9Sb_{1-x}Te_6$ samples at 325 K (first value) and at 500 K (second value).

Property	$x = 0$	$x = 0.01$	$x = 0.02$	$x = 0.03$
$\alpha/(\mu V\ K^{-1})$	115 \ 192	121 \ 200	107 \ 177	105 \ 173
$\sigma/(\Omega^{-1}cm^{-1})$	490 \ 226	449 \ 203	532 \ 272	500 \ 265
$P.F./(\mu W\ cm^{-1}K^{-2})$	6.5 \ 8.4	6.6 \ 8.1	6.0 \ 8.5	5.5 \ 7.9
$\kappa/(W\ m^{-1}K^{-1})$	0.72 \ 0.50	0.71 \ 0.53	0.69 \ 0.54	0.72 \ 0.54
zT	0.29 \ 0.84	0.30 \ 0.78	0.28 \ 0.81	0.24 \ 0.73

Table 4.3 Thermoelectric properties of various $Tl_{9-x}Sb_{1+x}Te_6$ samples at 325 K (first value) and at 500 K (second value).

Property	$x = 0$	$x = 0.01$	$x = 0.02$	$x = 0.03$
$\alpha/(\mu V\ K^{-1})$	115 \ 192	106 \ 179	113 \ 191	118 \ 200
$\sigma/(\Omega^{-1}cm^{-1})$	490 \ 226	532 \ 260	419 \ 227	435 \ 201
$P.F./(\mu W\ cm^{-1}K^{-2})$	6.5 \ 8.4	6.0 \ 8.3	5.4 \ 8.3	6.1 \ 8.1
$\kappa/(W\ m^{-1}K^{-1})$	0.72 \ 0.50	0.71 \ 0.53	0.59 \ 0.46	0.67 \ 0.46
zT	0.29 \ 0.84	0.27 \ 0.80	0.29 \ 0.90	0.29 \ 0.88

Overall, the zT values of the $Tl_9Sb_{1-x}Te_6$ series appear to be slightly lower than those of the Bi samples, in particular at lower temperatures, with zT_{max} values ranging from around 0.73 to 0.84 at 500 K, compared to 0.82 to 1.1 at 500 K for $Tl_9Bi_{1-x}Te_6$. On the other hand, the Sb-rich samples outperform the Bi-rich samples (and $Tl_9Sb_{1-x}Te_6$) with 500 K zT values between 0.80 and 0.90 vs. 0.01 and 0.63.

To check for reproducibility, we repeated the physical property measurements for Tl_9BiTe_6 and Tl_9SbTe_6 on the same pellets as well as on different samples prepared in a different furnace, while slightly extending the temperature range of the measurements. Re-measuring the same samples did not result in any significant differences. The second Tl_9BiTe_6 sample showed that the figure-of-merit increases at least up to 540 K, and overall had *zT* values very comparable to the first sample (within error, e.g., *zT*(500 K) = 0.95 vs. 0.98). Likewise, the figure-of-merit of the second Tl_9SbTe_6 sample increased beyond 550 K, and the absolute values are equivalent to those of the first sample within error as well (Figure 4.6).

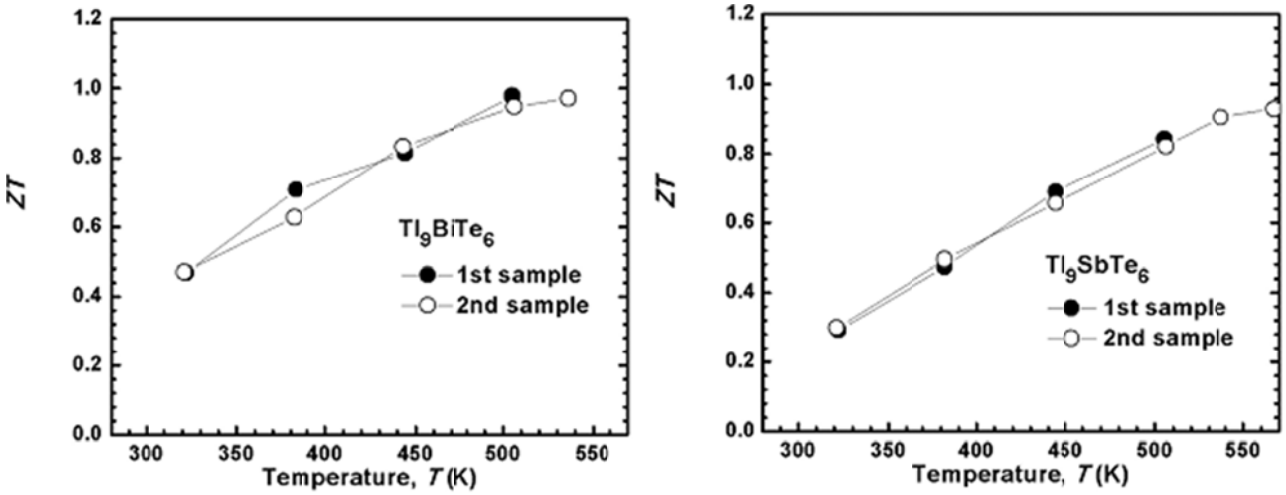

Figure 4.6 Figure-of-merit of two different Tl_9BiTe_6 and Tl_9SbTe_6 samples.

4.4. Conclusions

Motivated by promising reports on the thermoelectric properties of Tl_9BiTe_6, we have investigated four different series, namely $Tl_9Bi_{1-x}Te_6$, $Tl_{9-x}Bi_{1+x}Te_6$, $Tl_9Sb_{1-x}Te6$, and $Tl_{9-x}Sb_{1+x}Te_6$. All samples were prepared from the elements in evacuated silica tubes, and then hot-pressed to give dense pellets for measurements of the thermoelectric properties.

Table 4.4 summarizes the key data of the best Bi and Sb samples introduced here, as well as the literature data on Kurosaki's hot-pressed [61] and Wölfing's zone-refined Tl_9BiTe_6,[62] and cold-pressed, sintered Tl_9SbTe_6.[84] A substantial improvement of the thermoelectric figure-of-merit, zT, was achieved both in the Bi and Sb system over the previous data on hot-pressed Tl_9BiTe_6 and cold-pressed Tl_9SbTe_6, respectively. For example at 500 K, we report zT values of 1.1 for $Tl_9Bi_{0.98}Te_6$ (and 0.98 for Tl_9BiTe_6) and 0.90 for $Tl_{9.02}Sb_{0.98}Te_6$ (and 0.84 for Tl_9SbTe_6), compared to 0.78 for Tl_9BiTe_6 [61]and 0.34 for Tl_9SbTe_6.[84] Wölfing's zone-refined Tl_9BiTe_6 remains the best sample, having the lowest electrical conductivity and the highest Seebeck coefficient, with an extrapolated zT = 1.2 at 500 K.

Table 4.4 Thermoelectric properties of various Tl_9ETe_6 samples at 325 K (first value) and at 500 K (second value). a) Measured at 450 K. b) Extrapolated value.

Property	E = Sb sintered[84]	E = Bi hot pressed[61]	E = Bi zone refined[62]	E = Sb this work	E = Bi this work
$\alpha/(\mu V\ K^{-1})$	80 \ 106	163 \ 218	280 \ 399	115 \ 192	200 \ 285
$\sigma/(\Omega^{-1}cm^{-1})$	781 \ 396.8	193 \ 123	136 \ 60	490 \ 226	182 \ 83
$P.F./(\mu W\ cm^{-1}K^{-2})$	4.9 \ 5.9	–	–	6.5 \ 8.4	7.2 \ 6.7
$\kappa/(W\ m^{-1}K^{-1})$	0.88 \ 0.86	0.39 \ 0.39	0.46 \ 0.39[a)]	0.72 \ 0.50	0.50 \ 0.35
zT	0.2 \ 0.34	0.40 \ 0.78	0.72 \ 1.2	0.29 \ 0.84	0.47 \ 0.98
zT_{max} [T]	0.42 [591 K]	0.86 [590 K]	1.2 [500 K][b)]	0.93 [567K]	0.98 [500 K]

Considering the high electrical conductivity of the cold-pressed Tl_9SbTe_6 of 780 $\Omega^{-1}cm^{-1}$, compared to 490 $\Omega^{-1}cm^{-1}$ of the hot-pressed Tl_9SbTe_6, that particular sample seems to suffer more from

a too high charge carrier concentration than from the consolidation method, despite having the same nominal composition. We thus postulate that our samples have fewer defects and/or impurities. Further improvements appear to be possible by optimizing the materials on both the micro and the nano level, as demonstrated for PbTe.[86, 87] Moreover, different partial substitutions may enhance, or decrease, the performance, such as introducing lanthanides,[52, 53] or Sn atoms,[83] which remains to be investigated, as discussed in the following chapters.

5. Thermoelectric Properties of *Tt*-doped Tl_9BiTe_6 and Tl_9SbTe_6 (*Tt* = Sn, Pb)

5.1. Introduction

In the previous chapter, we revealed the results on the preparation and transport measurements (between 325 K and 500 K) of $Tl_9Bi_{1-x}Te_6$, $Tl_9Sb_{1-x}Te_6$ and their variants. Decreasing the Sb/Bi contents (cation vacancies) results in higher *p*-type carrier concentrations. High *zT* values of around unity were obtained for several samples. Apart from creating vacancies, alloying is also a common strategy for optimization of thermoelectric efficiency.[88, 89] For this contribution, we fabricated Sn- and Pb-doped Tl_9SbTe_6 and Tl_9BiTe_6. Considering that Sn and Pb have one valence electron less than Sb and Bi, the Sn and Pb substitutions are expected to induce extrinsic *p*-type carriers in the materials. Furthermore, the disorder of random atomic substitution may introduce mass and strain fluctuations in the material, which is expected to scatter the phonons, thereby decreasing the thermal conductivity.[90] With this in mind, we began to investigate the effects of the Sn- and Pb-content on crystal structure and thermoelectric properties of Tl_9SbTe_6 and Tl_9BiTe_6 variants.

5.2. Experimental Details

Several samples with the following nominal composition were investigated: $Tl_9Bi_{1-x}Sn_xTe_6$, $Tl_9Bi_{1-y}Pb_yTe_6$ ($0 \leq x, y \leq 0.15$), $Tl_9Sb_{1-m}Sn_mTe_6$ and $Tl_9Sb_{1-n}Pb_nTe_6$ ($0 \leq m, n \leq 0.10$). The compounds were synthesized from the respective elements (Tl granules, 99.9%, Strem Chemicals; Sb powder, 99.5%, – 100 mesh, Alfa Aesar; Bi granules, 99.997%, 1 - 2 mm, Alfa Aesar; Sn granules, 99.9%, Alfa

Aesar; Pb powder, 99.9%, Alfa Aesar; Te broken ingots, 99.99+%, Strem Chemicals). To remove impurities, Pb was further purified through the melting method, in which process the Pb powder was melted at 1003 K for 12 h, followed by cooling down to the room temperature with the furnace.

5.3. Results and Discussion

Figure 5.1 reveals the room temperature powder XRD patterns and crystallographic details of the samples are tabulated in Table 5.1.

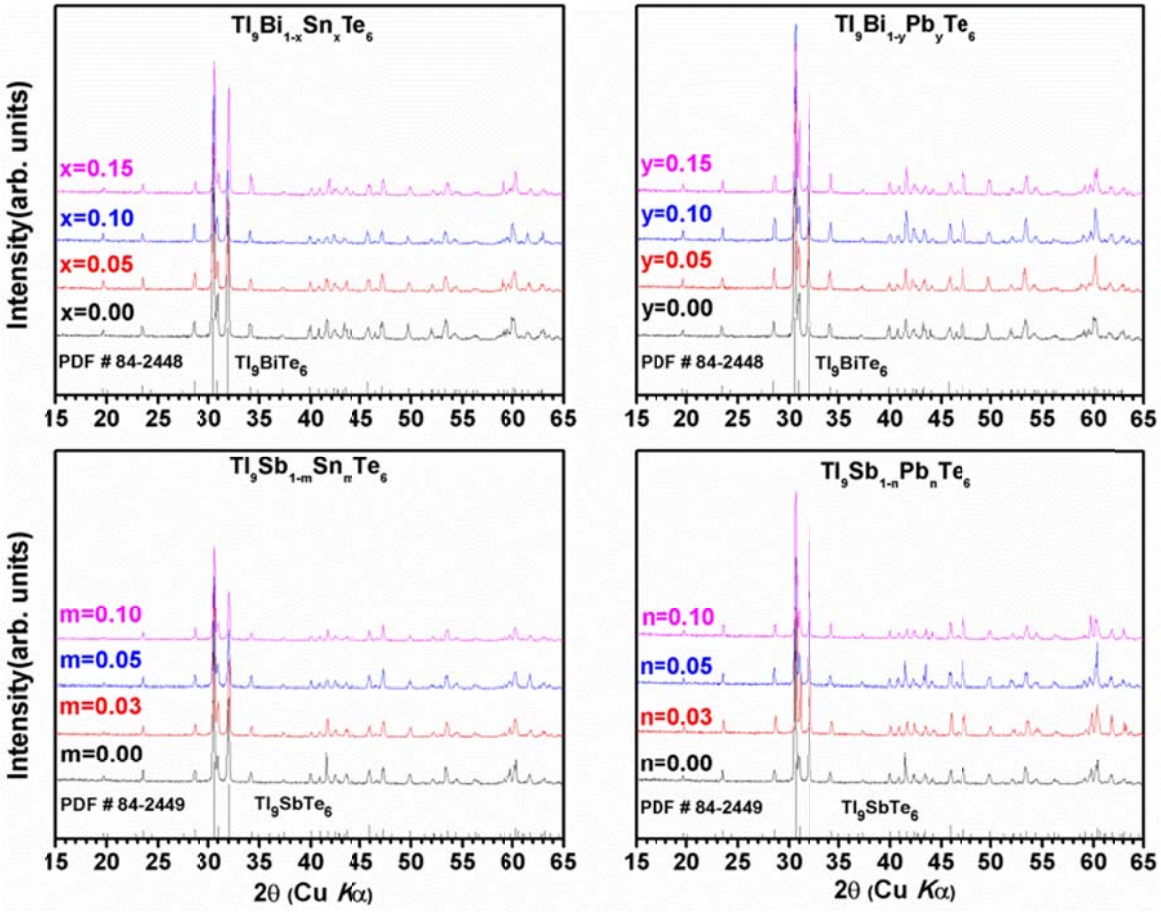

Figure 5.1 Room temperature powder XRD patterns of $Tl_9Bi_{1-x}Sn_xTe_6$, $Tl_9Bi_{1-y}Pb_yTe_6$ ($0 \le x, y \le 0.15$), $Tl_9Sb_{1-m}Sn_mTe_6$ and $Tl_9Sb_{1-n}Pb_nTe_6$ ($0 \le m, n \le 0.10$).

Table 5.1 Crystallographic information for *Tt*-doped Tl_9BiTe_6 and Tl_9SbTe_6 (*Tt* = Sn, Pb)

Chemical formula	Tl_9BiTe_6	$Tl_9Bi_{0.85}Pb_{0.15}Te_6$	$Tl_9Bi_{0.85}Sn_{0.15}Te_6$
M [g/mol]	2814.03	2813.76	2800.49
T [K]	296(2)	296(2)	296(2)
λ [Å]	1.5406	1.5406	1.5406
space group	*I*4/*mcm*	*I*4/*mcm*	*I*4/*mcm*
a [Å] = b	8.85533(7)	8.85391(7)	8.84966(8)
c [Å]	13.0482(2)	13.0308(2)	13.0173(2)
V [Å^3]	1023.20(1)	1021.51(1)	1019.47(1)
Z	2	2	2
R_P \ R_B	0.049 \ 0.099	0.050 \ 0.095	0.049 \ 0.118
Chemical formula	Tl_9SbTe_6	$Tl_9Sb_{0.90}Pb_{0.10}Te_6$	$Tl_9Sb_{0.90}Sn_{0.10}Te_6$
M [g/mol]	2759.74	2735.22	2726.38
T [K]	296(2)	296(2)	296(2)
λ [Å]	1.5406	1.5406	1.5406
space group	*I*4/*mcm*	*I*4/*mcm*	*I*4/*mcm*
a [Å] = b	8.82981(9)	8.84079(7)	8.83001(8)
c [Å]	13.0126(2)	13.0263(2)	13.0077(2)
V [Å^3]	1014.54(2)	1018.13(1)	1014.19(1)
Z	2	2	2
R_P \ R_B	0.056 \ 0.095	0.043 \ 0.085	0.0505 \ 0.079

The XRD patterns demonstrate that all the samples are single phase, having adopted the tetragonal Tl_5Te_3-type structure. No diffraction peak of any impurity was detected. The XRD peaks of the Sn and Pb doped Tl_9BiTe_6 and Tl_9SbTe_6 variants slightly deviated from standard XRD patterns of Tl_9BiTe_6 (PDF No. 84-2448) and Tl_9SbTe_6 (PDF No. 84-2449), which is caused by chemical substitutions, e.g. of Bi with Sn. Doping Tl_9BiTe_6 with Pb and Sn decreased the unit cell size, whereas doping Tl_9SbTe_6 with Pb increased the unit cell, as expected based on the different atomic radii. With each substitution of Sn and Pb on a Bi and Sb site, we expect to remove one valence electron, which should affect the transport properties.The temperature dependences of the electrical conductivity, σ, of all samples are plotted in Figure 5.2. In each case, σ decreases with increasing temperature, typical for degenerate semiconductors. An increasing doping level (i.e., increasing Sn and Pb amount) is expected to increase the number of holes, the dominant charge carriers according to earlier reports.[13,81] This expected trend is experimentally observed: with increasing x in $Tl_9Bi_{1-x}Sn_xTe_6$, the electrical conductivity at 300 K increased stepwise from $\sigma = 220\ \Omega^{-1}cm^{-1}$ when $x = 0$ to $520\ \Omega^{-1}cm^{-1}$ when $x = 0.15$. It is worth noting that at the same doping level, the Pb doped samples have a higher electrical conductivity than the Sn doped ones. For example, $\sigma = 910\ \Omega^{-1}cm^{-1}$ when $y = 0.15$ is much higher than the $520\ \Omega^{-1}cm^{-1}$ when $x = 0.15$. With an estimated relative error of ±5%, these differences are significant. Moreover, the temperature dependence of the Pb-containing samples is larger than that of the Sn samples, reminiscent of the differences of $Tl_{10-x}Pb_xTe_6$ and $Tl_{10-x}Sn_xTe_6$.[91] The same general trends were also observed in the Pb doped Tl_9SbTe_6 samples, while for Sn-doping, σ only increased for the highest dopant concentration, $m = 0.10$. With hole doping, smaller increases in σ were obtained: considering that for each hole replacing one trivalent Bi atom, three electrons are missing; thus $Tl_9Bi_{0.95}Te_6$ ($\sigma = 3730\ \Omega^{-1}cm^{-1}$)[81] has the same formal electron count as $Tl_9Bi_{0.85}Sn_{0.15}Te_6$.

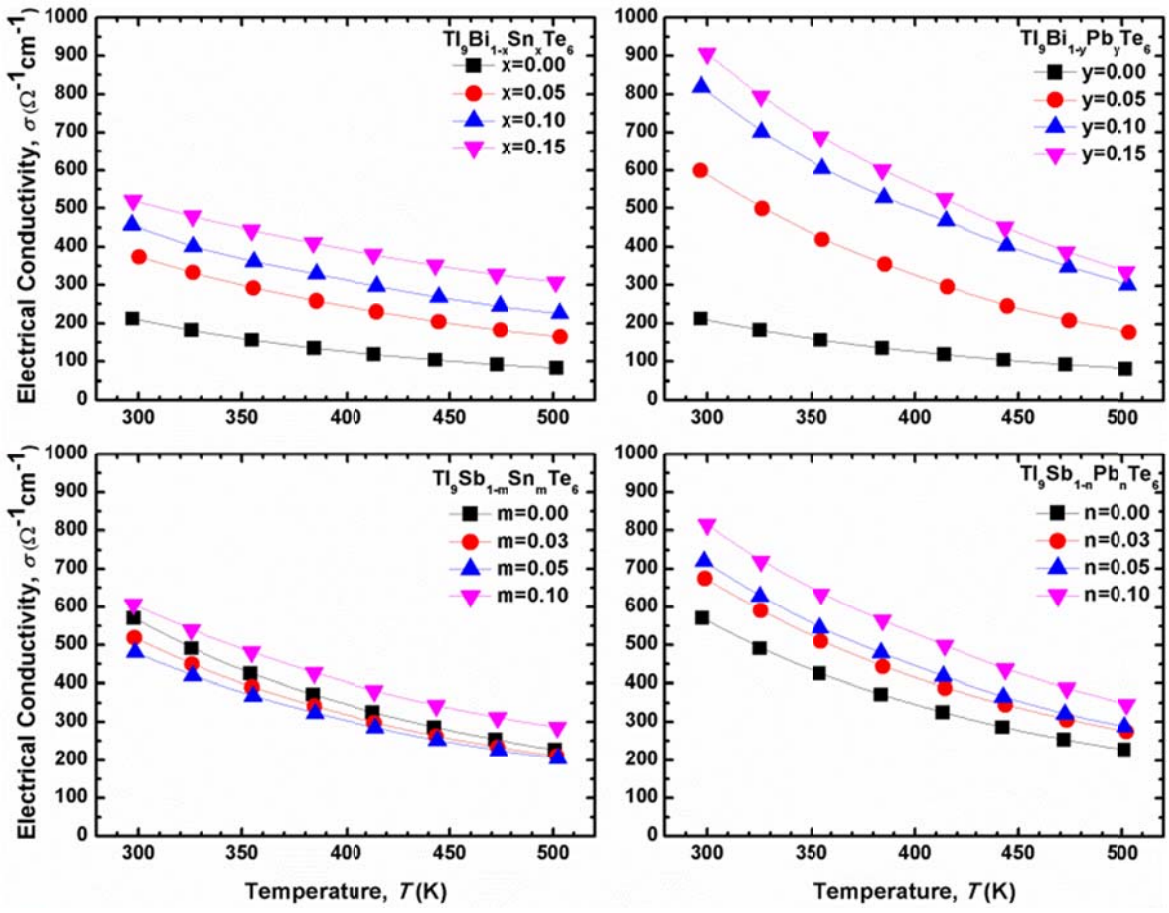

Figure 5.2 Electrical conductivity of $Tl_9Bi_{1-x}Sn_xTe_6$, $Tl_9Bi_{1-y}Pb_yTe_6$ ($0 \leq x, y \leq 0.15$), $Tl_9Sb_{1-m}Sn_mTe_6$ and $Tl_9Sb_{1-n}Pb_nTe_6$ ($0 \leq m, n \leq 0.10$) as a function of temperature.

The temperature dependences of the Seebeck coefficient, α, of all samples are shown in Figure 5.3. In each case, α displays behaviour typical of *p*-type semiconductors, increasing linearly in the entire temperature range of the measurements, suggesting that the carrier concentration is constant.[92] All Seebeck coefficient values are positive, implying that the major carriers in the samples are holes. In the cases discussed here as well, the samples that exhibit the highest conductivity possess the smallest Seebeck coefficient. At room temperature, the Seebeck coefficient values range from α = +180 μV K^{-1} for Tl_9BiTe_6 to +100 μV K^{-1} for $Tl_9Bi_{0.85}Sn_{0.15}Te_6$, and +70 μV K^{-1} for $Tl_9Bi_{0.85}Pb_{0.15}Te_6$. Direct hole-

doping causes a smaller decrease in α, e.g. to +140 μV K^{-1} for $Tl_9Bi_{0.95}Te_6$. With an experimental error of ±3%, these values differ significantly. The changes in the magnitude of the Seebeck coefficient are less distinct in the cases of the doped variants of Tl_9SbTe_6; in case of Sn-doping, only the m = 0.10 sample exhibits significantly different (lower) α values.

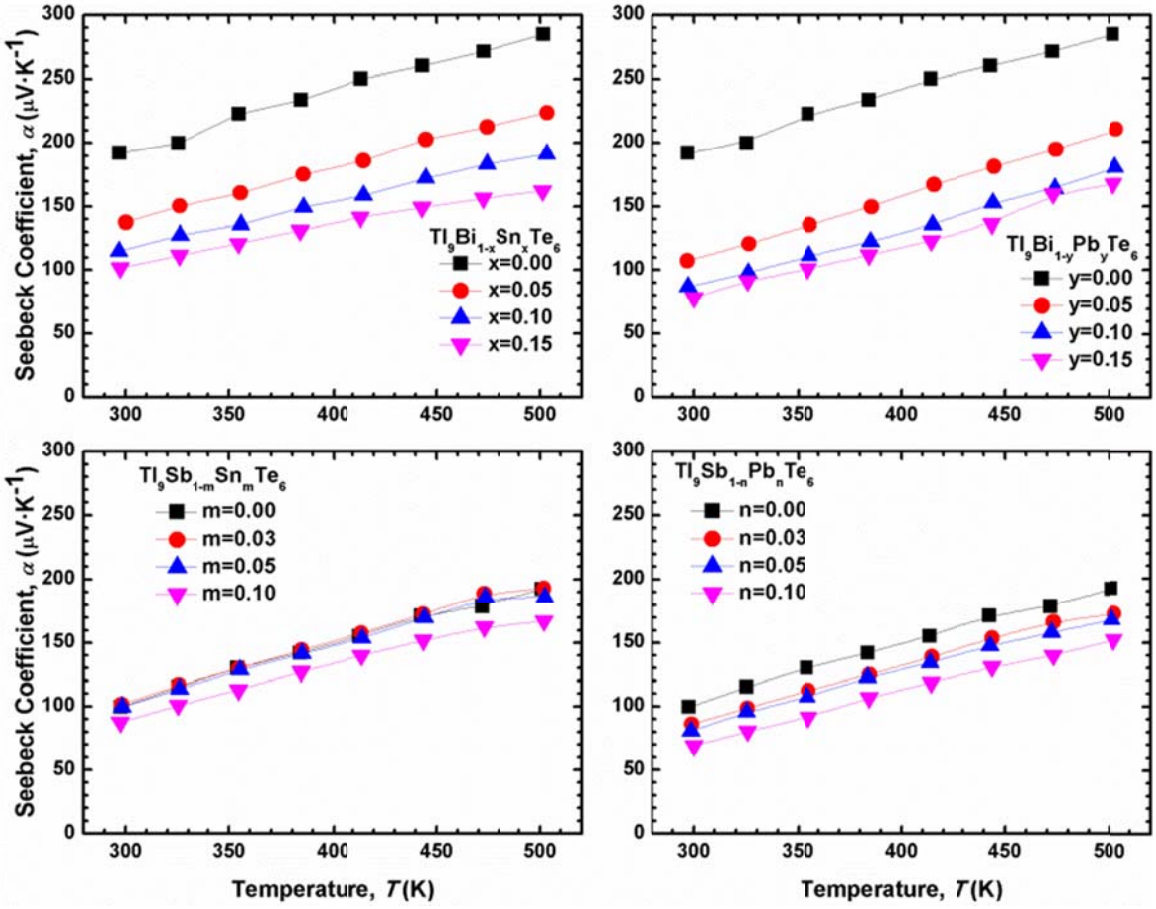

Figure 5.3 Seebeck coefficient of $Tl_9Bi_{1-x}Sn_xTe_6$, $Tl_9Bi_{1-y}Pb_yTe_6$ ($0 \leq x, y \leq 0.15$), $Tl_9Sb_{1-m}Sn_mTe_6$ and $Tl_9Sb_{1-n}Pb_nTe_6$ ($0 \leq m, n \leq 0.10$) as a function of temperature.

The power factor, $P.F. = \alpha^2\sigma$, for these compounds is displayed in Figure 5.4. The Seebeck coefficient, α, dominates this equation, and thus the temperature dependence. As expected, all $P.F.$

values rise in a similar fashion to α with the exception of undoped Tl_9BiTe_6, which shows weak negative temperature dependence. For the Tl_9BiTe_6-based compounds, the doped samples exhibit lower power factors compared with the mother compound when the temperature is below 370 K. However, at higher temperatures, the electrical performance of the doped samples exceeds that of the pristine Tl_9BiTe_6, culminating in a power factor of *P.F.* = 8.4 μW $cm^{-1}K^{-2}$ for $Tl_9Bi_{0.85}Sn_{0.15}Te_6$ and 9.8 μW $cm^{-1}K^{-2}$ for $Tl_9Bi_{0.90}Pb_{0.10}Te_6$, compared to 6.9 μW $cm^{-1}K^{-2}$ for Tl_9BiTe_6 (all at 500 K). The 9.8 μW $cm^{-1}K^{-2}$ constitute the highest power factor we have experienced in Tl_5Te_3-based materials to date, matching the extrapolated one of zone-refined Tl_9BiTe_6 at 500 K (9.8 μW $cm^{-1}K^{-2}$).[62] In comparison, all the doped Sb samples display slightly lower power factor in the whole temperature range. The *P.F.* values of the Tl_9SbTe_6 series increase as the temperature increases, and then almost level off (around 8 μW $cm^{-1}K^{-2}$) in the temperature range of 400 K – 500 K or even decrease at the end of this range, for example in case of Sn-doped samples.

The thermal conductivity data obtained from the laser flash method are depicted in Figure 5.5. All samples show an overall low thermal conductivity (κ < 1.0 W $m^{-1}K^{-1}$), which slowly decreases with increasing temperature. Generally speaking, as a consequence of the significant changes in charge carrier concentration, the samples with higher Sn and Pb content (having larger electrical conductivity, σ) exhibit higher thermal conductivity. At 325 K, κ increases from 0.48 W $m^{-1}K^{-1}$ when x = 0.00 to 0.75 W $m^{-1}K^{-1}$ when x = 0.15. With the experimental error assumed to be ±5%, one should also note that the Pb-doped samples usually show higher total thermal conductivity values compared with their Sn-doped counterparts in both Tl_9BiTe_6 and Tl_9SbTe_6 series, which correlates well with their high electrical conductivity values.

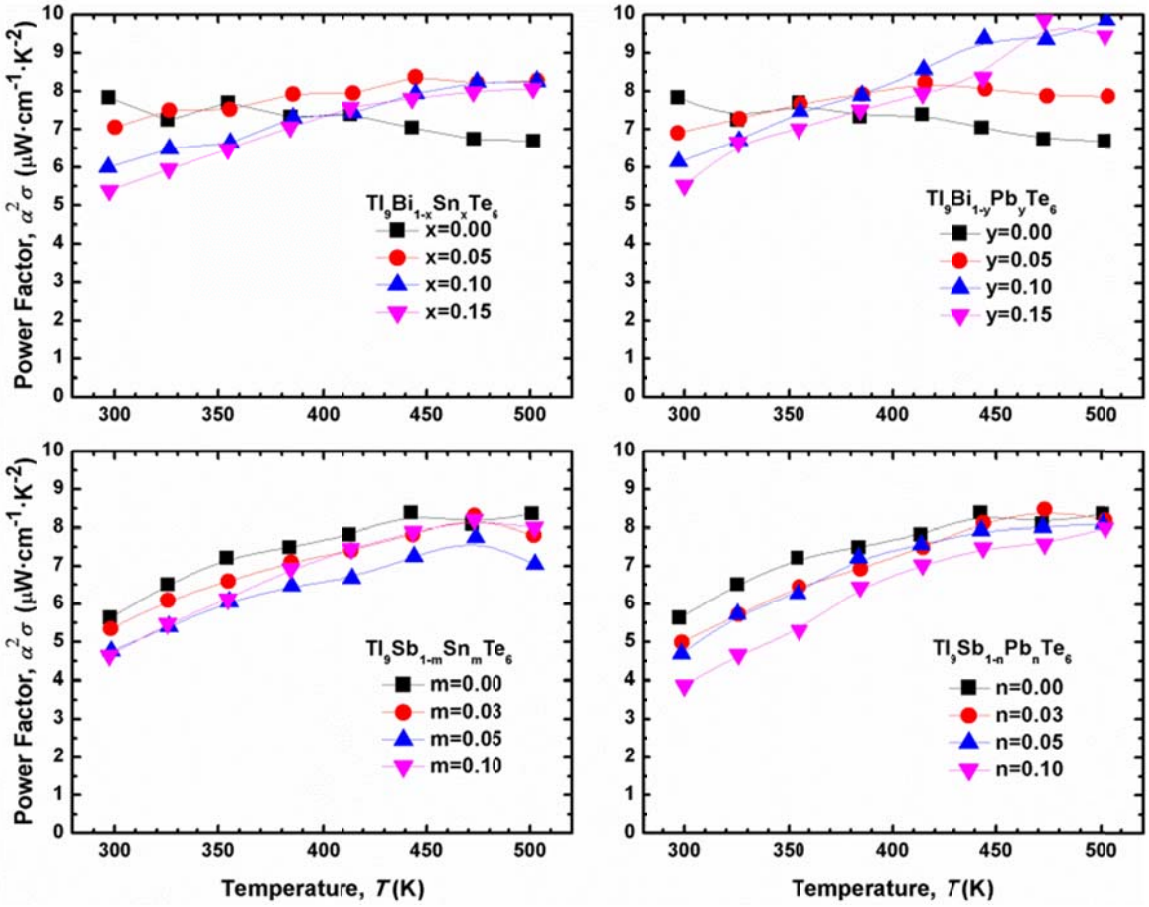

Figure 5.4 Power factor of $Tl_9Bi_{1-x}Sn_xTe_6$, $Tl_9Bi_{1-y}Pb_yTe_6$ ($0 \le x, y \le 0.15$), $Tl_9Sb_{1-m}Sn_mTe_6$ and $Tl_9Sb_{1-n}Pb_nTe_6$ ($0 \le m, n \le 0.10$) as a function of temperature.

To obtain insight into the effect of Sn and Pb doping on the lattice thermal conductivity, we calculate the lattice contribution, κ_L, to the thermal conductivity. A comparison with theoretical values of the minimum lattice thermal conductivity for Tl_9BiTe_6 and Tl_9SbTe_6, κ_{min}, is instructive. Here the calculated longitudinal and transverse sound velocities for Tl_9BiTe_6 and Tl_9SbTe_6 from reference are employed.[51] All samples exhibit very low κ_L values, consistently below 0.5 W m^{-1}K^{-1}, which approach κ_{min} in some cases (Figure 5.6), in accord with earlier findings of undoped Tl_9BiTe_6[13] and Tl_9SbTe_6.[17] The changes in κ_L after incorporation of Sn or Pb are not systematic (often but not always leading to a

lower κ_L). Because κ_L was calculated as the difference of two similar, experimentally determined values via $\kappa_L = \kappa - \kappa_E$, its relative error is higher than for both κ and κ_E, which may explain the absence of a clear trend.In most thermoelectric materials, the lattice thermal conductivity decreases with increasing temperature, suggesting an enhancement in phonon-phonon scattering with rising temperature. Most of these calculated curves are very flat, and in some samples, e.g. $Tl_9Bi_{0.95}Pb_{0.05}Te_6$, the lattice thermal conductivity seems to be even temperature independent, especially in the temperature range 375 K - 500 K.

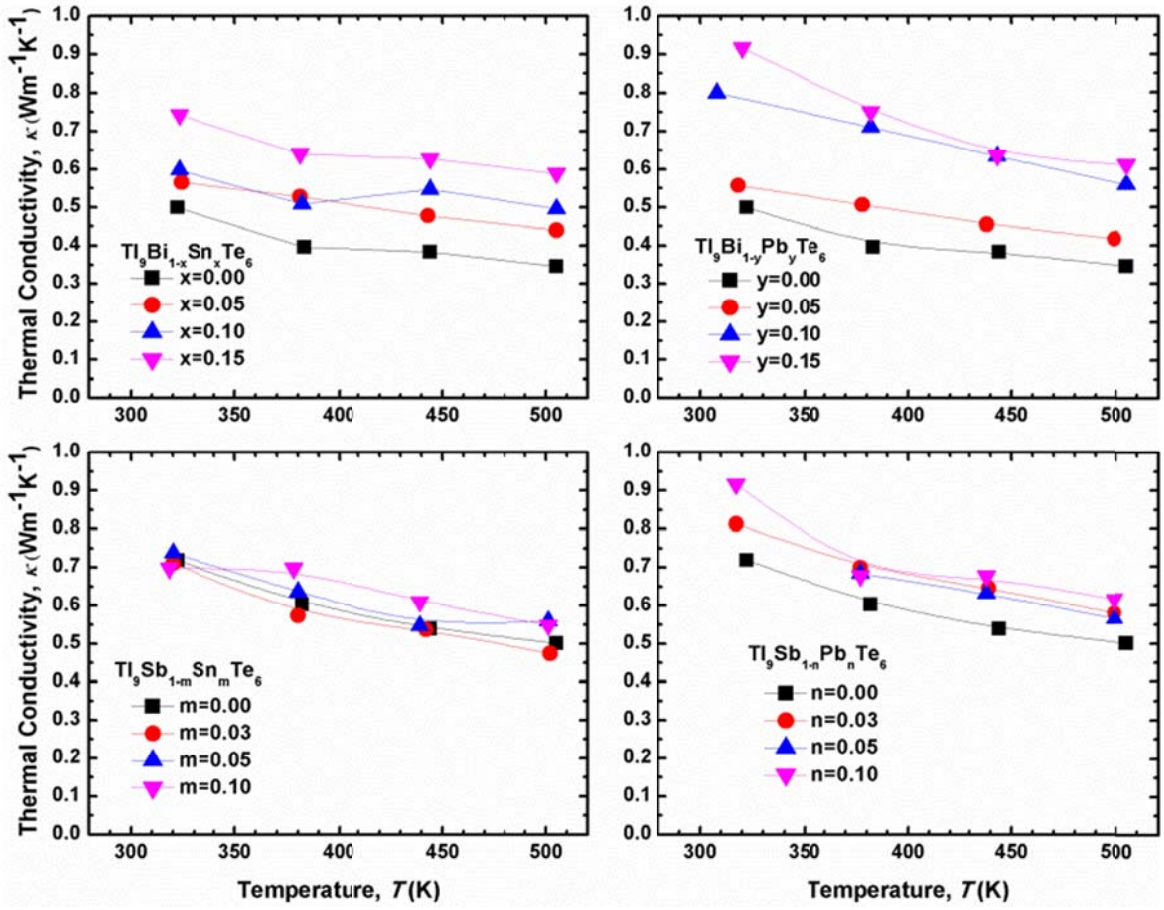

Figure 5.5 Thermal conductivity of $Tl_9Bi_{1-x}Sn_xTe_6$, $Tl_9Bi_{1-y}Pb_yTe_6$ ($0 \le x, y \le 0.15$), $Tl_9Sb_{1-m}Sn_mTe_6$ and $Tl_9Sb_{1-n}Pb_nTe_6$ ($0 \le m, n \le 0.10$) as a function of temperature.

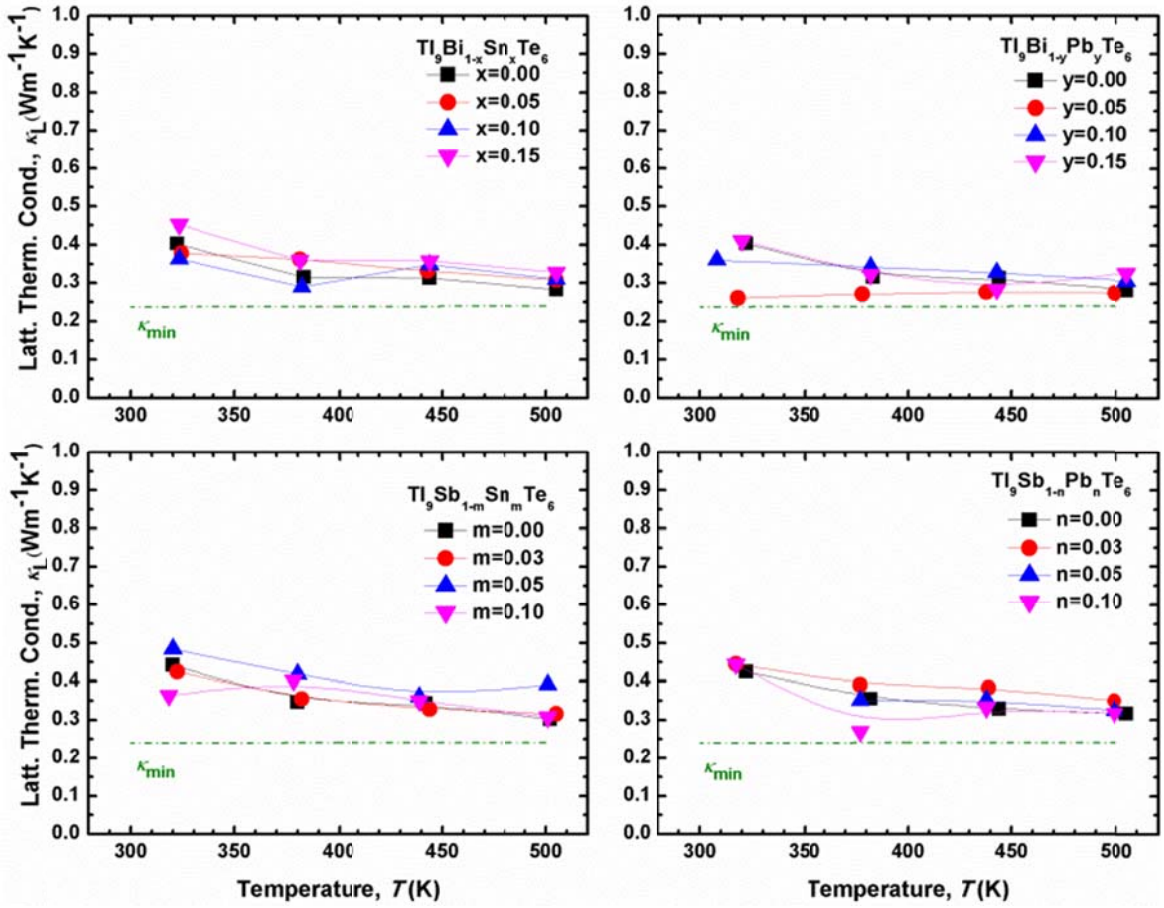

Figure 5.6 Lattice thermal conductivity of $Tl_9Bi_{1-x}Sn_xTe_6$, $Tl_9Bi_{1-y}Pb_yTe_6$ ($0 \leq x, y \leq 0.15$), $Tl_9Sb_{1-m}Sn_mTe_6$ and $Tl_9Sb_{1-n}Pb_nTe_6$ ($0 \leq m, n \leq 0.10$) as a function of temperature.

As no increase in κ_L at higher temperatures occurs, no bipolar diffusion contribution is found, implying higher zT values could be achieved if the samples were measured at higher temperatures. The dimensionless thermoelectric figure-of-merit zT is calculated based on the transport data presented above. For all samples, zT increases monotonically with increasing temperature (Figure 5.7). The zT values of the slightly doped samples ($x = 0.05$, $y = 0.05$, $m = 0.03$) are within estimated experimental error (±8%) of those of the undoped ones, with the exception of sample $n = 0.03$. With increasing amount of the dopants, the zT values deteriorate significantly: at around 500 K, $Tl_9Bi_{0.85}Sn_{0.15}Te_6$ and $Tl_9Bi_{0.85}Pb_{0.15}Te_6$

possess zT values of 0.69 and 0.78, which are 30% and 20% lower than zT = 0.98 of Tl_9BiTe_6, respectively.

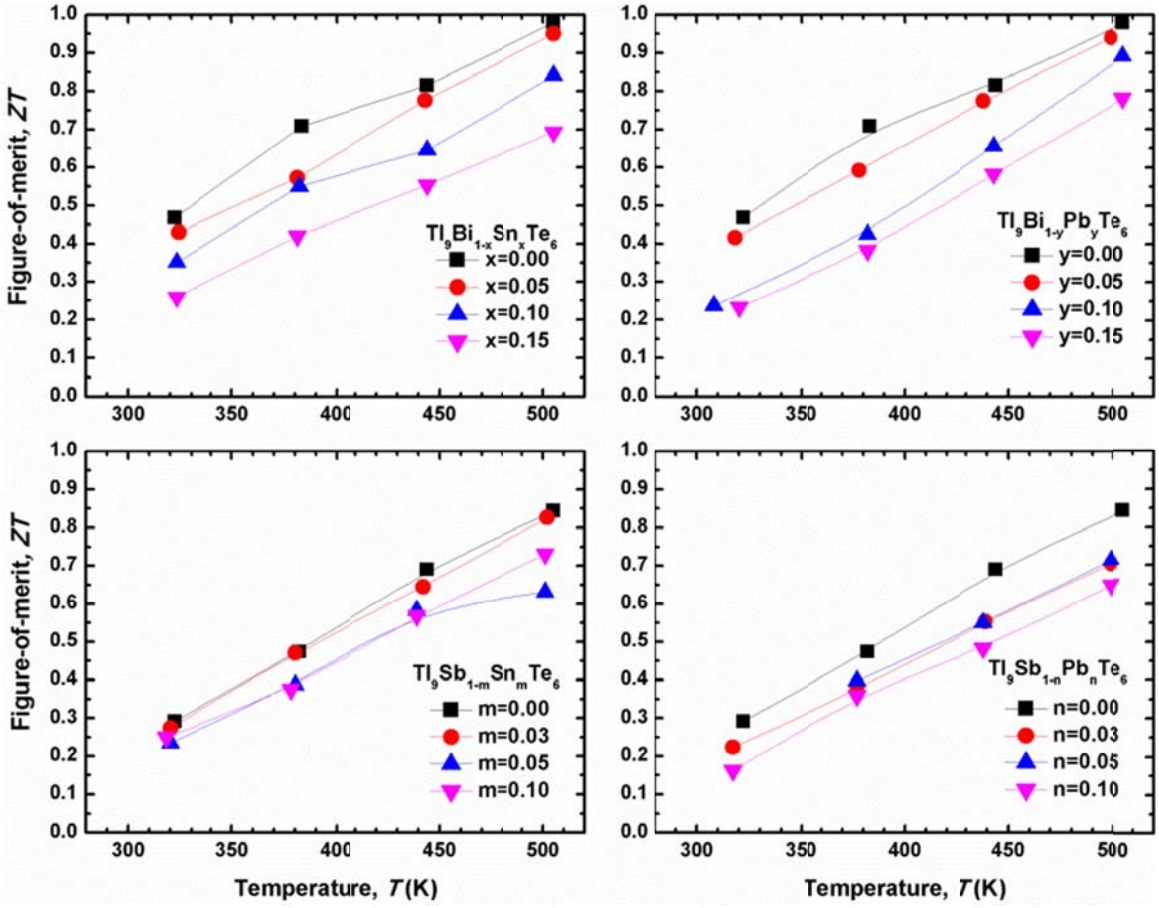

Figure 5.7 Thermoelectric figure-of-merit zT of $Tl_9Bi_{1-x}Sn_xTe_6$, $Tl_9Bi_{1-y}Pb_yTe_6$ ($0 \le x, y \le 0.15$), $Tl_9Sb_{1-m}Sn_mTe_6$ and $Tl_9Sb_{1-n}Pb_nTe_6$ ($0 \le m, n \le 0.10$) as a function of temperature.

5.4. Conclusions

Polycrystalline bulk materials with the compositions $Tl_9Bi_{1-x}Sn_xTe_6$, $Tl_9Bi_{1-y}Pb_yTe_6$ ($0 \le x, y \le 0.15$) and $Tl_9Sb_{1-m}Sn_mTe_6$ and $Tl_9Sb_{1-n}Pb_nTe_6$ ($0 \le m, n \le 0.10$) have been prepared by the combination

of the melting method and the hot-pressing technique. XRD results indicate that all the samples crystallize in the Tl_5Te_3-type structure, with Bi and Sb occupying the 4*c* site of the space group *I*4/*mcm*. The substitution of Sn and Pb atoms for Bi and Sb are considered to be *p*-type doping from the viewpoint of valence band filling, which is reflected in the results of the thermoelectric property measurements: increasing the Sn or Pb content results in an increase in the hole carrier concentration, and thus a decrease in Seebeck coefficient and an increase in both electrical and thermal conductivity. The highest power factor values were found for the slightly doped Bi samples. No clear conclusion regarding the composition dependence of the lattice thermal conductivity could be drawn from the results presented, probably due to the relatively small contents of the dopants in combination with experimental errors. In the end, the best thermoelectric properties still belong to the cases of pristine Tl_9BiTe_6 and Tl_9SbTe_6. As such, it would be interesting to see whether Sn and Pb could be used to substitute for Tl, e.g. according to $Tl_{9-x}BiPb_xTe_6$, in order to decrease the carrier concentration (number of holes) because increasing it ultimately led to decreasing thermoelectric performance. Of course, the toxicity of thallium remains a concern, as well as the toxicity of lead, antimony and tellurium to a smaller extent. We will therefore attempt to replace thallium gradually with less toxic elements such as indium.

6. Thermoelectric Properties of $Tl_{10-x}Sn_xTe_6$ and $Tl_{10-x}Pb_xTe_6$

6.1. Introduction

Tl_9BiTe_6's isostructural counterparts $Tl_4ETe_3 \equiv Tl_8E_2Te_6$ with E = Sn and Pb instead of Bi, were reported to attain significantly smaller zT values, reaching approximately $zT_{max} = 0.7$ at 673 K.[63] Here we describe how we were able to approximately double zT_{max} via optimization of the Tl : E ratio and the densification procedure, culminating in $zT \approx 1.5$ in case of $Tl_{8.10}Pb_{1.90}Te_6$ and $zT \approx 1.3$ in case of $Tl_{8.05}Sn_{1.95}Te_6$, both around moderate 685 K.

6.2. Experimental Section

The following samples were investigated: $Tl_{10-x}Sn_xTe_6$ with $1.95 \leq x \leq 2.05$ and $Tl_{10-x}Pb_xTe_6$ with $1.90 \leq x \leq 2.05$. The reactions started from the respective elements (Tl granules, 99.9%, Strem Chemicals; Sn shot, 99.99+%, 3 mm, Alfa Aesar; Pb powder, 99.9%, Alfa Aesar; Te broken ingots, 99.99+%, Strem Chemicals). The tubes were heated to 923 K within twelve hours, i.e. beyond the melting points between 830 K and 850 K, held at this temperature for 24 hrs, and then cooled down within 120 hours to 703 K. All samples were hot-pressed under a flow of argon at 45 MPa at 523 K for a period of 2 h.

To further verify the crystal structure, a single crystal of the Tl_4PbTe_3 sample was selected for structure studies. A Bruker Kappa APEX II utilizing Mo Kα radiation was employed for the data collection at room temperature. Data were collected by scans of 0.3° in ω and ϕ in nine blocks for a total

of 3928 frames, with exposure times of 20 seconds per frame. After correcting for Lorentz and polarization effects, the structure refinements were performed with the SHELXTL package.[68] The refinements starting from the Tl_5Te_3 structure, with Pb on the 4*c* site, converged quickly without any noticeable problems, resulting in the residual values of $R_1 = 0.019$ and $wR_2 = 0.046$ (all reflections).

Two hot-pressed pellets of the starting compostions $Tl_{8.05}Sn_{1.95}Te_6$ and $Tl_{8.10}Pb_{1.90}Te_6$ were analyzed after the physical property measurements by EDX. No impurity elements were found, and the pellets appeared to be homogenous with the elements close to the desired ratios.

The WIEN2k package, which employs the full-potential linearized augmented plane wave (FP-LAPW) method within density functional theory (DFT),[54, 55] was utilized for calculations on Tl_5Te_3, Tl_4SnTe_3 and Tl_4PbTe_3. The generalized gradient approximation (GGA) from Perdew, Burke and Ernzerhof was used for exchange and correlation energies.[93] We chose 2.5 Bohr as muffin-tin radii (R_{MT}) for all atoms, and set the product $R_{MT} \times K_{max} = 7$. For the self-consistent energy calculations, 240 independent *k* points were selected on a grid of 14 × 14 × 14 with an improved tetrahedron method within the irreproducible wedge of the first Brillouin zone. The energy convergence was set to be 10^{-4} Ry for the self-consistency. In addition, the modified Becke-Johnson local density functional was also employed to obtain more accurate band gaps.[94, 95]

6.3. Results and Discussion

6.3.1. Crystal Structures

No additional peaks were detected in the powder patterns of any of the samples discussed here, except for very minor ones in the cases of $Tl_{7.95}Sn_{2.05}Te_6$ (barely visible) and $Tl_{7.95}Pb_{2.05}Te_6$, indicative of the formation of SnTe and PbTe, respectively. The XRD patterns are shown in the Figure 6.1.

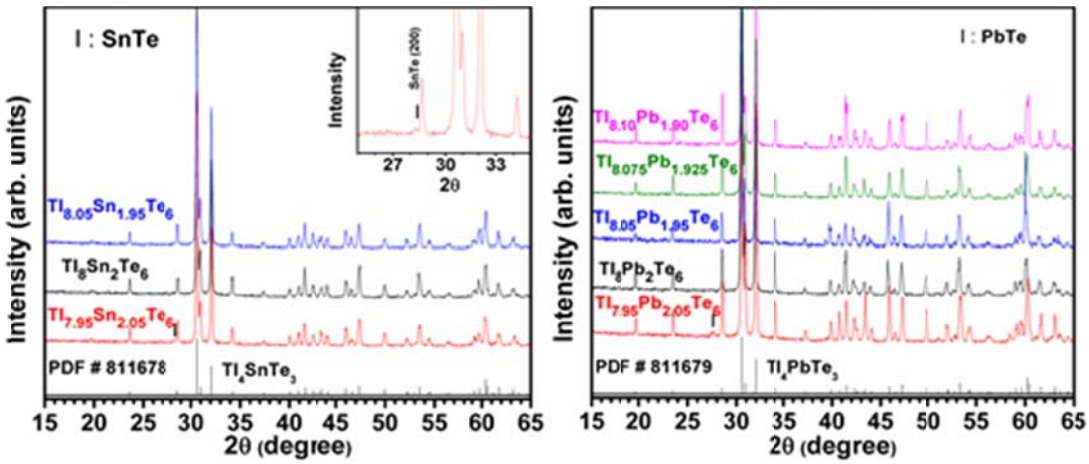

Figure 6.1 XRD patterns of $Tl_{10-x}Sn_xTe_6$ (left) and $Tl_{10-x}Pb_xTe_6$ (right).

The refined lattice parameters are listed in Tables 6.1 and 6.2, in comparison to Tl_5Te_3[50] and Tl_4SnTe_3 and Tl_4PbTe_3.[59] Going from Tl_5Te_3 to Tl_4SnTe_3 or Tl_4PbTe_3, the *a* parameter decreases, while *c* and the volume of the cell increase. This anisotropic change is a consequence of the more regular coordination of Sn and Pb by Te, compared to Tl1 in Tl_5Te_3. The same tendencies are observed with increasing Sn and Pb content for the $Tl_{10-x}Sn_xTe_6$ and $Tl_{10-x}Pb_xTe_6$ series, respectively. Finally, the Pb compounds generally have larger unit cell dimensions than the Sn compounds because of the larger size of the Pb atom.

To verify that these materials do adopt the In_5Bi_3 type, a single crystal structure study was performed on Tl_4PbTe_3. Details are summarized in Table 6.3. Further details of the crystal structure investigation may be obtained from the Fachinformationszentrum Karlsruhe, 76344 Eggenstein-Leopoldshafen (Germany), on quoting the depository number CSD-427382. This study confirmed that Tl_4PbTe_3 indeed crystallizes in the assumed structure type, and that the Tl2 atom exhibits larger atomic displacement parameters, compared to the Pb1 and the Te sites, namely U_{eq} = 0.031 Å^2 vs. 0.016 Å^2 -

0.022 Å^2 (Table 6.4). The latter may contribute to low thermal conductivity, as shown for various clathrates.[96] Similarly, the respective values obtained by Böttcher et al. were U_{eq} = 0.024 Å^2 for Tl2 vs. 0.010 Å^2 - 0.015 Å^2 for the other sites. Such differences were observed in other examples of this structure as well, namely in Tl_4SnTe_3 (U_{eq}(Sn1) = 0.014 Å^2, U_{eq}(Tl2) = 0.024 Å^2) and in $Tl_{9.4}La_{0.6}Te_6$ (U_{eq}(Tl1/La1) = 0.028 Å^2, U_{eq}(Tl2) = 0.037 Å^2) with mixed Tl and La occupancies on the 4*c* site.[52]

Table 6.1 Lattice parameters of $Tl_{10-x}Sn_xTe_6$ in comparison to Tl_5Te_3 and Tl_4SnTe_3 reported by Böttcher et al.*.

Parameter	Tl_5Te_3*	x = 1.95	x = 2.0	x = 2.05	Tl_4SnTe_3*
a [Å]	8.9320(2)	8.8315(3)	8.832(1)	8.8380(3)	8.819(2)
c [Å]	12.589(4)	13.0385(5)	13.054(2)	13.0550(5)	13.013(3)
V [Å^3]	1003.9(5)	1016.9(1)	1018.3(5)	1019.73(9)	1012.1(4)

Table 6.2 Lattice parameters of $Tl_{10-x}Pb_xTe_6$ in comparison to Tl_5Te_3 and Tl_4PbTe_3 reported by Böttcher et al.*.

Parameter	Tl_5Te_3*	x = 1.9	x = 1.95	x = 2.0	Tl_4PbTe_3*
a [Å]	8.9320(2)	8.8582(3)	8.85705(6)	8.8566(3)	8.841(2)
c [Å]	12.589(4)	13.0718(6)	13.08541(2)	13.0880(4)	13.056(3)
V [Å^3]	1003.9(5)	1025.7(1)	1026.42(2)	1026.62(9)	1020.4(4)

Table 6.3 Crystallographic details of Tl_4PbTe_3.

Formula weight [g/mol]	1407.47
T of measurement [K]	295(2)
λ [Å]	0.71073
space group	*I*4/*mcm*
a [Å]	8.8449(3)
c [Å]	13.0729(6)
V [Å^3]	1022.72(7)
Z	4
μ [mm^{-1}]	87.5
ρ_{calcd} [g/cm^3]	9.14
$R(F_o)^{a)}$ \ $wR\ (F_o^2)^{b)}$ (all data)	0.019 \ 0.046

a) $R(F_o) = \Sigma||F_o|-|F_c|| \ / \ \Sigma|F_o|$; b) $wR\ (F_o^2) = [\ \Sigma[w(F_o^2 - F_c^2)^2] \ / \ \Sigma[w(F_o^2)^2]\ ]^{1/2}$

Table 6.4 Atomic positions and atomic displacement parameters of Tl_4PbTe_3.

Atom	site	x	y	z	U_{eq}/Å^2
Pb1	4*c*	0	0	0	0.0221(2)
Tl2	16*l*	0.14661(3)	x + ½	0.15933(3)	0.0307(2)
Te1	4*a*	0	0	¼	0.0181(2)
Te2	8*h*	0.33700(5)	x + ½	0	0.0158(2)

The large atomic displacement parameters may be a consequence of the highly irregular coordination of Tl2 by five Te atoms at distances between 3.16 Å and 3.59 Å (Table 6.5). Böttcher et al. found basically equivalent Tl2–Te distances between 3.17 Å and 3.59 Å.[59] The Te coordination of the Pb1 atom is much more regular, showing six Te atoms at Pb–Te distances of 3.27 Å and 3.31 Å (Böttcher: 3.26 Å, 3.31 Å). That Tl adopts less regular coordination spheres than Pb, was also observed in the quaternary Tl-Pb chalcogenides $Tl_{18}Pb_2M_7Q_{25}$ (M = Ti, Zr, Hf; Q = S, Se)[38] and Tl_2PbMQ_4 (M = Zr, Hf; Q = S, Se).[39]

Table 6.5 Selected interatomic distances [Å] of Tl_4PbTe_3 in comparison to Böttcher's report.

Distance	No.	*this work*	Böttcher's
Pb1–Te1	2×	3.2682(2)	3.264(1)
Pb1–Te2	4×	3.3111(2)	3.313(2)
Tl2–Te2	1×	3.1639(6)	3.174(6)
Tl2–Te2	2×	3.4437(5)	3.432(4)
Tl2–Te1	2×	3.5856(3)	3.586(2)
Tl2–Tl2	1×	3.5085(8)	3.503(2)
Tl2–Tl2	2×	3.5138(6)	3.515(5)
Tl2–Tl2	1×	3.6678(7)	3.653(7)

For more structural details, it is referred to earlier work on Tl_4ETe_3[59] and Tl_9LaTe_6, where the consequences of Tl : La mixing on the 4*c* site are discussed.[52] In case of the latter, a significant phase range was detected for $Tl_{10-x}Ln_xTe_6$, with $0.2 \leq x \leq 1.32$, and several different lanthanides, Ln, were used.[53]

6.3.2. Electronic Structures

Electronic structure calculations for Tl_5Te_3 and Tl_4SnTe_3 were first presented by Miller et al., who utilized the Extended Hückel approximation in 1996.[97] This resulted in Tl_5Te_3 being a metal and Tl_4SnTe_3 a narrow gap semiconductor with a gap of 0.7 eV. We obtained qualitatively equivalent results using the DFT-based LMTO method (E_{gap} = 0.3 eV), and showed that the intermediate Tl_9SnTe_6 should be a *p*-type extrinsic semiconductor. In Figure 6.2, the density of states of Tl_5Te_3, Tl_4SnTe_3 and Tl_4PbTe_3 are presented, calculated with a full potential DFT method. Again, this yields metallic properties for Tl_5Te_3, and the PBE approach results in touching of the valence and conduction bands for Tl_4SnTe_3 and Tl_4PbTe_3, while mBJ yields (more trustworthy) gaps of 0.2 eV and 0.3 eV, respectively. Noteworthy for the latter two DOS are the rather steep slope just below the Fermi level, E_F, indicative of large Seebeck coefficient values when *p*-doped. This *p*-doping may be conveniently achieved via decreasing the *E* = Sn, Pb amount, as both *E* atoms have one more valence electron than Tl.

6.3.3. Thermoelectric Properties

We determined the properties of the series $Tl_{10-x}Sn_xTe_6$ with $1.95 \leq x \leq 2.05$ and $Tl_{10-x}Pb_xTe_6$ with $1.90 \leq x \leq 2.05$. In both cases, the samples with $x = 2.05$, i.e. the most *E*-rich samples, contained small amounts of the binary telluride *E*Te. Thus, the actual *E* amount in the target compound is most

likely smaller than as expressed in the target formula $Tl_{7.95}E_{2.05}Te_6$. One could assume that the phase width of $Tl_{10-x}E_xTe6$ series is below $x = 2.05$ (while x can be as small as zero). The data are summarized in Tables 6.6 and 6.7 in comparison to the literature data.

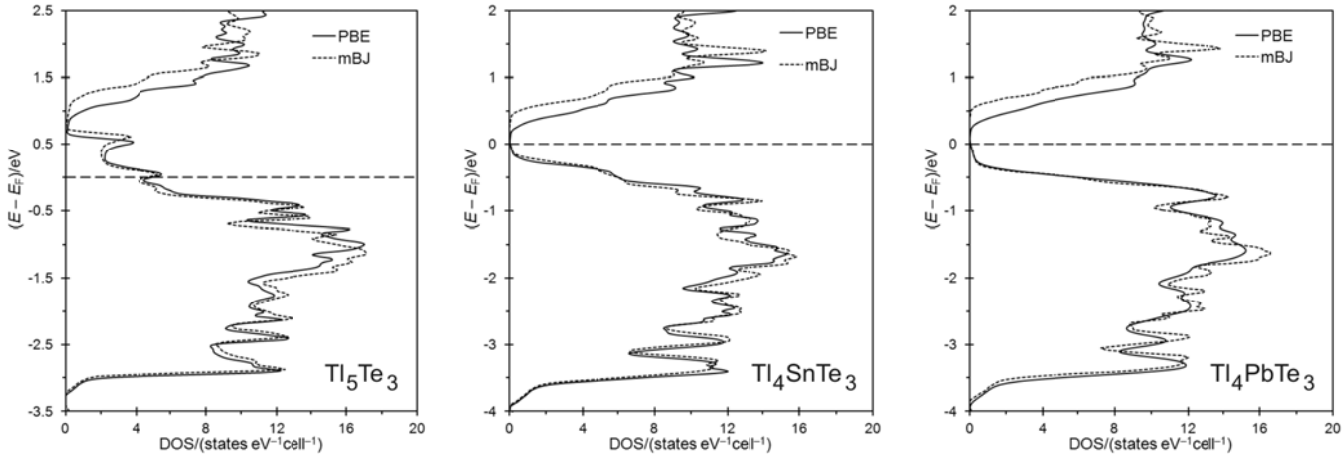

Figure 6.2 Density of states of Tl_5Te_3 (left), Tl_4SnTe_3 (center), and Tl_4PbTe_3 (right).

Table 6.6 Thermoelectric properties of $Tl_{10-x}Sn_xTe_6$ at ≈320 K (first value) and at ≈ 685 K (second value) in comparison to Tl_4SnTe_3 reported by Kosuga et al.*.

Property	$x = 1.95$	$x = 2$	$x = 2.05$	Tl_4SnTe_3*
σ/(Ω^{-1}cm^{-1})	549 \ 154	303 \ 68	312 \ 64	272 \ 122
α/(μV K^{-1})	90 \ 220	109 \ 269	116 \ 283	126 \ 211
P.F./(μW cm^{-1}K^{-2})	4.4 \ 7.5	3.6 \ 4.9	4.2 \ 5.1	4.3 \ 5.4
κ/(W m^{-1}K^{-1})	0.73 \ 0.41	0.52 \ 0.33	0.62 \ 0.32	0.52 \ 0.51
zT	0.19 \ 1.26	0.22 \ 1.02	0.24 \ 1.09	0.27 \ 0.74

Table 6.7 Thermoelectric properties of $Tl_{10-x}Pb_xTe_6$ with $1.95 \leq x \leq 2.05$ at ≈ 320 K (first value) and at ≈ 685 K (second value) in comparison to Tl_4PbTe_3 reported by Kosuga et al.*.

Property	$x = 1.9$	$x = 1.925$	$x = 1.95$	$x = 2$	$x = 2.05$	Tl_4PbTe_3*
$\sigma/(\Omega^{-1}cm^{-1})$	1520 \ 199	1344 \ 169	1343 \ 139	1174 \ 79	417 \ 44	781 \ 95
$\alpha/(\mu V\ K^{-1})$	9 \ 213	12 \ 219	17 \ 238	36 \ 281	76 \ 299	54 \ 233
$P.F./(\mu W\ cm^{-1}K^{-2})$	0.13 \ 9.0	0.21 \ 8.1	0.39 \ 7.9	1.5 \ 6.2	2.4 \ 3.9	2.3 \ 5.2
$\kappa/(W\ m^{-1}K^{-1})$	1.21 \ 0.45	1.27 \ 0.43	1.30 \ 0.44	1.03 \ 0.36	0.78 \ 0.33	1.20 \ 0.49
zT	0.05 \ 1.42	0.01 \ 1.31	0.01 \ 1.22	0.05 \ 1.16	0.10 \ 0.82	0.06 \ 0.71

The electrical conductivity, σ, data between 300 K and 700 K are displayed in Figure 6.3, in comparison to the results from Kosuga et al.,[63] (labeled JAP, 2006 for J. Appl. Phys., 2006). In each case, σ decreases with increasing temperature, indicative of a large number of charge carriers. This is true even in case of the nominally intrinsic semiconductors with $x = 2$, including the samples from Kosuga et al., whose values and slopes resemble the ones from our samples of the same formula. With these materials being *p*-type conductors, the carrier concentration and thusly the electrical conductivity should generally decrease with increasing *E* content. Highly unusual is the large temperature dependence of the Pb samples, whereas the Sn samples exhibit more usual, relatively flat curves. As a consequence, the Pb samples exhibit much higher σ values than the Sn samples around room temperature, and comparable values above 600 K. For example, σ of $Tl_{8.1}Pb_{1.9}Te_6$ decreases from 1520 $\Omega^{-1}cm^{-1}$ at 320 K to 200 $\Omega^{-1}cm^{-1}$ at 685 K, and $Tl_{7.95}Pb_{2.05}Te_6$ from 420 $\Omega^{-1}cm^{-1}$ to 44 $\Omega^{-1}cm^{-1}$, compared to the smaller σ range of $Tl_{8.05}Sn_{1.95}Te_6$ (from 550 $\Omega^{-1}cm^{-1}$ to 150 $\Omega^{-1}cm^{-1}$). Considering an estimated experimental error of

±5%, the numbers are significantly different. With the Sb and Bi representatives behaving similar to the Sn samples here, the Pb materials clearly stand out of this class of Tl_5Te_3-based materials.

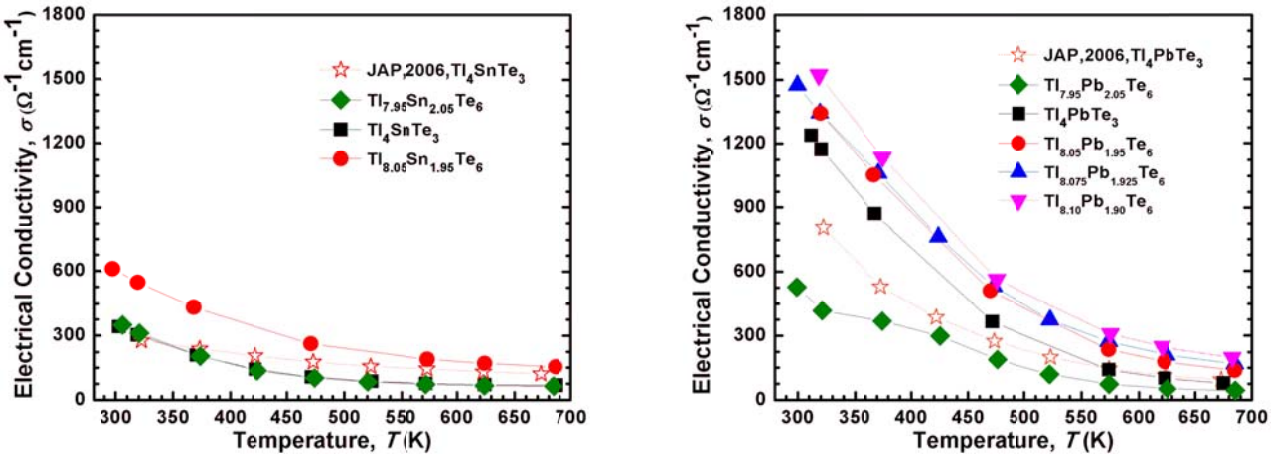

Figure 6.3 Electrical conductivity of $Tl_{10-x}Sn_xTe_6$ (left) and $Tl_{10-x}Pb_xTe_6$ (right).

The Seebeck coefficient, α, data are compared in Figure 6.4. As expected, the materials with larger σ values exhibit smaller α values because of the almost reciprocal relationship of α with the carrier concentration. In other words, increasing x occurs with increasing Seebeck coefficient. In case of $Tl_{10-x}Sn_xTe_6$, α varies from +90 μV K^{-1} for x = 1.95 to +116 μV K^{-1} for x = 2.05 at 320 K, while the 690 K values are more than twice as large (between +220 μV K^{-1} and 283 μV K^{-1}). With an experimental error of ±3%, these differences are significant. The Tl_4SnTe_3 sample from Kosuga et al. has almost identical α values to our $Tl_{8.05}Sn_{1.95}Te_6$, which are significantly lower than those of our Tl_4SnTe_3 sample, while the conductivity was comparable. We postulate that Kosuga's sample had more defects, i.e. a larger carrier concentration, but more grain boundary scattering causing comparable conductivity despite the higher carrier concentration. The same is true for the Pb materials, with Kosuga's data matching the ones from our x = 1.95 sample.

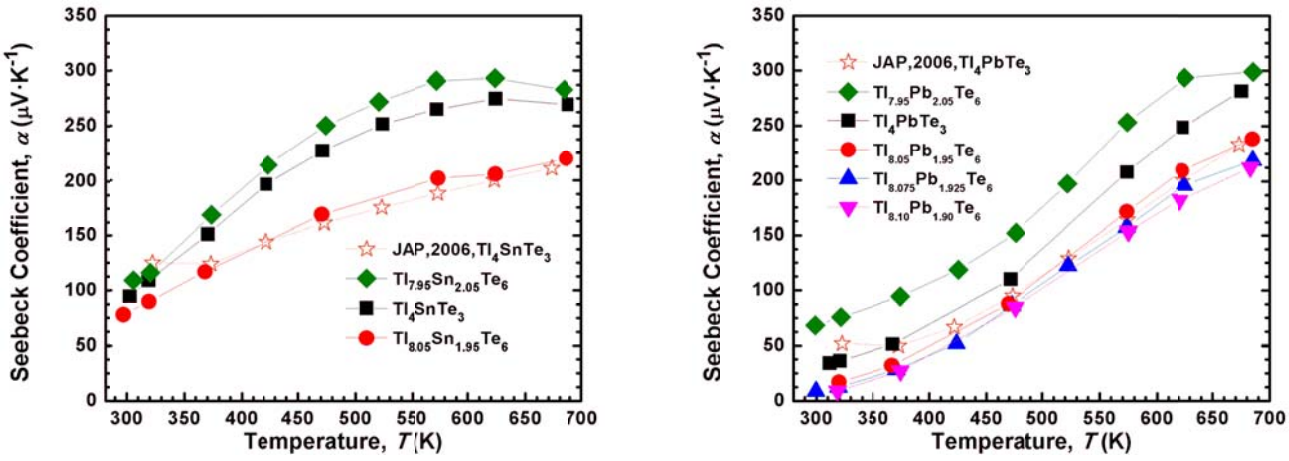

Figure 6.4 Seebeck coefficient of $Tl_{10-x}Sn_xTe_6$ (left) and $Tl_{10-x}Pb_xTe_6$ (right).

As discussed for the electrical conductivity, the temperature dependence of the Pb containing materials is particularly pronounced, with α of Tl_4PbTe_3 increasing from 36 μV K^{-1} at 320 K to 281 μV K^{-1} at 690 K, while α of Tl_4SnTe_3 increases from 116 μV K^{-1} to 269 μV K^{-1} in that temperature range. Moreover, it is interesting to note that α of Tl_4SnTe_3 and of $Tl_{7.95}Sn_{2.05}Te_6$ reach maxima around 624 K of 275 μV K^{-1} and 293 μV K^{-1}, respectively, while no Pb containing telluride shows a decrease in α at any temperature measured here. Such a maximum occurs at the temperature where the intrinsic carriers begin to cross the band gap in significant amounts, and may thus be used to estimate the band gap, E_g, via the relation $E_g = 2\ e\ \alpha_{max}\ T_{max}$, with e = electron charge.[98] This results in E_g = 0.34 eV for Tl_4SnTe_3 and 0.37 eV for $Tl_{7.95}Sn_{2.05}Te_6$, in qualitative agreement with the WIEN2k calculation.

The electrical performance of thermoelectrics is measured by the numerator of the figure-of-merit zT, namely the power factor, $P.F. = \alpha^2\sigma$, revealed in Figure 6.5. While the Sn containing materials show reasonable values between 3.6 μW $cm^{-1}K^{-2}$ and 7.6 μW $cm^{-1}K^{-2}$, the Pb materials again exhibit a very pronounced temperature dependence, the most extreme example being $Tl_{8.10}Pb_{1.90}Te_6$. In that case, $P.F.$ increases from 0.13 μW $cm^{-1}K^{-2}$ at 320 K to at 9.0 μW $cm^{-1}K^{-2}$ 685 K. Except for T < 400 K, all Pb

samples investigated here have better electrical performance than Kosuga's Tl_4PbTe_3, which reaches *P.F.* = 5.2 μW $cm^{-1}K^{-2}$ at 685 K. Likewise, most of our Sn samples perform better electrically at most temperatures than Kosuga's Tl_4SnTe_3, with $Tl_{8.05}Sn_{1.95}Te_6$ being superior at all temperatures investigated.

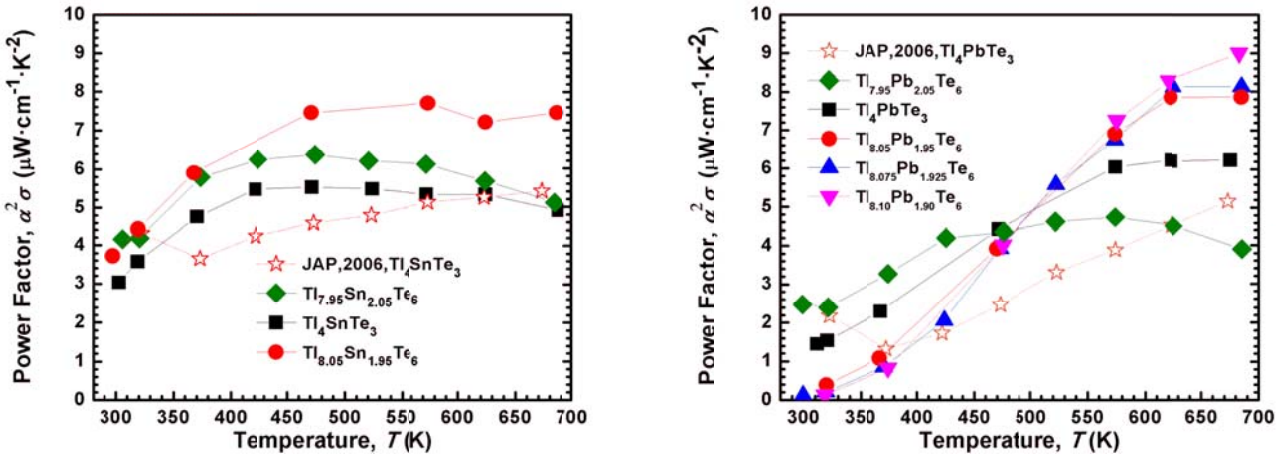

Figure 6.5 Power factor of $Tl_{10-x}Sn_xTe_6$ (left) and $Tl_{10-x}Pb_xTe_6$ (right).

For comparison, the above mentioned high *zT* *n*-type materials $Ba_{0.08}La_{0.05}Yb_{0.04}Co_4Sb_{12}$[26] and $Ba_8Ni_{0.31}Zn_{0.52}Ga_{13.06}Ge_{32.2}$[99] exhibit significantly higher power factors of up to 52 μW $cm^{-1}K^{-2}$ and 15 μW $cm^{-1}K^{-2}$. $Yb_{13.6}La_{0.4}MnSb_{11}$ is *p*-type and more comparable with a maximal *P.F.* = 6.2 μW $cm^{-1}K^{-2}$,[100] and $Tl_{0.02}Pb_{0.98}Te$ reaches *P.F.* = 19 μW $cm^{-1}K^{-2}$ around 700 K.[101]

Thermal conductivity data, κ, are presented in Figure 6.6. All samples have very low κ values, with the Sn containing samples showing consistently $\kappa < 0.75$ W $m^{-1}K^{-1}$. With the exception of Kosuga's Tl_4SnTe_3, κ decreases consistently throughout the whole temperature range because of the decreasing mobility of both the phonons and electrical charge carriers. Lead telluride and the skutterudites and clathrates typically exhibit larger (yet still relatively low) thermal conductivity, with κ values at high temperatures of 1.0 W $m^{-1}K^{-1}$ for $Tl_{0.02}Pb_{0.98}Te$,[101] 2.6 W $m^{-1}K^{-1}$ for $Ba_{0.08}La_{0.05}Yb_{0.04}Co_4Sb_{12}$[26] and 1.3

W $m^{-1}K^{-1}$ for $Ba_8Ni_{0.31}Zn_{0.52}Ga_{13.06}Ge_{32.2}$,[99] while κ of $Yb_{13.6}La_{0.4}MnSb_{11}$ is comparable (0.7 W $m^{-1}K^{-1}$).[100]

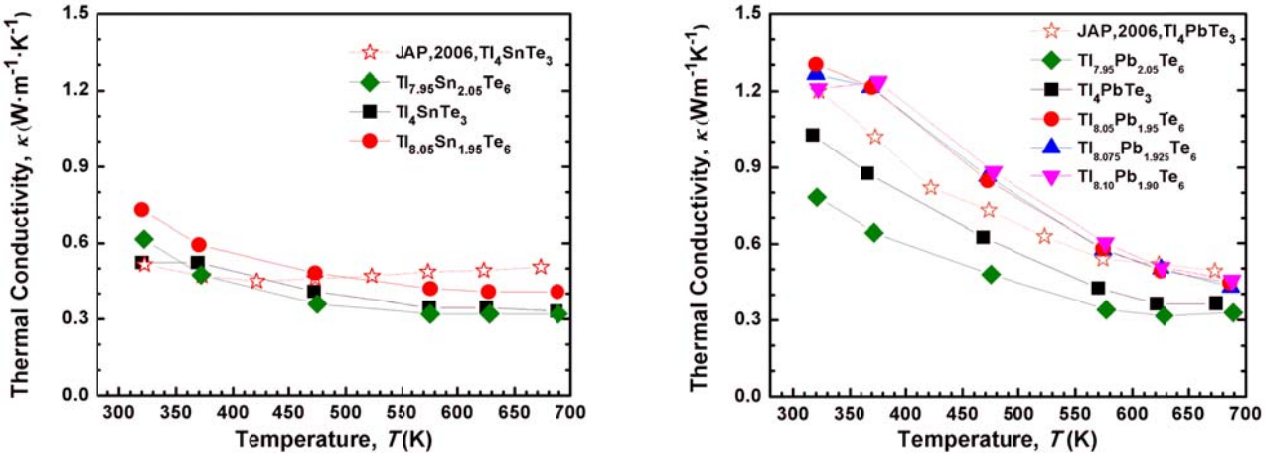

Figure 6.6 Thermal conductivity of $Tl_{10-x}Sn_xTe_6$ (left) and $Tl_{10-x}Pb_xTe_6$ (right).

As shown in Figure 6.7, all κ_L values of the new samples are below 0.5 W $m^{-1}K^{-1}$ throughout the whole measured temperature range. Wölfing et al. calculated the so-called minimal thermal conductivity for a fully disordered solid composed of the elements Tl-Bi-Te in the 9 : 1 : 6 ratio to be κ_{min} = 0.2 W $m^{-1}K^{-1}$.[84] Thus, these materials are very close to the lowest possible thermal conductivity. For a more detailed consideration of κ_L, one needs to realize the large uncertainties, because κ_L was estimated from the difference of two similar experimentally obtained values, which have an experimental error of roughly ±5%. In addition, the Lorenz number may vary with charge carrier concentration and temperature (and material), further adding to the uncertainty of κ_L. In any case, all these values are significantly lower than those of other leading thermoelectrics, where one often aims to achieve κ_L = 1 W $m^{-1}K^{-1}$ at low T.[102] For example, κ_L of $Tl_{0.02}Pb_{0.98}Te$ amounts to ≈1.9 W $m^{-1}K^{-1}$ at 300 K, estimated using the degenerate L.

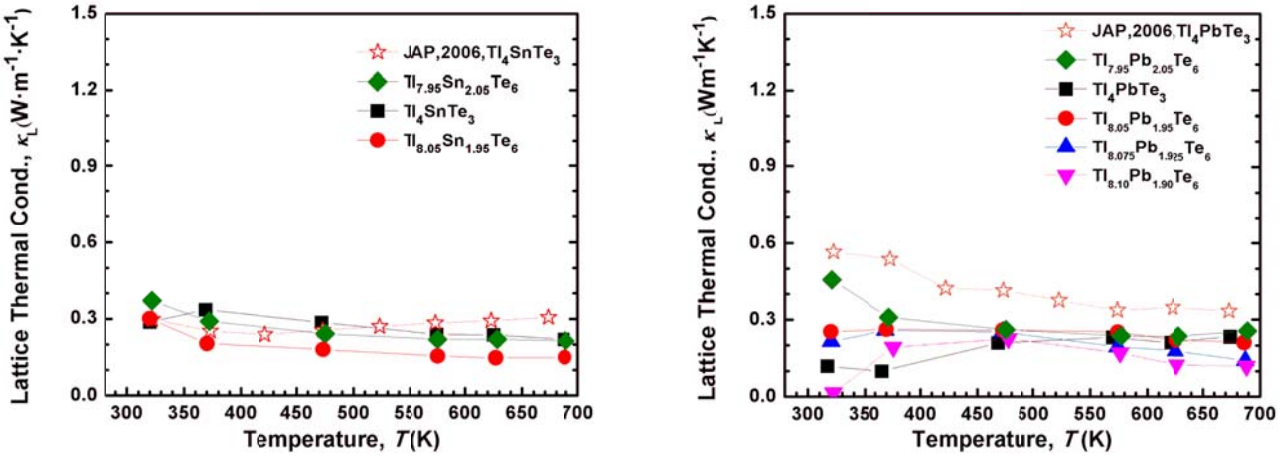

Figure 6.7 Lattice thermal conductivity of $Tl_{10-x}Sn_xTe_6$ (left) and $Tl_{10-x}Pb_xTe_6$ (right).

From the experimental data described above, the figure-of-merit for the $Tl_{10-x}E_xTe_6$ series was calculated via $zT = T\alpha^2\sigma\kappa^{-1}$. With the exception of the samples with $x = 2.05$, which do contain *E*Te as a side product, all samples exhibit increasing zT values with increasing T throughout the whole temperature range (Figure 6.8), as often found for thermoelectric materials. The highest zT values occur in the samples $Tl_{8.05}Sn_{1.95}Te_6$ and $Tl_{8.10}Pb_{1.90}Te_6$, culminating in $zT = 1.26$ and $zT = 1.42$, respectively, which both are *p*-doped (deficient in E = Sn, Pb) compared to the formally intrinsic semiconductors Tl_4ETe_3. Because of the steep zT curve of $Tl_{8.10}Pb_{1.90}Te_6$, this is not necessarily the best sample, depending on the T range of interest, because the (impure) samples $Tl_{7.95}E_{2.05}Te_3$ are superior below 600 K.

From the estimated errors in the determination of α, σ, and κ, the error in zT is concluded to amount to ±8%. Therefore, the above-mentioned maximal zT values of 1.26 ± 0.10 and 1.42 ± 0.11 are not significantly different. We obtained similar values for the Pb samples after synthesizing two new batches from scratch, resulting in $zT = 1.34$ and 1.46 at 685 K. Likewise, repeat measurements on the same pellets showed no signs of a significant decay - details are presented in the experimental section.

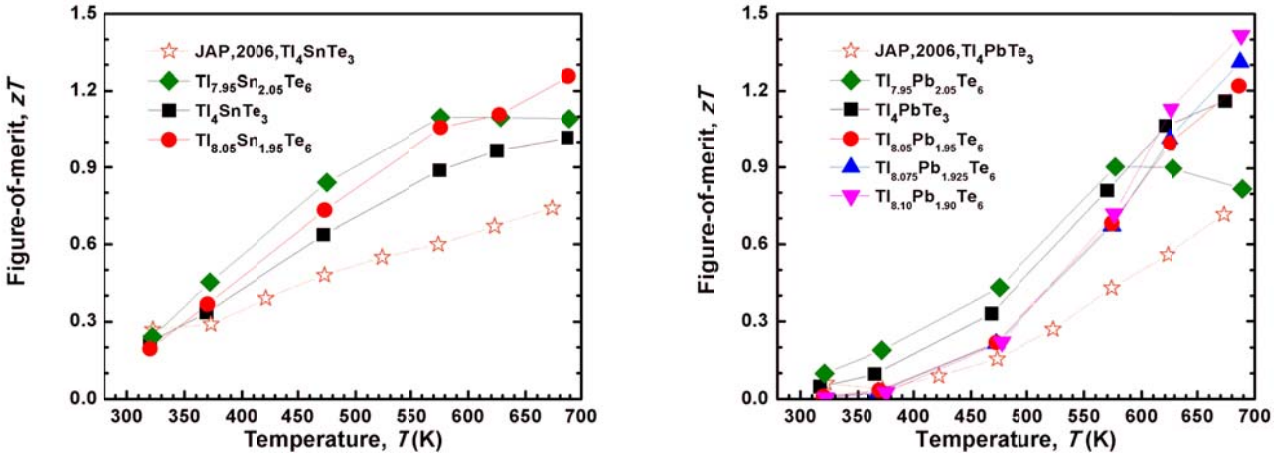

Figure 6.8 Figure-of-merit of $Tl_{10-x}Sn_xTe_6$ (left) and $Tl_{10-x}Pb_xTe_6$ (right).

As compared in Figure 6.9, these materials are very competitive compared to other leading bulk materials as well, including the *n*-type triple-filled skutterudite $Ba_{0.08}La_{0.05}Yb_{0.04}Co_4Sb_{12}$,[26] whose figure-of-merit curve closely resembles that of $Tl_{8.05}Sn_{1.95}Te_6$, and clearly outperforming the *p*-type Zintl phase $Yb_{13.6}La_{0.4}MnSb_{11}$ below 700 K.[100] The thermoelectric performance of $Tl_{8.05}Sn_{1.95}Te_6$ is better than *p*-type $Tl_{0.02}Pb_{0.98}Te$ until 673 K,[101] which is typically viewed as the upper temperature limit for thermoelectric generators in automotives, and thereafter $Tl_{0.02}Pb_{0.98}Te$ begins to outperform $Tl_{8.05}Sn_{1.95}Te_6$.[101]

To check for stability, the measurements of the electrical properties were repeated in several cases; no noticeable degrading was detected. To check for reproducibility, two more samples of the target composition $Tl_{8.10}Pb_{1.90}Te_6$ - the one with the highest $zT_{max} > 1.4$ - were prepared and characterized. As evidenced in Figure 6.10, these samples are both stable under the measurement conditions (shown in repeat measurements) and highly reproducible (reflected in zT_{max} values of 1.34, 1.42 and 1.46 at 685 K and of 1.26 at 675 K).

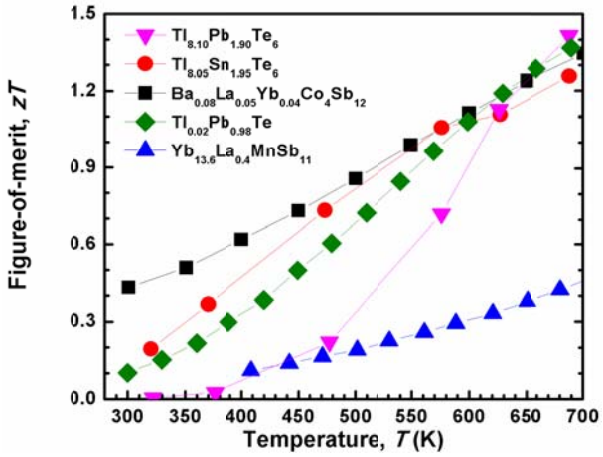

Figure 6.9 Figure-of-merit of $Tl_{8.05}Sn_{1.95}Te_6$ and $Tl_{8.10}Pb_{1.90}Te_6$ in comparison to selected leading thermoelectrics.

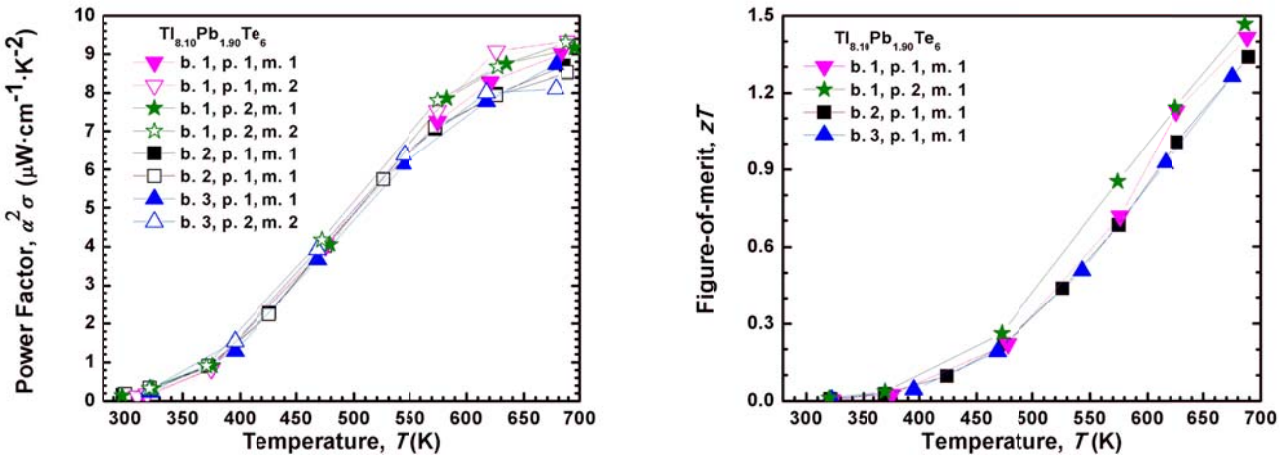

Figure 6.10 Power factor (left) and figure-of-merit (right) of several measurements of $Tl_{8.10}Pb_{1.90}Te_6$. b. = batch, p. = pellet, m. = measurement.

6.4. Conclusions

We have successfully prepared a variety of Sn- and Pb-containing variants of Tl_5Te_3, and determined their thermoelectric properties. These materials are bestowed with an intrinsic low thermal

conductivity, which ultimately leads to high zT values in combination with moderate power factors. The improvements compared to the literature data on Tl_4SnTe_3 and Tl_4PbTe_3 (zT = 0.71 and 0.74 at 680 K) are significant (and occur at all temperatures), amounting to relative advancements of approximately 75% and 90%. The highest zT values were obtained in the cases of $Tl_{8.05}Sn_{1.95}Te_6$ with zT = 1.26 and $Tl_{8.10}Pb_{1.90}Te_6$ with zT = 1.46, both below 700 K.

7. Summary and Outlook

In this thesis, several series of *p*-type polycrystalline thallium tellurides have been successfully fabricated by a combination of the melting-slow cooling-down process and hot-pressing technique. The 9-1-6 modifications include Tl_9LnTe_6 (Ln = La, Ce, Pr, Nd, Sm, Gd, Tb), $Tl_{10-x}La_xTe_6$ (x = 0.90, 0.95, 1.00, 1.05). $Tl_9Bi_{1-x}Te_6$ ($0 \le x \le 0.05$), $Tl_{9-x}Bi_{1+x}Te_6$ ($0 \le x \le 0.05$), $Tl_9Sb_{1-x}Te_6$ ($0 \le x \le 0.03$), $Tl_{9-x}Sb_{1+x}Te_6$ ($0 \le x \le 0.03$), $Tl_9Bi_{1-x}Sn_xTe_6$($0 \le x \le 0.15$), $Tl_9Bi_{1-y}Pb_yTe_6$ ($0 \le y \le 0.15$), $Tl_9Sb_{1-m}Sn_mTe_6$ ($0 \le m \le 0.10$) and $Tl_9Sb_{1-n}Pb_nTe_6$ ($0 \le n \le 0.10$). The 8-2-6 variants are $Tl_{10-x}Sn_xTe_6$ ($1.95 \le x \le 2.05$) and $Tl_{10-x}Pb_xTe_6$ ($1.90 \le x \le 2.05$). Their crystal structure, electronic structure and high temperature electrical and thermal transport properties were also investigated. These findings resulted in publications in *Journal of Alloys and Compounds*, *Chemistry of Materials*, *Journal of Applied Physics* and *Advanced Energy Materials*.

One of the most impressive features of these themoelectrics is their low thermal conductivity values ($\kappa < 1.1$ W $m^{-1}K^{-1}$), as shown in Figure 7.1. Our results demonstrate that replacing an optimal portion of the Tl in Tl_5Te_3 by lanthanide elements, tetrels (*Tt* = Sn and Pb) and pnicotgens (*Pn* = Sb and Bi) will effectively tuning the transport properties from metallic to semiconducting, thereby culminating in enhanced thermoelectric performance. For example, zT = 0.51 at 550 K, zT = 0.84 at 500 K, zT = 0.98 at 500 K, zT = 1.02 at 685 K and zT = 1.16 at 685 K were obtained for Tl_9LaTe_6, Tl_9SbTe_6, Tl_9BiTe_6, Tl_4SnTe_3 and Tl_4PbTe_3, respectively. Through slightly adjusting the carrier concentration, higher zT values were obtained in the cases of $Tl_{8.05}Sn_{1.95}Te_6$ with zT = 1.26 and $Tl_{8.10}Pb_{1.90}Te_6$ with zT = 1.46, both below 700 K. These extraordinary zT values make thallium tellurides competitive to the other state-of-the-art thermoelectric materials for intermediate temperature (400 – 700 K) power generation.

Whether or not these tellurides can be further improved, for example via optimizing of the particle size or nanostructuring or partial Se/Te substitution remains the topic of further investigations.

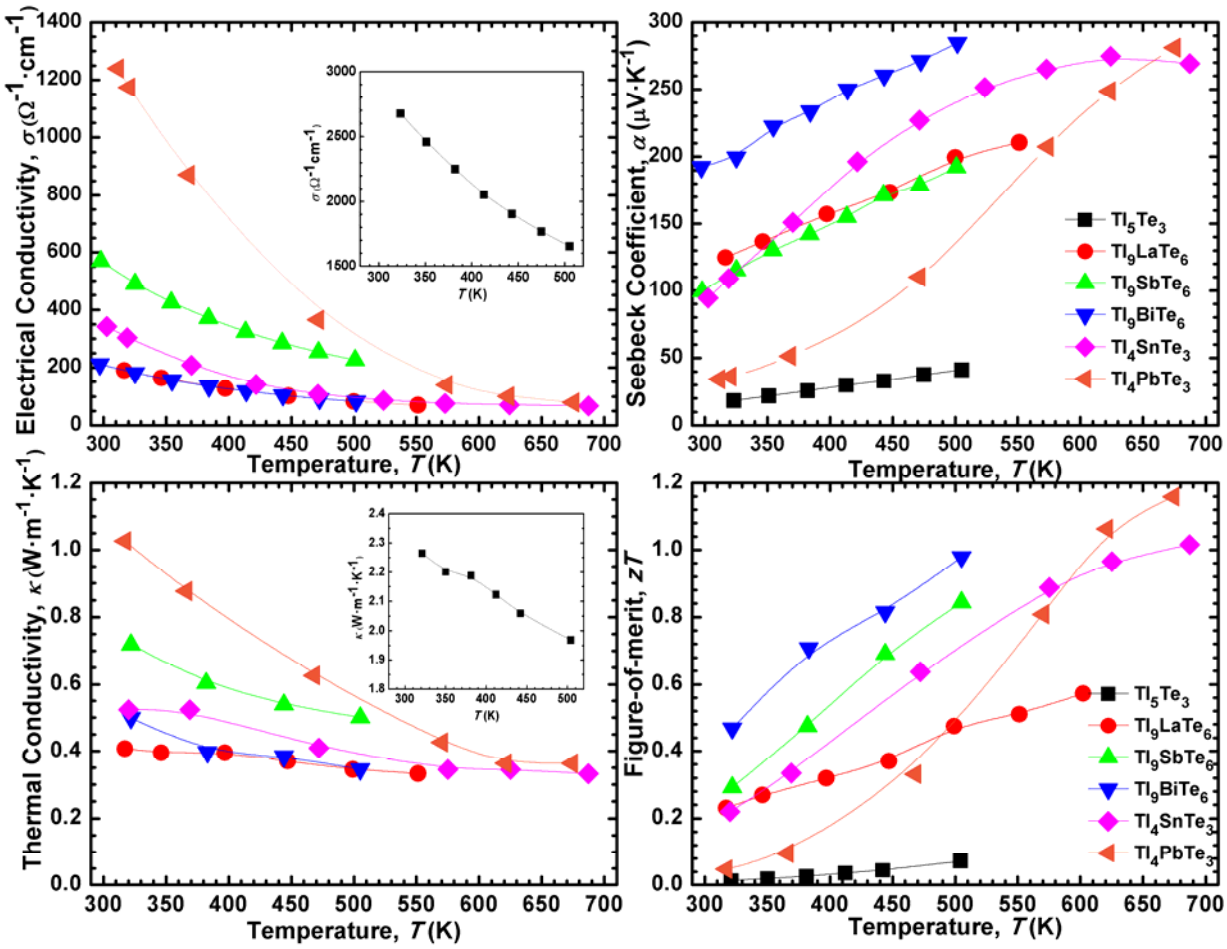

Figure 7.1 Thermoelectric properties of stoichiometric modifications of Tl_5Te_3

References

1 D. M. Rowe, *Thermoelectric Handbook: Macro to Nano* (CRC Press, Taylor & Francis Group, Boca Raton, FL, USA, 2006).
2 J. Yang and T. Caillat, MRS Bull **31**, 224 (2006).
3 L. E. Bell, Science **321**, 1457 (2008).
4 G. J. Snyder and E. S. Toberer, Nat Mater **7**, 105 (2008).
5 T. Takabatake, K. Suekuni, T. Nakayama, and E. Kaneshita, Rev Mod Phys **86**, 669 (2014).
6 A. R. West, *Solid state chemistry and its applications* (John Wiley & Sons, 2007).
7 H. Goldsmid, *Thermoelectric refrigeration* (Plenum Press, New York, 1964).
8 F. J. DiSalvo, Science **285**, 703 (1999).
9 N. F. Mott, *The Theory of the Properties of Metals and Alloys* (Dover Publications, Inc, New York, 1958).
10 R. Franz and G. Wiedemann, Ann Phys-Berlin **165**, 497 (1853).
11 C. Kittel, *Introduction to Solid State Physics* (Wiley, 1996).
12 G. A. Slack, *Solid State Physics* (Academic Press, New York, 1979).
13 J. M. Ziman, *Electrons and phonons: the theory of transport phenomena in solids* (Oxford University Press, 1960).
14 D. G. Cahill, S. K. Watson, and R. O. Pohl, Phys Rev B **46**, 6131 (1992).
15 P. W. Lange, Naturwiss **27**, 133 (1939).
16 J. Drabble and C. Goodman, J Phys Chem Solids **5**, 142 (1958).
17 T. M. Tritt and M. A. Subramanian, MRS Bull **31**, 188 (2006).
18 Y. Pei, H. Wang, and G. Snyder, Adv Mater **24**, 6125 (2012).
19 A. D. LaLonde, Y. Pei, H. Wang, and G. J. Snyder, Mater Today **14**, 526 (2011).
20 K. Biswas, J. He, I. D. Blum, C.-I. Wu, T. P. Hogan, D. N. Seidman, V. P. Dravid, and M. G. Kanatzidis, Nature **489**, 414 (2012).
21 H. Kleinke, Chem Mater **22**, 604 (2010).
22 X. Su, H. Li, Y. Yan, G. Wang, H. Chi, X. Zhou, X. Tang, Q. Zhang, and C. Uher, Acta Mater **60**, 3536 (2012).
23 X. Su, H. Li, Y. Yan, H. Chi, X. Tang, Q. Zhang, and C. Uher, J Mater Chem **22**, 15628 (2012).
24 G. Rogl, A. Grytsiv, M. Falmbigl, E. Bauer, P. Rogl, M. Zehetbauer, and Y. Gelbstein, J Alloy Compd **537**, 242 (2012).
25 G. Rogl, A. Grytsiv, M. Falmbigl, E. Bauer, C. Mangler, C. Rentenberger, M. Zehetbauer, and P. Rogl, Acta Mater **60**, 4487 (2012).
26 X. Shi, J Yang, J. R. Salvador, M. Chi, J. Y. Cho, H. Wang, S. Bai, J. Yang, W. Zhang, and L. Chen, J Am Chem Soc **133**, 7837 (2011).
27 Q. Guo and H. Kleinke, J Solid State Chem **215**, 253 (2014).
28 Q. Guo, A. Assoud, and H. Kleinke, J Solid State Chem, *in press* (2015).
29 J. C. Slater, J Chem Phys **41**, 3199 (1964).
30 G. J. Snyder, M. Christensen, E. Nishibori, T. Caillat, and B. B. Iversen, Nat Mater **3**, 458 (2004).
31 A. Zevalkink, G. S. Pomrehn, S. Johnson, J. Swallow, Z. M. Gibbs, and G. J. Snyder, Chem Mater **24**, 2091 (2012).
32 W. G. Zeier, A. Zevalkink, E. Schechtel, W. Tremel, and G. J. Snyder, J Mater Chem **22**, 9826 (2012).

[33] Y. Pei, A. D. LaLonde, N. A. Heinz, and G. J. Snyder, Adv Energy Mater **2**, 670 (2012).
[34] H. Liu, X. Shi, F. Xu, L. Zhang, W. Zhang, L. Chen, Q. Li, C. Uher, T. Day, and G. J. Snyder, Nat Mater **11**, 422 (2012).
[35] X. Shi, Y. Pei, G. J. Snyder, and L. Chen, Energy Environ Sci **4**, 4086 (2011).
[36] H. Wang, Y. Pei, A. D. LaLonde, and G. J. Snyder, Adv Mater **23**, 1366 (2011).
[37] A. F. May, J. P. Fleurial, and G. J. Snyder, Chem Mater **22**, 2995 (2010).
[38] C. R. Sankar, A. Becker, A. Assoud, and H. Kleinke, Inorg Chem **52**, 1895 (2013).
[39] C. R. Sankar, A. Assoud, and H. Kleinke, Inorg Chem **52**, 13869 (2013).
[40] C. R. Sankar, B. A. Kuropatwa, A. Assoud, and H. Kleinke, Dalton Trans **41**, 9646 (2012).
[41] C. R. Sankar, S. Bangarigadu-Sanasy, and H. Kleinke, J Electron Mater **41**, 1662 (2012).
[42] C. R. Sankar, M. Guch, A. Assoud, and H. Kleinke, Chem Mater **23**, 3886 (2011).
[43] C. R. Sankar, S. Bangarigadu-Sanasy, A. Assoud, and H. Kleinke, Inorg Chem **50**, 245 (2011).
[44] C. R. Sankar, S. Bangarigadu-Sanasy, A. Assoud, and H. Kleinke, J Mater Chem **20**, 7485 (2010).
[45] M. A. McGuire, T. J. Scheidemantel, J. V. Badding, and F. J. DiSalvo, Chem Mater **17**, 6186 (2005).
[46] M. A. McGuire, T. K. Reynolds, and F. J. DiSalvo, Chem Mater **17**, 2875 (2005).
[47] K. Kurosaki and S. Yamanaka, Phys Status Solidi A **210**, 82 (2013).
[48] K. Kurosaki, A. Kosuga, H. Muta, M. Uno, and S. Yamanaka, Appl Phys Lett **87**, 061919 (2005).
[49] J. W. Sharp, B. C. Sales, D. G. Mandrus, and B. C. Chakoumakos, Appl Phys Lett **74**, 3794 (1999).
[50] I. Schewe, P. Böttcher, and H. G. von Schnering, Z Kristallogr **188**, 287 (1989).
[51] X. Tao, P. Jund, R. Viennois, and J.-C. Tédenac, J Phys Chem A **115**, 8761 (2011).
[52] S. Bangarigadu-Sanasy, C. R. Sankar, A. Assoud, and H. Kleinke, Dalton Trans **40**, 862 (2011).
[53] S. Bangarigadu-Sanasy, C. R. Sankar, P. Schlender, and H. Kleinke, J Alloy Compd **549**, 126 (2013).
[54] P. Blaha, K. Schwarz, G. K. H. Madsen, D. Kvasnicka, and J. Luitz, *WIEN2k, An Augmented Plane Wave + Local Orbitals Program for Calculating Crystal Properties*, Techn. Universität Wien, Austria, 2001.
[55] K. Schwarz, J Solid State Chem **176**, 319 (2003).
[56] V. Agafonov, B. Legendre, N. Rodier, J. Cense, E. Dichi, and G. Kra, Acta Crystallogr C **47**, 850 (1991).
[57] R. E. Marsh, J Solid State Chem **87**, 467 (1990).
[58] G. S. Nolas, J. Sharp, and H. J. Goldsmid, *Thermoelectrics : Basic Principles and New Materials Developments* (Springer-Verlag Berlin Heidelberg New York, 2001).
[59] S. Bradtmöller and P. Böttcher, Z Anorg Allg Chem **619**, 1155 (1993).
[60] P. Böttcher, T. Doert, C. Druska, and S. Bradtmöller, J. Alloys Compd **246**, 209 (1997).
[61] S. Yamanaka, A. Kosuga, and K. Kurosaki, J Alloy Compd **352**, 275 (2003).
[62] B. Wölfing, C. Kloc, J. Teubner, and E. Bucher, Phys Rev Lett **86**, 4350 (2001).
[63] A. Kosuga, K. Kurosaki, H. Muta, and S. Yamanaka, J Appl Phys **99,** 063705 (2006).
[64] S. K. Bux, J.-P. Fleurial, and R. B. Kaner, Chem Commun **46**, 8311 (2010).
[65] V. K. Pecharsky and P. Y. Zavalij, *Fundamentals of Powder Diffraction and Structural Characterization of Materials* (Springer, 2009).
[66] A. C. Larson and R. B. Von Dreele, *Generalized Structural Analysis System (GSAS)*, LANSCE, MSH805, Los Alamos National Laboratory, NM 87545, USA, 1995.
[67] B. H. Toby, J Appl Crystallogr **34**, 210 (2001).
[68] G. M. Sheldrick, Acta Crystallogr A **64**, 112 (2008).

[69] H. Czichos, T. Saito, and L. R. Smith, *Springer handbook of materials measurement methods* (Springer Science & Business Media, 2006).
[70] R. Prasad, *Electronic Structure of Materials* (CRC Press, Taylor and Francis Group, 2013).
[71] W. Kohn and L. J. Sham, Phys Rev **140**, A1133 (1965).
[72] J. P. Perdew, Physica B Condens Matter **172**, 1 (1991).
[73] R. Dronskowski, *Computational Chemistry of Solid State Materials* (WILEY-VCH, 2005).
[74] H. Wang, W. D. Porter, H. Böttner, J. König, L. Chen, S. Bai, T. M. Tritt, A. Mayolet, J. Senawiratne, C. Smith, F. Harris, P. Gilbert, J. Sharp, J. Lo, H. Kleinke, and L. Kiss, J Electron Mater **42**, 1073 (2013).
[75] F. E. Neumann, Ann Phys-Berlin **99**, 9 (1831).
[76] H. Kopp, Ann der Chem and Pharm **3**, 289 (1864).
[77] M. B. Babanly, S. Z. Imamalieva, and F. M. Sadygov, in *News of Baku University*, 2009), Vol. 4, p. 5.
[78] S. Bangarigadu-Sanasy, C. R. Sankar, P. A. Dube, J. E. Greedan, and H. Kleinke, J Alloy Compd **589**, 389 (2014).
[79] V. I. Fistul', *Heavily Doped Semiconductors* (Plenum Press, New York, NY, USA, 1969).
[80] Q. Guo, M. Chan, B. A. Kuropatwa, and H. Kleinke, J Appl Phys **116**, 183702 (2014).
[81] Q. Guo, M. Chan, B. A. Kuropatwa, and H. Kleinke, Chem Mater **25**, 4097 (2013).
[82] E. Dichi, M. Sghaier, and G. Kra, J Alloy Compd **458**, 109 (2008).
[83] B. A. Kuropatwa, A. Assoud, and H. Kleinke, J Alloy Compd **509**, 6768 (2011).
[84] K. Kurosaki, K. Goto, A. Kosuga, H. Muta, and S. Yamanaka, Mat Res Soc Symp Proc **886**, 281 (2006).
[85] J. Shen, L. Hu, T. Zhu, and X. Zhao, Appl Phys Lett **99**, 124102 (2011).
[86] K. F. Hsu, S. Loo, F. Guo, W. Chen, J. S. Dyck, C. Uher, T. Hogan, E. K. Polychroniadis, and M. G. Kanatzidis, Science **303**, 818 (2004).
[87] K. Biswas, J. Q. He, Q. C. Zhang, G. Y. Wang, C. Uher, V. P. Dravid, and M. G. Kanatzidis, Nat Chem **3**, 160 (2011).
[88] A. Majumdar, Science **303**, 777 (2004).
[89] E. S. Toberer, A. F. May, and G. J. Snyder, Chem Mater **22**, 624 (2010).
[90] J. R. Sootsman, D. Y. Chung, and M. G. Kanatzidis, Angew Chem Int Ed **48**, 8616 (2009).
[91] Q. Guo, A. Assoud, and H. Kleinke, Adv Energy Mater **4**, 1400348 (2014).
[92] J. R. Sootsman, H. Kong, C. Uher, J. J. D'Angelo, C. I. Wu, T. P. Hogan, T. Caillat, and M. G. Kanatzidis, Angew Chem Int Ed **47**, 8618 (2008).
[93] J. P. Perdew, K. Burke, and M. Ernzerhof, Phys Rev Lett **77**, 3865 (1996).
[94] F. Tran and P. Blaha, Phys Rev Lett **102**, 226401 (2009).
[95] J. J. Pulikkotil, D. J. Singh, S. Auluck, M. Saravanan, D. K. Misra, A. Dhar, and R. C. Budhani, Phys Rev B **86**, 155204 (2012).
[96] M. Christensen, A. B. Abrahamsen, N. B. Christensen, F. Juranyi, N. H. Andersen, K. Lefmann, J. Andreasson, C. R. H. Bahl, and B. B. Iversen, Nat Mater **7**, 811 (2008).
[97] K. J. Nordell and G. J. Miller, J Alloy Compd **241**, 51 (1996).
[98] H. J. Goldsmid and J. W. Sharp, J Electron Mater **28**, 869 (1999).
[99] X. Shi, J. Yang, S. Bai, J. Yang, H. Wang, M. Chi, J. R. Salvador, W. Zhang, L. Chen, and W. Wong-Ng, Adv Energy Mater **20**, 755 (2010).
[100] E. S. Toberer, S. R. Brown, T. Ikeda, S. M. Kauzlarich, and G. J. Snyder, Appl Phys Lett **93**, 062110 (2008).

[101] J. P. Heremans, V. Jovovic, E. S. Toberer, A. Saramat, K. Kurosaki, A. Charoenphakdee, S. Yamanaka, and G. J. Snyder, Science **321**, 554 (2008).
[102] M. G. Kanatzidis, Chem Mater **22**, 648 (2010).

Permissions

"Reprinted (adapted) from J. Alloys Compd., 630, Quansheng Guo, Holger Kleinke, Thermoelectric Properties of hot-pressed Tl_9LnTe_6 (Ln = La, Ce, Pr, Nd, Sm, Gd, Tb) and $Tl_{10-x}La_xTe_6$ ($0.90 \leq x \leq 1.05$), 37 - 42, Copyright (2015), with permission from Elsevier."

"Reprinted (adapted) with permission from Q. Guo, M. Chan, B. A. Kuropatwa, H. Kleinke, Enhanced thermoelectric properties of variants of Tl_9SbTe_6 and Tl_9BiTe_6, Chem. Mater. 25, 4097 - 4104 (2013). Copyright (2013) American Chemical Society."

"Reprinted with permission from [Q. Guo, M. Chan, B. A. Kuropatwa, H. Kleinke, Thermoelectric properties of Sn- and Pb-doped Tl_9BiTe_6 and Tl_9SbTe_6, J. Appl. Phys. 116, 183702/1 - 9]. Copyright [2014], AIP Publishing LLC."

"Reprinted from Q. Guo, A. Assoud, H. Kleinke, Improved Bulk Materials with Thermoelectric Figure-of-Merit Greater than 1: $Tl_{10-x}Sn_xTe_6$ and $Tl_{10-x}Pb_xTe_6$, Adv. Energy Mater. 4, 1400348/1 - 8 (2014) with permission from John Wiley and Sons."